

Investigation of Differential Diffusion Effects in Turbulent Hydrogen Jet Flame using Conditional Moment Closure Method

by

Man Ching Ma

A thesis
presented to the University of Waterloo
in fulfillment of the
thesis requirement for the degree of
Master of Applied Science
in
Mechanical Engineering

Waterloo, Ontario, Canada, 2014

© Man Ching Ma 2014

Author's Declaration

I hereby declare that I am the sole author of this thesis. This is a true copy of the thesis, including any required final revisions, as accepted by my examiners.

I understand that my thesis may be made electronically available to the public.

Abstract

The effects of differential diffusion in the numerical modelling of a turbulent non-premixed hydrogen-air jet flame using a Conditional Moment Closure (CMC) method are investigated. The CMC calculations, which are coupled with computational fluid dynamics (CFD) calculations, relax the commonly used assumption of equal species mass diffusivities. The focus is on the predictions of species mass fractions and temperatures, especially the production of NO. The results of the calculations are compared with available experimental measurements.

The formulation of the CMC species transport equation including differential diffusion is presented and the closure of the terms are discussed. Further, the CMC equation for conditional enthalpy is also derived in the present study. The implementation of the CMC equations using two dimensional finite volume method is discussed, including a presentation of the discretised forms of the equations.

The results of the CMC calculations including the effects of differential diffusion show that NO mass fractions are increased from the large underpredictions observed for equal diffusivity results near the jet nozzle. Improvements are also found for other species such as H_2 and H_2O . The results show physical behaviours, such as a shift in the location of the reaction zone and increased reaction rates due to increased diffusion rates of H_2 . It is also found that differential diffusion effects persist downstream from the nozzle, where the effects are expected to be small, and reasons for the discrepancies are discussed in the present study. The profiles obtained from the CMC calculations show large radial variations, much larger than in equal diffusivity calculations. An analysis isolating the differential diffusion effects of various species shows that the largest changes occur due to the accounting for the differential diffusivity of H_2 . A budget of the terms in the CMC equations for the differentially diffusing chemical species and enthalpy is also investigated.

Acknowledgements

I would like to thank my supervisor, Professor Cécile Devaud, for providing assistance and guidance on my research throughout the duration of my MASc studies. My knowledge and understanding of CFD and combustion modelling have greatly improved thanks to her support. I would also like to thank my friends and colleagues in the Turbulent Combustion Modelling Group for the insightful discussions on various topics such as fluid dynamics and combustion. I would also like to thank Professor Serhiy Yarusevych and Professor Metin Renksizbulut for reviewing my thesis.

Table of Contents

List of Tables	ix
List of Figures	x
Nomenclature	xiv
1 Introduction	1
1.1 Overview	1
1.2 Objectives	2
1.3 Outline	4
2 Background	6
2.1 Principles of Turbulent Combustion	6
2.1.1 Classification of Combustion Processes	6
2.1.2 Governing Equations of Transport Phenomena and State Equations	7
2.1.3 Statistical Description of Turbulence	12
2.1.4 Averaging Transport Equations	16
2.2 Computational Fluid Dynamics of Turbulent Flows	18
2.2.1 Direct Numerical Simulation	18
2.2.2 RANS Modelling	18
2.2.3 Large Eddy Simulation	21

2.3	Turbulent Non-premixed Reacting Flow Modelling	21
2.3.1	Turbulence-Chemistry Interaction	21
2.3.2	Mixture Fraction	22
2.3.3	Scalar Dissipation Rate	23
2.3.4	Chemistry	24
2.4	Models for Turbulent Non-premixed Combustion	25
2.4.1	Fast Chemistry Models	25
2.4.2	Laminar Flamelet Models	27
2.4.3	Conditional Moment Closure	28
2.4.4	Transported PDF models	28
3	Differential Diffusion in Turbulent Non-premixed Combustion	30
3.1	Theory	30
3.2	Differential Diffusion in Experimental Studies	33
3.3	Differential Diffusion in DNS Studies	36
3.4	Progress in Differential Diffusion Modelling	37
3.5	Summary	40
4	Conditional Moment Closure	42
4.1	Probability Density Function Transport Equation	42
4.2	Equal Diffusivity CMC Formulation	43
4.3	CMC Formulation of Species Equation Including Differential Diffusion . . .	46
4.4	CMC Formulation of Enthalpy Equation Including Differential Diffusion . .	49
4.5	Models for the Unclosed Terms	51
4.5.1	Closure Hypothesis for J_Y	51
4.5.2	Presumed Probability Density Function	53
4.5.3	Chemical Source Term	57
4.5.4	Radiative Heat Loss	58

4.5.5	Conditional Velocity and Turbulent Flux	58
4.5.6	Conditional Scalar Dissipation Rate	59
4.6	Summary of CMC Equations with Differential Diffusion	61
5	Implementation of Conditional Moment Closure	63
5.1	Overview of Computational Methodology	63
5.2	Finite Volume Discretisation of the CMC equations	65
5.3	Advection Scheme	70
5.4	PDF Ratio	71
5.5	Numerical Solver	72
5.6	Lewis Number	73
6	Hydrogen Flame Calculations	75
6.1	Description of Experimental Study	75
6.2	Computational Setup	77
6.2.1	Computational Domain, Boundary Conditions, and Initial Conditions	78
6.2.2	Turbulence Model	81
6.2.3	Temperature	82
6.2.4	Chemical Kinetics	82
6.2.5	Radiative Heat Loss	86
6.2.6	Cross-stream averaging	87
6.3	Sensitivity Analysis	88
6.3.1	Grid Spacing	88
6.3.2	Turbulence Modelling Constant	89
6.4	Velocity Field Results	90
6.5	Equal Diffusivity Results	92
6.5.1	Mixing Field	92
6.5.2	Conditional Scalars	95

6.5.3	Unconditional Mean Scalar Field	97
6.6	Differential Diffusivity Results	101
6.6.1	Conditional Scalars	102
6.6.2	Mean Mixing and Unconditional Scalar Field	108
6.6.3	Radial Dependence of Conditional Scalars	117
6.6.4	Differential Diffusion Effects of Individual Species	119
6.6.5	Analysis of CMC equation	122
7	Conclusions	128
7.1	Hydrogen Flame Results	129
7.2	Recommendations and Future Work	130
	APPENDICES	132
A	Derivation of CMC species transport equation	133
B	Derivation of CMC enthalpy transport equation	137
	References	140

List of Tables

2.1	Classification of combustion systems	8
2.2	Non-premixed combustion models and their major assumptions	26
5.1	Lewis numbers from simplified transport model of Smooke	74
6.1	Summary of flame conditions	76
6.2	Estimates of experimental accuracy	77
6.3	Distribution of nodes in spatial grid	80
6.4	Distribution of nodes in η grid	81
6.5	Enthalpy coefficients	83
6.6	Hydrogen-nitrogen chemical mechanism	84
6.7	Various spatial grids	88

List of Figures

2.1	CDF and PDF of Gaussian distribution	13
2.2	Reynolds decomposition of point scalar measurement	17
2.3	Sketch of the effect of scalar dissipation rate on temperature	24
2.4	Burke-Schumann solution for fuel (F), oxidizer (O), and product (P) mass fractions against mixture fraction.	27
4.1	Clipped Gaussian and β distributions with for different values of $\tilde{\xi}$ and $\tilde{\xi}''^2$	56
4.2	χ_η distribution modelled by AMC	60
5.1	Computational methodology	64
5.2	Section of computational grid, reproduced from Cleary	66
6.1	Computational domain and boundary conditions (not to scale)	79
6.2	Specified inlet velocity profile	79
6.3	Planck mean absorption coefficient K_{p,H_2O}	87
6.4	Axial Favre averaged mixture fraction profile with differential diffusion effects for various grids	89
6.5	Radial profiles of Favre averaged Bilger's mixture fraction with differential diffusion effects for various $C_{\varepsilon,1}$	90
6.6	Predicted radial profiles of Favre averaged velocity. Experimental measurements are from the TNF library	91
6.7	Predicted radial profiles of Favre averaged turbulent kinetic energy. Experimental measurements are from the TNF library	92

6.8	Predicted radial profiles of Favre averaged Bilger's mixture fraction. Experimental measurements are from the TNF library	93
6.9	Predicted radial profiles of rms of Favre averaged mixture fraction variance. Experimental measurements are from the TNF library	94
6.10	Predicted profile of conditional radially averaged H ₂ , O ₂ , and H ₂ O mass fraction with $Le_i = 1$. Experimental measurements with uncertainties taken from the TNF library	96
6.11	Predicted profile of conditional radially averaged N ₂ mass fraction and temperature with $Le_i = 1$. Experimental measurements with uncertainties taken from the TNF library	96
6.12	Predicted profile of conditional radially averaged OH mass fraction with $Le_i = 1$. Experimental measurements with uncertainties taken from the TNF library	97
6.13	Predicted profile of conditional radially averaged NO mass fraction with $Le_i = 1$. Experimental measurements with uncertainties taken from the TNF library	98
6.14	Predicted profile of unconditional Favre averaged H ₂ and H ₂ O mass fraction with $Le_i = 1$. Experimental measurements with uncertainties taken from the TNF library	99
6.15	Predicted profile of unconditional Favre averaged O ₂ and N ₂ mass fraction with $Le_i = 1$. Experimental measurements with uncertainties taken from the TNF library	99
6.16	Predicted profile of unconditional Favre averaged OH mass fraction with $Le_i = 1$. Experimental measurements with uncertainties taken from the TNF library	100
6.17	Predicted profile of unconditional Favre averaged NO mass fraction with $Le_i = 1$. Experimental measurements with uncertainties taken from the TNF library	101
6.18	Predicted profile of unconditional Favre averaged temperature with $Le_i = 1$. Experimental measurements with uncertainties taken from the TNF library	102
6.19	Predicted profiles of conditional means of major species mass fractions with differential diffusion effects at $x/L_v = 1/8$. Experimental measurements taken from the TNF library	103

6.20	Predicted profiles of conditional means of minor species mass fraction and temperature with differential diffusion effects at $x/L_v = 1/8$. Experimental measurements taken from the TNF library	105
6.21	Predicted profiles of conditional means of major species mass fractions with differential diffusion effects at $x/L_v = 1/2$. Experimental measurements taken from the TNF library	106
6.22	Predicted profiles of conditional means of minor species mass fraction and temperature with differential diffusion effects at $x/L_v = 1/2$. Experimental measurements taken from the TNF library	107
6.23	Predicted radial profiles of Favre averaged Bilger's mixture fraction with differential diffusion. Experimental measurements are from the TNF library	109
6.24	Predicted radial profiles of Favre averaged major species mass fraction with differential diffusion effects at $x/L_v = 1/8$. Experimental measurements are from the TNF library	110
6.25	Predicted radial profiles of Favre averaged minor species mass fraction and temperature with differential diffusion effects at $x/L_v = 1/8$. Experimental measurements are from the TNF library	112
6.26	Predicted radial profiles of Favre averaged major species mass fraction with differential diffusion effects at $x/L_v = 1/2$. Experimental measurements are from the TNF library	113
6.27	Predicted radial profiles of Favre averaged minor species mass fraction and temperature with differential diffusion effects at $x/L_v = 1/2$. Experimental measurements are from the TNF library	114
6.28	Predicted profiles of conditional means of H_2 , O_2 , OH , and NO mass fraction with differential diffusion effects (H_2 and H) for various radial positions at $x/L_v = 1/8$, in conserved mixture fraction space.	118
6.29	Predicted profiles of conditional means of H_2 , O_2 , and OH mass fraction with differential diffusion effects (H_2 and H) for various radial positions at $x/L_v = 1/8$, in Bilger's mixture fraction space.	120
6.30	Predicted conditional profiles of independent contributions of $Le_{H_2} = 0.3$ and $Le_H = 0.18$ at $x/L_v = 1/8$, in conserved mixture fraction space.	121
6.31	Budget of terms in CMC equation of Y_{H_2} at $x/L_v = 1/8$	123
6.32	Budget of terms in CMC equation of Y_H at $x/L_v = 1/8$	124

6.33	Budget of terms in CMC equation of Y_{H_2} at $x/L_v = 1/2$	124
6.34	Budget of terms in CMC equation of Y_H at $x/L_v = 1/2$	125
6.35	Budget of terms in CMC equation of h at $x/L_v = 1/8$	126
6.36	Budget of terms in CMC equation of h at $x/L_v = 1/2$	127

Nomenclature

Acronyms

CFD	Computational fluid dynamics
CMC	Conditional moment closure
DNS	Direct numerical simulation
LES	Large eddy simulation
LHS	Left hand side
RANS	Reynolds averaged Navier Stokes
RHS	Right hand side

Abbreviations

Da	Damköhler number
Le	Lewis number
Pe	Peclet number
Re	Reynolds number
Sc	Schmidt number

Greek Symbols

α	Thermal diffusivity
β	Beta distribution
χ	Scalar dissipation rate
δ_{ij}	Kronecker delta
$\dot{\omega}$	Production rate
η	Sample space variable for ξ
μ	Dynamic viscosity
ν	Kinematic viscosity

ϕ	Scalar variable
ψ	Fine-grain pdf
ρ	Density
τ	Time scale
ε	Dissipation rate of k
ξ	Mixture fraction
ξ''^2	Mixture fraction variance

Other Notations

$\langle \mathcal{A} \rangle$	Unconditional average of \mathcal{A}
\mathcal{A}'	Fluctuation of \mathcal{A} about its Reynolds average
\mathcal{A}''	Fluctuation of \mathcal{A} about its Favre average
$\overline{\mathcal{A}}$	Reynolds average of \mathcal{A}
$\widetilde{\mathcal{A}}$	Favre average of \mathcal{A}

Roman Symbols

\mathcal{Y}	Random variable
\mathcal{Z}	Sample space variable for \mathcal{Y}
A	Area
c_p	Constant pressure specific heat
D	Mass diffusivity
d	Nozzle diameter
f_k	Weight factor
h	Enthalpy
J	Conditional flux
j	Flux
k	Turbulent kinetic energy
L_v	Visible flame length
M	Molecular mass
M_η	Diffusion velocity
P	Probability density function
p	Pressure
Q	Favre averaged conditional expectation
R	Gas constant
r	Radial distance from centerline
s_h	Enthalpy production rate

T	Temperature
t	Time
u	Velocity
V	Volume
W	Production rate of ϕ
x	Axial distance from nozzle
Y	Mass fraction
Z	Sample space variable for ϕ

Chapter 1

Introduction

This chapter provides the motivation and objectives of the present study. An outline of the subsequent chapters is also presented.

1.1 Overview

Turbulent combustion plays a vital role in today's high energy demand society due to its presence in most transportation and power generation applications. Over two decades, from 1990 to 2009, rapid growth of energy usage in Canada has been observed in the commercial (37% growth), industrial (17%), and transportation (37%) sectors. Correspondingly greenhouse gas (GHG) emissions have also grown in commercial (29%), industrial (8%), and transportation (36%) [1]. Due to economic, regulatory, health and environmental factors, the research and development of new combustion technologies have been focused on improving fuel economy and reducing atmospheric pollution. As emission regulations and control become progressively rigorous, adequate prediction of pollutant emissions, such as carbon dioxide (CO_2), nitrogen oxides (NO_x), sulfur oxides (SO_x) and unburnt carbon particulates (soot), can prove invaluable in the design of these systems. Experimentation has traditionally been adopted for research and design of combustion systems, since their complexity limits the applicability and accuracy of theoretical calculations. However, repeated experimental studies are costly, especially for testing the magnitudes of different parameter and configurations of complex combustion systems.

With the rapid pace of advancement in computer power, computational fluid dynamics (CFD), the numerical solution of fluid problems, has increasingly become a viable and

sought after tool to complement experimentation in the engineering design process of combustion applications. CFD can also contribute to the improvement of the fundamental understanding of the complex phenomena involved in turbulent combustion that are difficult to observe in experimental studies, which in turn results in more reliable simulations and innovative designs of industrial combustion devices. It is easy to see the motivation for the growing community in numerical combustion research. However, in numerical combustion research, accurate prediction of pollutant formation proves to be a challenging objective to achieve. Complex interactions occur between turbulent mixing, chemical reactions, heat transfer and multiphase fluid leading to a wide range of length and time scales, from the macroscopic to the molecular level, that need to be modelled. In addition, the tradeoff between accuracy and computational cost of modelling approaches serves as the motivation for model development. These challenges drive the ongoing research in numerical combustion.

With rising prices and environmental awareness of conventional fossil fuels (petroleum, natural gas, and coal), interest has risen not only in improving efficiency and emissions of conventional fuel systems, but also in the viability of alternative fuel systems, such as biofuels, hydrogen, alcohols, and more [2]. The growing range of systems with different fuels has also contributed to the surge in combustion research. One alternative fuel that has garnered much attention is the use of hydrogen based fuels, known for being regarded as an emissionless fuel, and sustainable due to its abundance [3]. Though hydrogen fuel is commonly regarded to have zero-emission (product being mostly water, H_2O), this is only true when the oxidizer is pure oxygen. More commonly in practical combustion applications, the oxidizer is air which contains nitrogen (N_2), and reaction with hydrogen will result in small amounts of nitrogen oxides. As such, prediction and reduction of nitrogen oxide emission are hurdles that hydrogen fuel faces. Alternatively, hydrogen has also gained attention not only as a primary fuel, but also as a constituent in conventional fuels systems that acts as a stabiliser of the ignition and combustion processes, thereby reducing emissions in the traditional combustion processes [4]. The development of combustion modelling techniques suitable for the emerging alternative fuels, such as hydrogen fuels, can inevitably help to advance the state of the art.

1.2 Objectives

The history of each turbulent CFD and combustion modelling methods has, for the most part, followed the same progression of advancement. The methods are first developed with a set of assumptions and constraints, and subsequent efforts proceed to assess the

methods for its applicability to different problems and to further develop the methods to push the boundaries of the presupposed constraints. The Conditional Moment Closure method (CMC) is one such combustion modelling approach which has attracted interest in the numerical combustion community. Numerous studies focus on extending the the approach to a wider variety of combustion problems. One assumption regularly made for CMC modelling, as well as many other combustion modelling methods, is that of equal mass diffusivities for every chemical species. The equally diffusive species or unity Lewis assumption is often considered to be valid for sufficiently high Reynolds number turbulent flows and in non-premixed turbulent combustion modelling, leading to convenient relationships between species concentrations and conserved scalar variables, and greatly simplifying the model formulations [5]. However, the validity of this assumption can be questioned when the Reynolds number is moderate and significantly different species diffusivities are present, for example in mixtures containing a highly diffusive component like hydrogen, H_2 , or a less diffusive constituent like soot.

The objectives of the present study are:

- The implementation of a previously derived CMC species transport equation [6, 7] which accounts for the effects of differential diffusion. To the author's best knowledge, the method has not been previously implemented in a CFD simulation of a flame.
- The derivation and implementation of a new formulation for the CMC enthalpy transport equation which also accounts for the effects of differential species diffusion. The derivation of the enthalpy equation follows a similar approach to the derivation of the species equation [6, 7], but the inherent differences between species and enthalpy transport are evident in the resulting CMC equations.
- The assessment of benefits and drawbacks of the CMC model with differential diffusion, by comparison with the experimental data, in its application to a well documented experimental turbulent non-premixed hydrogen-air jet flame in a Reynolds-Averaged Navier-Stokes (RANS) setting. Especially of interest are the predictions of NO production, which have previously been found to be inadequate when differential diffusion effects are disregarded.
- Identification and suggestions of possible areas of investigation for improving the CMC approach for future studies.

1.3 Outline

In Chapter 2 the general background of turbulent combustion modelling is covered. The fundamental concepts should provide sufficient knowledge for the reader to interpret the contents of the subsequent chapters. The topics introduced include the governing equations of fluid flows, statistical concepts for turbulence, and common tools for turbulent non-premixed combustion modelling. Brief presentations are given for various methods in turbulent flow and non-premixed combustion modelling, along with their advantages and shortcomings, so that the reader has an overview of the state of the art.

Chapter 3 is centred on the details of the main phenomenon addressed in this study, differential diffusion. A discussion of the concepts, with a focus on its role turbulent non-premixed combustion, is provided. A review of previous experimental, direct numerical simulation, and numerical modelling studies involving differential diffusion in turbulent non-premixed combustion, and brief discussions on their findings, are presented, as to provide the reader with a perspective of the current progress in the area.

The turbulent combustion modelling approach applied in this study, CMC, is discussed in Chapter 4. A review is given for the derivation procedure for the transport equation of conditional species mass fraction with differential diffusion effects considered. A novel derivation of conditional enthalpy transport equation considering differential species diffusion effects is presented, along with the application of the primary CMC closure hypothesis to the unclosed diffusion terms with differential diffusion. The chapter also covers closure models for other terms in the CMC equations that are used in this study.

Following the development of the CMC equations, Chapter 5 details the general implementation (not specific to a particular flame) of the CMC model with differential diffusion effects. An outline of the solution chronology is provided, illustrating the coupling of the CFD and combustion modelling methods. The numerical methods that are used in the present study, including the finite volume discretisation of the transport equations and the numerical solution of the system of differential equations, are discussed.

The application of the aforementioned modelling method to the investigation of a hydrogen-air jet flame is conducted in Chapter 6. Firstly, an overview of the experimental study of the hydrogen-air jet flame is provided. The details of the numerical setup of parameters related to the flame under investigation are established, including the computational finite volume grid, boundary and initial conditions, CFD model parameters, and chemical mechanism. The remainder of the chapter is dedicated to the presentation and assessment of the results that are obtained for the hydrogen-air flame using the numerical models, by comparison to the experimental data and to calculations disregarding differ-

ential diffusion effects. The assessment includes identifying successes and shortcomings of the application of the model to the experimental test case, and analyzing the plausible causes and, wherever possible, suggesting potential methods for improvement.

Lastly, the current study and its findings are summarized in Chapter 7. Recommendations for future areas of study based on the knowledge that is obtained from the current research are suggested.

Chapter 2

Background

In this chapter, an overview of concepts fundamental to the turbulent combustion modelling is presented. Governing equations for fluid and thermodynamics are presented. One of the main topics in this chapter is the statistical treatment of turbulence; a review of statistics and the statistical representation of the governing equations is covered, as well as insight into the difficulties that arise from the statistical representation. An emphasis is placed on turbulent non-premixed reacting flow modelling, and various turbulence and combustion modelling techniques are briefly introduced.

2.1 Principles of Turbulent Combustion

2.1.1 Classification of Combustion Processes

Combustion processes involve the exothermic chemical reaction between a fuel and an oxidizer (reactants) in a mixture, resulting in the production various chemical products. It is useful to classify these processes based on their characteristics. It is common to categorize the combustion processes based on when combustion occurs in relation to the mixing of the fuel and oxidizer.

In premixed flames, the fuel and the oxidizer are homogeneously mixed before ignition occurs. The mixture is stoichiometric when the fuel and oxidizer are completely consumed in the combustion process. When there is excess fuel or oxidizer, the mixture is fuel-rich or fuel-lean, respectively. The premixture can be described by the equivalence ratio, which relates the composition of the mixture to the stoichiometric mixture. The fresh

and burnt mixtures are separated by a reaction zone which, with sufficient heat release, self-propagates and consumes the unburnt mixture.

In non-premixed flames, the fuel and the oxidizer are mixed as combustion is occurring; hence, combustion occurs across a range of equivalence ratios. This results in a more complex chemistry due to the presence of both rich and lean burning. Unlike the self-propagating nature of the reaction zone in premixed combustion, the reaction zone in non-premixed combustion occurs at the interface of the fuel and oxidizer and its structure is governed by the fluid dynamics of the mixing process.

Both types of combustion processes have advantages and disadvantages. Premixed combustion processes are more efficient than non-premixed processes due to the ability to restrict the chemistry that occurs by controlling the composition of the premixture. The advantage of non-premixed combustion processes is better safety than premixed processes, since the reactants are initially separated, preventing accidental ignition. It is also easier to control non-premixed processes after ignition has occurred, since the flame does not self-propagate.

Most commonly studied flames can also be classified by whether the fluid flow governing the mixing process is laminar or turbulent. Mixing in turbulent flames is enhanced due to turbulent eddies, resulting in greater transport of mass, momentum, and heat. Examples of combustion systems that are classified under premixed or non-premixed, and turbulent or laminar, are given in Table 2.1.

2.1.2 Governing Equations of Transport Phenomena and State Equations

The present description of the governing equations of mass, momentum, species, and enthalpy transport in turbulent combustion phenomena adopts an Eulerian viewpoint, though a Lagrangian viewpoint is equally valid, and in some cases more convenient.

Transport of mass

The equation for the conservation of mass, or the continuity equation, can be expressed as

$$\frac{\partial \rho}{\partial t} + \nabla \cdot (\rho \mathbf{u}) = 0, \quad (2.1)$$

where ρ is the density and \mathbf{u} is the velocity vector field. Equation 2.1 states that the rate of change in mass of the control volume is equal to the net rate of flow into the control volume.

Table 2.1: Classification of combustion systems

	Laminar	Turbulent
Premixed	<ul style="list-style-type: none"> • Flat flame • Bunsen burner 	<ul style="list-style-type: none"> • Spark ignition engine • Gas turbines
Non-premixed	<ul style="list-style-type: none"> • Wood fire • Radiant burners • Candle 	<ul style="list-style-type: none"> • Coal combustion • Aircraft turbine • Diesel engine • Rocket engine • Furnaces

Transport of Linear Momentum

The transport of linear momentum can be described by

$$\frac{\partial \rho \mathbf{u}}{\partial t} + \nabla \cdot (\rho \mathbf{u} \mathbf{u}) = -\nabla p + \nabla \cdot \boldsymbol{\tau} + \mathbf{B}. \quad (2.2)$$

The two terms on the left hand side (LHS) of Eq. 2.2 are the material derivative describing the local and advection rates of change in momentum in the control volume. The terms on the right hand side (RHS) are the forces acting on the control volume, consisting of a pressure gradient, stress tensor, and body forces. Equation 2.2 describes a system of N equations, where N is the number of spatial components of \mathbf{u} , commonly known as the Navier-Stokes equations.

The total stress tensor for Newtonian fluids (where the viscous stresses are proportional to the strain rates) is

$$\boldsymbol{\tau} = \mu \left(\frac{\partial u_i}{\partial x_j} + \frac{\partial u_j}{\partial x_i} \right) + \lambda \frac{\partial u_k}{\partial x_k} \delta_{ij}, \quad (2.3)$$

where λ is the bulk viscosity, and δ_{ij} is the Kronecker delta. λ is commonly approximated as $-\frac{2}{3}\mu$ [8].

Transport of Species

The mass fraction Y of a chemical species i is the ratio of the mass of the species to the mass of the mixture. The sum of the mass fraction of N species is equal to 1,

$$\sum_i^N Y_i = 1. \quad (2.4)$$

The transport of a species i is expressed by the equation

$$\frac{\partial \rho Y_i}{\partial t} + \nabla \cdot (\rho \mathbf{u} Y_i) = -\nabla \cdot \mathbf{j}_i + \rho \dot{\omega}_i, \quad (2.5)$$

where \mathbf{j}_i is the species diffusion flux, and $\dot{\omega}_i$ is the rate of production or destruction of the species due to chemical reactions. The terms on the LHS of Eq. 2.5 account for the temporal rate of change of h , and the advection of h . The species diffusion flux involves different modes of diffusion: ordinary diffusion due to concentration gradients, thermophoretic (Soret) diffusion due to temperature gradients, pressure diffusion due to pressure gradients, and forced diffusion due to differences in body forces, and can be summarized as,

$$\mathbf{j}_i = \mathbf{j}_i^d + \mathbf{j}_i^T + \mathbf{j}_i^P + \mathbf{j}_i^f, \quad (2.6)$$

where the superscripts d , T , P , and f denote ordinary, thermophoretic, pressure, and forced diffusion, respectively. Pressure gradients are typically not large enough in combustion processes for pressure diffusion to be significant. Forced diffusion, generally caused by charged species, is also negligible in most combustion processes. Thermophoretic diffusion is important for light species such as hydrogen, but only at lower temperatures [9]. The ordinary diffusion component is commonly approximated using Fick's law for binary diffusion,

$$\mathbf{j}_i^d = -\rho D_i \nabla Y_i, \quad (2.7)$$

where D_i is the binary diffusion coefficient of species i and a reference species. The governing equation for species transport, where only \mathbf{j}_i^d is important in \mathbf{j}_i , is obtained from using Eqs. 2.5-2.7,

$$\frac{\partial \rho Y_i}{\partial t} + \nabla \cdot (\rho \mathbf{u} Y_i) = \nabla \cdot (\rho D_i \nabla Y_i) + \rho \dot{\omega}_i. \quad (2.8)$$

Transport of Enthalpy

Enthalpy describes the thermodynamic potential of a system. The enthalpy h of the mixture is the mass weighted sum of the individual specific enthalpy h_i of species i ,

$$h = \sum_i Y_i h_i. \quad (2.9)$$

The standardized or total enthalpy of a species i is given as

$$\bar{h}_i(T) = \bar{h}_{f,i}^o(T_{ref}) + \delta\bar{h}_{s,i}(T_{ref}), \quad (2.10)$$

where $\bar{h}_{f,i}^o(T_{ref})$ is the enthalpy of formation at the reference state, describing the energy potential in the chemical bonds, and $\delta\bar{h}_{s,i}(T_{ref})$ is the sensible enthalpy, describing the amount of energy needed to change the temperature from T_{ref} to T . The transport of enthalpy in a system is expressed by the equation

$$\frac{\partial \rho h}{\partial t} + \nabla \cdot (\rho \mathbf{u} h) = -\nabla \cdot j_q + \rho s_h + \Phi_v + \frac{Dp}{Dt}, \quad (2.11)$$

where ρ is the density, \mathbf{u} is the velocity vector, j_q is the heat diffusion flux, s_h is the heat source, Φ_v is the viscous heating, and $\frac{Dp}{Dt}$ is the material derivative of pressure. The terms on the LHS of Eq. 2.11 account for the temporal rate of change of h , and the advection of h . For constant pressure flames, the last term of the RHS involving changes in pressure, is neglected. Φ_v is negligible for low Mach numbers [10]. In turbulent combustion, the enthalpy source term usually accounts for heating due to radiation, though in general electrical sources can be included. The heat diffusion flux involves the following modes of diffusion: heat conduction, species diffusion, and Dufour effects caused by concentration gradients, and can be summarized by the relationship

$$j_q = j_q^c + j_q^d + j_q^D. \quad (2.12)$$

Dufour effects are typically negligible in most cases, and j_p can be expressed by,

$$j_q = -\lambda \nabla T + \sum_i h_i j_i, \quad (2.13)$$

where λ is the thermal conductivity and j_i is the the species diffusion flux from Eq. 2.6. The terms on the RHS describe the contributions of heat conduction (Fourier's law) and species diffusion, respectively. ∇T in Eq. 2.13 can be expressed in terms of h by the use of Eq. 2.9, and along with the expression for j_i in Eq. 2.7, j_q can be expressed as [11],

$$j_q = -\rho\alpha\nabla h + \sum_i \rho h_i (\alpha - D_i) \nabla Y_i, \quad (2.14)$$

where α is the thermal diffusivity, Y_i is the mass fraction of the i th chemical species, D_i is its diffusion coefficient, and h_i is its enthalpy. The resulting governing equation for enthalpy transport, neglecting viscous heating, pressure changes, and Dufour effect, is

$$\frac{\partial \rho h}{\partial t} + \nabla \cdot (\rho \mathbf{u} h) = \nabla \cdot (\rho \alpha \nabla h) - \nabla \cdot \sum_i \rho h_i (\alpha - D_i) \nabla Y_i + \rho s_h. \quad (2.15)$$

Equations of State

Other than the transport of quantities, it is useful to relate various state properties to each other. Various equations from thermodynamics are commonly used in conjunction with the transport equations.

The ideal gas law is an equation of state relating the pressure, volume and temperature of a gas, under the assumption of ideal gas behaviour, stated as

$$p = \frac{nRT}{V} = \frac{\rho RT}{M}, \quad (2.16)$$

where p is the pressure, n is the number of moles, T is the temperature, ρ is the density, M is the molar mass, and $R = 8.314 \frac{\text{J}}{\text{K}\cdot\text{mol}}$ is the ideal gas constant. The ideal gas law assumes negligible molecular size and intermolecular attractions, and works well for gases with low density and high temperatures.

The calorific equations of state are equations relating the internal energy and enthalpy to pressure and temperature. For an ideal gas, the equations are

$$u - u_{ref} = \int_{T_{ref}}^T c_v dT, \quad (2.17)$$

and

$$h - h_{ref} = \int_{T_{ref}}^T c_p dT, \quad (2.18)$$

where c_v is the constant volume specific heat and c_p is the constant pressure specific heat, both of which are functions of temperature.

2.1.3 Statistical Description of Turbulence

The instantaneous equations of Section 2.1.2 are sufficient to describe the deterministic nature of fluid flows for any Reynolds number. However, the distinguishing feature of turbulent flows is the seemingly chaotic fluctuations in its properties, as opposed to in laminar flows where the fluctuations are dampened by viscous effects. Any small perturbation in the system results in drastic changes in the state of the system. As turbulence intensifies, quantified by an increasing Reynolds number, the range of energy containing scales widens, leading to greater sensitivity of the system to initial and boundary conditions. In experiments, it is impossible to know or control the exact initial and boundary conditions. Experimental results of turbulent flow studies are presented as statistics of numerous trials. In numerical studies of turbulent flows, it is impractical, and for most engineering applications impossible, to fully resolve the details of the flow. Subsequently, turbulence is, in most cases, treated statistically as a random dynamical process. The randomly fluctuating (stochastic) flow quantities, such as velocity and reactive chemical species, can take on a value in a set of possible values described by their probability. In this section, a brief review of basic concepts in statistics is presented.

Probability Density Functions

In turbulent combustion modelling, the velocity and scalars are stochastic variables that can take on a set of different values within the sample space. The stochastic variables can either be discrete, taking on certain values, or continuous, taking on any of an uncountably infinite number of values within the range of the sample space. These possible values of a stochastic variable can be described by their probabilities. The cumulative probability of a stochastic variable \mathcal{Y} is the probability of the event in which \mathcal{Y} takes on a value less than or equal to a particular value of the sample space variable \mathcal{Z} , given by

$$F(\mathcal{Z}) = \text{prob}(\mathcal{Y} < \mathcal{Z}), \quad (2.19)$$

and its values over all \mathcal{Z} constitute the cumulative distribution function (CDF). The derivative of the CDF of a continuous stochastic variable is its probability density function (PDF), which maps the density of the probability around values in the sample space;

$$P(\mathcal{Z}) = \frac{dF(\mathcal{Z})}{d\mathcal{Z}}. \quad (2.20)$$

Figure 2.1 shows an example of the CDF and PDF of a Gaussian distribution. The probability of the stochastic variable being within some infinitesimal range $d\mathcal{Z}$ is given by the

product of $P(\mathcal{Z})$ and $d\mathcal{Z}$, such that

$$\text{prob}(\mathcal{Z} \leq \mathcal{Y} < \mathcal{Z} + d\mathcal{Z}) = P(\mathcal{Z})d\mathcal{Z}. \quad (2.21)$$

A property of the PDF is that the sum of the density over the entire space is equal to 1;

$$\int_{-\infty}^{\infty} P(\mathcal{Z})d\mathcal{Z} = 1. \quad (2.22)$$

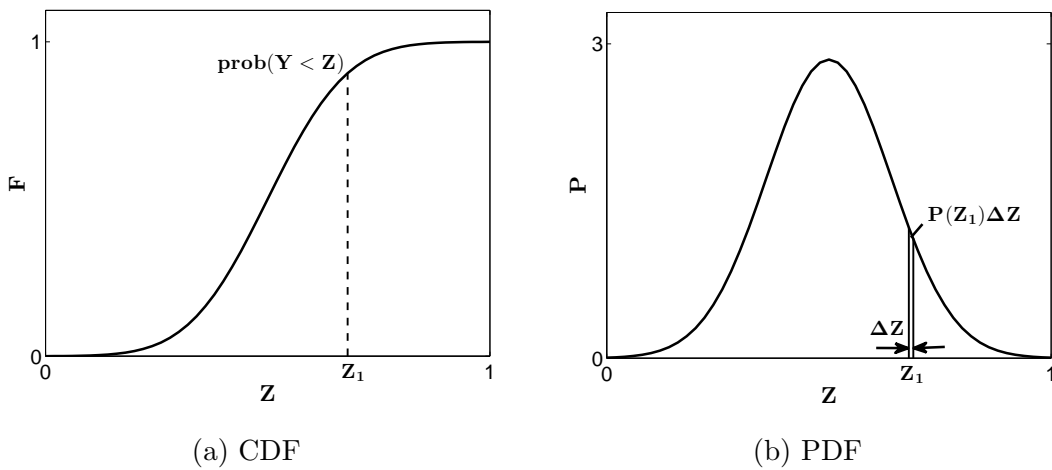


Figure 2.1: CDF and PDF of Gaussian distribution

Moments

Moments are important concepts in stochastic variables which characterize a set of points. The moments of the PDF describes the features of the distribution. The n th moment of the PDF about a value c is given by,

$$\mu'_n = \int_{-\infty}^{\infty} (\mathcal{Z} - c)^n P(\mathcal{Z})d\mathcal{Z}. \quad (2.23)$$

The n th moment of the PDF about zero is called the expected value of \mathcal{Y}^n ,

$$E(\mathcal{Y}^n) = \int_{-\infty}^{\infty} \mathcal{Z}^n P(\mathcal{Z})d\mathcal{Z}. \quad (2.24)$$

The expected value of \mathcal{Y} , or the first moment of the PDF about zero is, is the mean of \mathcal{Y} , which describes the central tendency of the distribution,

$$\langle \mathcal{Y} \rangle = \int_{-\infty}^{\infty} \mathcal{Z} P(\mathcal{Z}) d\mathcal{Z}. \quad (2.25)$$

For any deterministic function $f(\mathcal{Y})$ of stochastic variable \mathcal{Y} , the mean is

$$\langle f(\mathcal{Y}) \rangle = \int_{-\infty}^{\infty} f(\mathcal{Z}) P(\mathcal{Z}) d\mathcal{Z}. \quad (2.26)$$

The fluctuation of \mathcal{Y} about its mean $\langle \mathcal{Y} \rangle$ is denoted by,

$$\mathcal{Y}' = \mathcal{Z} - \langle \mathcal{Y} \rangle. \quad (2.27)$$

The variance, which characterizes the spread of the distribution about the mean, is given by the second moment about the mean, or the central second moment,

$$\langle \mathcal{Y}'^2 \rangle = \int_{-\infty}^{\infty} (\mathcal{Z} - \langle \mathcal{Y} \rangle)^2 P(\mathcal{Z}) d\mathcal{Z}. \quad (2.28)$$

Joint Probability Density Functions

For multivariate stochastic variable \mathbf{Y} , where $\mathbf{Y} = (\mathcal{Y}_1, \mathcal{Y}_2, \dots, \mathcal{Y}_n)^T$ is a set of n stochastic variables on the same probability space, the probability of $\mathcal{Y}_1 < \mathcal{Z}_1, \mathcal{Y}_2 < \mathcal{Z}_2, \dots, \mathcal{Y}_n < \mathcal{Z}_n$, where $\mathbf{Z} = (\mathcal{Z}_1, \mathcal{Z}_2, \dots, \mathcal{Z}_n)^T$ is the set of sample space variables corresponding to each stochastic variable, is the joint cumulative probability function,

$$F(\mathbf{Z}) = \text{prob}(\mathcal{Y}_1 < \mathcal{Z}_1, \mathcal{Y}_2 < \mathcal{Z}_2, \dots, \mathcal{Y}_n < \mathcal{Z}_n). \quad (2.29)$$

The density of the probabilities in the probability space is mapped by the joint probability density function, which is given by the n th order derivative of the joint CDF,

$$P(\mathbf{Z}) = \frac{\partial^n F(\mathbf{Z} < \mathbf{Z})}{\partial \mathcal{Z}_1 \partial \mathcal{Z}_2 \dots \partial \mathcal{Z}_n}. \quad (2.30)$$

Once again, the integration of the joint PDF across the entire probability space is equal to 1,

$$\int_{\mathbf{Z}} P(\mathbf{Z}) d\mathbf{Z} = 1. \quad (2.31)$$

If the stochastic variables are statistically independent, then their events are independent of each other, and the PDF is simply the product of the individual single-variable PDFs,

$$P(\mathcal{Z}_1, \mathcal{Z}_2, \dots, \mathcal{Z}_n) = P(\mathcal{Z}_1)f(\mathcal{Z}_2)\dots f(\mathcal{Z}_n). \quad (2.32)$$

The expected value of a function $f(\mathcal{Y}_1, \mathcal{Y}_2, \dots, \mathcal{Y}_n)$ is obtained by integration over all sample spaces,

$$\langle f(\mathcal{Y}_1, \mathcal{Y}_2, \dots, \mathcal{Y}_n) \rangle = \int_{\mathcal{Z}} f(\mathcal{Z}_1, \mathcal{Z}_2, \dots, \mathcal{Z}_n)P(\mathcal{Z}_1, \mathcal{Z}_2, \dots, \mathcal{Z}_n)d\mathcal{Z}_1d\mathcal{Z}_2\dots d\mathcal{Z}_n. \quad (2.33)$$

Conditional Probability Density Functions and Conditional Averaging

A conditional probability is the probability of an event \mathcal{A} of the stochastic variable \mathcal{Y}_1 occurring, determined for particular realizations \mathcal{B} of the stochastic variable \mathcal{Y}_2 , such that

$$P(\mathcal{A}|\mathcal{B}) = \frac{P(\mathcal{A}, \mathcal{B})}{P(\mathcal{B})}. \quad (2.34)$$

For example, the conditional PDF $P(\mathcal{Z}_1|\mathcal{Y}_2 = \mathcal{Z}_2)$ is the probability density of \mathcal{Y}_1 around the sample space variable \mathcal{Z}_1 given the realization that the stochastic variable \mathcal{Y}_2 is equal to the state space variable \mathcal{Z}_2 . The joint PDF can be expressed as the conditional PDF multiplied by the single variable PDF across all realizations,

$$P(\mathcal{Z}_1, \mathcal{Z}_2) = P(\mathcal{Z}_1|\mathcal{Y}_2 = \mathcal{Z}_2)P(\mathcal{Z}_2). \quad (2.35)$$

The conditional expectation $\langle \mathcal{Y}_1|\mathcal{B} \rangle$ of \mathcal{Y}_1 is the average of \mathcal{Y}_1 over the sub-ensemble of the particular realizations \mathcal{B} . For example, the conditional expectation of \mathcal{Y}_1 on the realization of $\mathcal{Y}_2 = \mathcal{Z}_2$ is given by

$$\langle \mathcal{Y}_1|\mathcal{Y}_2 = \mathcal{Z}_2 \rangle = \int_{-\infty}^{\infty} \mathcal{Z}_1P(\mathcal{Z}_1|\mathcal{Y}_2 = \mathcal{Z}_2)d\mathcal{Z}_1. \quad (2.36)$$

The unconditional mean of \mathcal{Y}_1 can also be obtained from the conditional mean by integration over all realizations of \mathcal{Y}_2 ,

$$\langle \mathcal{Y}_1 \rangle = \int_{-\infty}^{\infty} \langle \mathcal{Y}_1|\mathcal{Y}_2 = \mathcal{Z}_2 \rangle P(\mathcal{Z}_2)d\mathcal{Z}_2. \quad (2.37)$$

2.1.4 Averaging Transport Equations

The statistical treatment of an instantaneous quantity in turbulent fluid flows involves the decomposition of the quantity into its mean and fluctuations about the mean. The decomposition of instantaneous quantities is applied to the governing transport equations. Two averaging techniques are described in the following sections.

Reynolds Averaging

A stochastic quantity ϕ can be decomposed into a time average and fluctuation about the average,

$$\phi(x_k, t) = \bar{\phi}(x_k) + \phi'(x_k, t), \quad (2.38)$$

where $'$ denotes the fluctuation about the average value. The process in Eq. 2.38 is known as Reynolds decomposition, and a graphical example is shown in Fig. 2.2. Reynolds averaging is typically used in non-reacting flows, where density fluctuations are negligible. The ensemble average is the average of the quantity over a sample size of N , defined by

$$\bar{\phi}(x_k, t) = \frac{1}{N} \sum_{i=1}^N \phi^i(x_i, t). \quad (2.39)$$

The average of the fluctuations is zero, such that $\overline{\phi'}(x_i, t) = 0$.

Favre Averaging

In turbulent flows with significant density fluctuations, such as in reacting flows due to large changes in temperature, Reynolds averaging results in correlations of the form $\overline{\rho'\phi'}$ which can not be neglected. These correlations can be neglected by the use of density-weighted averaging, also known as Favre averaging. The Favre average is given by

$$\tilde{\phi} = \frac{\overline{\rho\phi}}{\bar{\rho}}. \quad (2.40)$$

Though the use of Favre averaging is common in reacting flows, it is difficult to relate the quantities to Reynolds-averaged quantities, since a relation between the Favre averaged and Reynolds-averaged quantity requires the density correlations to be known, where

$$\bar{\rho}\tilde{\phi} = \bar{\rho}\bar{\phi} + \overline{\rho'\phi'}. \quad (2.41)$$

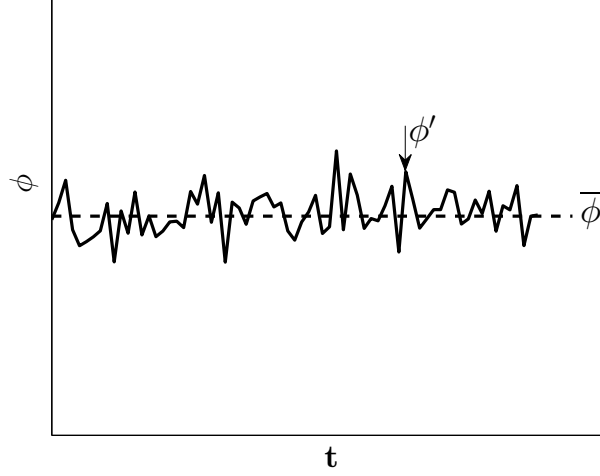


Figure 2.2: Reynolds decomposition of point scalar measurement

Decomposition with Favre averaging results in

$$\phi(x_k, t) = \tilde{\phi}(x_k, t) + \phi''(x_k, t), \quad (2.42)$$

where $''$ denotes fluctuations about the Favre average. The Favre averaged form of the transport equations (Eqs. 2.1, 2.2, 2.8, and 2.15) are

Mass:

$$\frac{\partial \bar{\rho}}{\partial t} + \nabla \cdot (\bar{\rho} \tilde{\mathbf{u}}) = 0. \quad (2.43)$$

Linear momentum:

$$\frac{\partial \bar{\rho} \tilde{\mathbf{u}}}{\partial t} + \nabla \cdot (\bar{\rho} \tilde{\mathbf{u}} \tilde{\mathbf{u}}) + \nabla \cdot (\bar{\rho} \tilde{\mathbf{u}}'' \tilde{\mathbf{u}}'') = -\nabla \bar{p} + \nabla \cdot \bar{\boldsymbol{\tau}} + \bar{\mathbf{B}}. \quad (2.44)$$

Species:

$$\frac{\partial \bar{\rho} \tilde{Y}_i}{\partial t} + \nabla \cdot (\bar{\rho} \tilde{\mathbf{u}} \tilde{Y}_i) + \nabla \cdot (\bar{\rho} \tilde{\mathbf{u}}'' \tilde{Y}_i'') = \nabla \cdot (\bar{\rho} D_i \nabla \tilde{Y}_i) + \bar{\rho} \bar{\omega}_i. \quad (2.45)$$

Enthalpy:

$$\frac{\partial \bar{\rho} \tilde{h}}{\partial t} + \nabla \cdot (\bar{\rho} \tilde{\mathbf{u}} \tilde{h}) + \nabla \cdot (\bar{\rho} \tilde{\mathbf{u}}'' \tilde{h}'') = \nabla \cdot (\bar{\rho} \alpha \nabla \tilde{h}) - \nabla \cdot \left(\sum_i \bar{\rho} \tilde{h}_i (\alpha - D_i) \nabla \tilde{Y}_i \right) + \bar{\rho} \bar{s}_h. \quad (2.46)$$

2.2 Computational Fluid Dynamics of Turbulent Flows

The prevalence of turbulent flows in engineering applications has substantially driven the development of numerical methods for analyzing such flows. The immense complexity of turbulence has made it impossible to solve the governing physics of the flow (Section 2.1.2) without simplifications; instead statistical approaches (Section 2.1.3) allow methods that require less computational power. A few of the most well-known computational methods for turbulent flows are presented in this section.

2.2.1 Direct Numerical Simulation

Direct Numerical Simulations (DNS) treats any fluid flow deterministically, such that the state of the system is completely resolved, instead of described by a probability distribution. This involves the solution at all scales in the flow. Any fluctuations are due to perturbations to initial or boundary conditions, or due to noise cause by discretization. The spatial grid and timesteps must be adequately fine to capture the smallest turbulent eddies. As the Reynolds number of the flow increases, the energy scale widens and the smallest eddy decreases in size, therefore an increasingly finer grid is required. Due to the large range of scales involved in turbulent flows, the computational resources required for DNS severely limits its use. Though the use of DNS to most industrial applications is unrealistic with current computing technologies, DNS can be useful in aiding the development of turbulence models, as well as in the validation of the models. The analysis of turbulent flames using DNS is limited to simple configurations; further information on the use of DNS in reacting flows can be found in [12, 13, 14, 15, 16]

2.2.2 RANS Modelling

The Reynolds Averaged Navier Stokes equations contain the non-linear correlations $\overline{\mathbf{u}'\mathbf{u}'}$ collectively known as the Reynolds stresses; and correspondingly, the Favre averaged form $\widetilde{\mathbf{u}''\mathbf{u}''}$ in Eq. 2.44. Various turbulence models have been used to predict the Reynolds stresses in order to close the RANS equations. Most of the RANS models rely on the turbulent viscosity hypothesis proposed by Joseph Boussinesq in 1872, which assumes that effects of the Reynolds stresses on the mean flow are analogous to the effects of viscous stress proportional to the rate of deformation of fluid elements. This enables the Reynolds

stresses to be described by the mean velocity gradients, such that

$$\tau_{ij} = -\overline{\rho u'_i u'_j} = \mu_t \left(\frac{\partial U_i}{\partial x_j} + \frac{\partial U_j}{\partial x_i} \right) - \frac{2}{3} \rho k \delta_{ij}, \quad (2.47)$$

where $\mu_t = \rho \nu_t$. Although the assumption is poor for many complex flows, reasonable predictions can be obtained for simple shear flows.

Mixing Length Model

The mixing length model, developed by Prandtl in 1925, does not require the solution of any additional transport equations. The assumption is made that the turbulence occurs in a single velocity scale and a single length scale. Dimensional analysis of the turbulent viscosity ν_t with dimensions of $\frac{m^2}{s}$ show that it can be expressed by the product of the turbulent velocity scale v_t with dimensions $\frac{m}{s}$ and the turbulent length scale l_t with dimension m ,

$$\nu_t = C v_t l_t. \quad (2.48)$$

For flows exhibiting two dimensional turbulence such that the $\tau_{xy} = \tau_{yx} = -\overline{\rho u'v'}$ are the only significant Reynolds stresses and only one component of the velocity gradient is significant, the velocity scale can be described by

$$v_t = c l_t \left| \frac{\partial U}{\partial y} \right|. \quad (2.49)$$

Combining Eqs. 2.48 and 2.49, while absorbing the constants into l_t results in

$$\nu_t = l_t^2 \left| \frac{\partial U}{\partial y} \right|. \quad (2.50)$$

Because most of the turbulent kinetic energy is in the largest eddies, l_t is taken as the length scale of the largest eddies corresponding to the mixing length l_m . The Reynolds stresses are

$$\tau_{xy} = \tau_{yx} = -\overline{\rho u'v'} = \rho l_m^2 \left| \frac{\partial U}{\partial y} \right| \frac{\partial U}{\partial y}. \quad (2.51)$$

k - ε model

One of the most well known and used RANS model is the k - ε model [17, 18, 19]. The turbulent kinetic energy k is

$$\frac{1}{2} \left(\overline{u'^2} + \overline{v'^2} + \overline{w'^2} \right). \quad (2.52)$$

The turbulent eddy viscosity is given by

$$\mu_t = \rho C_\mu \frac{k^2}{\varepsilon}. \quad (2.53)$$

The transport equation for k and ε are [17]:

$$\frac{\partial \rho k}{\partial t} + \nabla \cdot (\rho k \mathbf{u}) = \nabla \cdot \left(\frac{\mu_t}{\sigma_k} \nabla k \right) + 2\mu_t S_{ij} \cdot S_{ij} \cdot S_{ij} - \rho \varepsilon, \quad (2.54)$$

and

$$\frac{\partial \rho \varepsilon}{\partial t} + \nabla \cdot (\rho \varepsilon \mathbf{u}) = \nabla \cdot \left(\frac{\mu_t}{\sigma_\varepsilon} \nabla \varepsilon \right) + C_{\varepsilon 1} \frac{\varepsilon}{k} 2\mu_t S_{ij} \cdot S_{ij} - C_{\varepsilon 2} \rho \frac{\varepsilon^2}{k}. \quad (2.55)$$

The standard values for the adjustable constants are $C_\mu = 0.09$, $\sigma_k = 1.00$, σ_ε , $C_{\varepsilon 1} = 1.44$, $C_{\varepsilon 2} = 1.92$. The k - ε model is known to have difficulties in modeling certain types of flows such rotating flows, curved boundary layers, and axisymmetric jets [19]. However, due to its computational efficiency, the k - ε model is one of the most commonly used turbulence models.

Reynolds Stress Model

For flows with complex strain fields, the Reynolds stresses τ_{ij} are not well predicted. The Reynolds Stress Model (RSM) does not use the the eddy viscosity hypothesis to approximate the Reynolds stresses. The following system of equations is solved for the Reynolds stresses,

$$\underbrace{\frac{\partial \rho \overline{u'_i u'_j}}{\partial t}}_{\text{Rate of change}} + \underbrace{\frac{\partial \rho u_i \overline{u'_j u'_j}}{\partial x_i}}_{\text{Advection}} = \underbrace{D_{ij}}_{\text{Diffusion}} + \underbrace{P_{ij}}_{\text{Production}} - \underbrace{\varepsilon_{ij}}_{\text{Dissipation}} + \underbrace{\Pi_{ij}}_{\text{Pressure-strain}} + \underbrace{\Omega_{ij}}_{\text{Rotation}}. \quad (2.56)$$

The details of the exact form of terms on the RHS of Eq. 2.56 can be found in various reference texts on CFD methods, such as [19]. RSM requires higher computational costs than other RANS modelling approaches, but has the advantage of being more general. Though the approach fair better for many types of flows, it still suffers in accuracy for flows where ε is poorly predicted by its transport equation, such as axisymmetric jets [19].

2.2.3 Large Eddy Simulation

Large Eddy Simulation (LES) resolves the larger eddies in the flow, while the small eddies are modelled. The large and small eddies are separated by a spatial filtering, which filters out the small eddies from the unsteady Navier-Stokes equations. The interaction between the large eddies, which are resolved from the filtered Navier-Stokes equations, and the small eddies are described by subgrid-scale (SGS) stresses. There are various models proposed for modelling the SGS stresses [19].

The unsteady nature of LES, along with grid spacing requirements proportional to the filter width, result in significantly higher computational resources than most RANS modelling approaches. Additionally, LES is three-dimensional, and therefore computations can not be performed in two-dimensions for many flows that can otherwise be done in RANS modelling. Though computational requirements are high, the recent rapid improvements in computing technologies have increased interest in LES.

2.3 Turbulent Non-premixed Reacting Flow Modelling

The complex nature of turbulent reacting flows requires the use of concepts and tools to aid in the numerical analysis of such problems. In this section, key concepts in the modelling of turbulent non-premixed combustion are briefly presented.

2.3.1 Turbulence-Chemistry Interaction

The consideration of combustion adds to the complexity in the prediction of turbulent flows, due to the fluctuations in the species concentrations from the consumption and production of species, and fluctuations in temperature from the exothermic reactions. The sensitive coupling between reaction rates, temperature, and species concentrations demand

reliable predictions of reactant and heat transport due to turbulent and molecular motion. An important dimensionless number is the Damköhler number,

$$Da = \frac{\text{Diffusive time scale}}{\text{Chemical time scale}} = \frac{\tau_t}{\tau_c}, \quad (2.57)$$

which describes the ratio of the time scales of turbulent transport τ_t to the time scales of chemical reactions τ_c . When $Da \gg 1$, the time needed for chemical reactions to occur is less than the time needed turbulent transport. Equivalently, the reaction rates are greater than the advection rates; as such, reacting flows with high Da are known as fast chemistry flames. A characteristic of fast chemistry non-premixed flames is a thin reaction zone. Conversely, $Da \ll 1$ corresponds to large times for chemical reactions compared to advection. The limit of $Da \rightarrow 0$ corresponds to pure mixing without combustion, since chemical time scales are infinitely large (will not occur).

2.3.2 Mixture Fraction

The structure of the non-premixed flame is dependent on the mixing between the fuel and oxidizer. The mixture fraction ξ is a major concept in non-premixed combustion, and plays a role in most models. The mixture fraction allows the mixing of all reactive scalars to be described by the evolution of a single variable. There is no universal definition of ξ ; various definitions have been proposed under different assumptions. In the mixing of two fluid streams, ξ is defined as the ratio of the fuel stream mass flux to the sum of the mass flux of the fuel and oxidizer mass fluxes,

$$\xi = \frac{\dot{m}_f}{\dot{m}_f + \dot{m}_o}. \quad (2.58)$$

In non-reacting multi-component flows, the species mass fractions are linearly related to the mixture fraction. If the streams have different temperatures, the temperature is also linearly related to the mixture fraction. In reacting flows, the mixture fraction is linearly related to the atomic mass fractions and the standardized enthalpy. When the chemical species are assumed to diffuse at equal rates, ξ is a conserved scalar, known as a Schwab-Zel'dovich variable [20]. The use of the mixture fraction allows a description of turbulent mixing. For flames far from extinction and ignition limits, the reaction zone is located near mixture fractions corresponding to stoichiometric compositions. The transport equation for the instantaneous mixture fraction is

$$\frac{\partial \rho \xi}{\partial t} + \nabla \cdot (\rho \mathbf{u} \xi) = \nabla \cdot (\rho D_\xi \nabla \xi), \quad (2.59)$$

where D_ξ is the diffusivity of ξ . The lack of a source term indicates that ξ is conserved. Without the assumption of equal species diffusivities, the validity of a conserved mixture fraction is debatable, though theoretical studies have suggested that a definition of a conserved mixture fraction exists [21]. The transport equation for the Favre averaged mixture fraction is

$$\frac{\partial \bar{\rho} \tilde{\xi}}{\partial t} + \nabla \cdot (\bar{\rho} \tilde{\mathbf{u}} \tilde{\xi}) + \nabla \cdot (\bar{\rho} \tilde{\mathbf{u}}'' \tilde{\xi}'') = \nabla \cdot (\bar{\rho} D_\xi \nabla \tilde{\xi}), \quad (2.60)$$

where the turbulent flux $\tilde{\mathbf{u}}'' \tilde{\xi}''$ is modelled by the gradient diffusion hypothesis

$$\tilde{\mathbf{u}}'' \tilde{\xi}'' = -D_t \nabla \tilde{\xi}. \quad (2.61)$$

The transport equation for the mean mixture fraction variance $\tilde{\xi}''^2$ is

$$\frac{\partial \bar{\rho} \tilde{\xi}''^2}{\partial t} + \nabla \cdot (\bar{\rho} \tilde{\mathbf{u}} \tilde{\xi}''^2) + \nabla \cdot (\bar{\rho} \tilde{\mathbf{u}}'' \tilde{\xi}''^2) + 2\bar{\rho} \tilde{\mathbf{u}} \tilde{\xi}'' \cdot \nabla \tilde{\xi} + 2\bar{\rho} D_\xi \nabla \tilde{\xi}'' \cdot \nabla \tilde{\xi}'' = 0, \quad (2.62)$$

where the turbulent flux $\tilde{\mathbf{u}}'' \tilde{\xi}''^2$ is modelled using the gradient diffusion hypothesis. The last term on the LHS of Eq. 2.62 is the mean scalar dissipation rate $\tilde{\chi}$.

2.3.3 Scalar Dissipation Rate

The scalar dissipation rate is

$$\tilde{\chi} \equiv 2D \nabla \phi'' \cdot \nabla \phi'', \quad (2.63)$$

where ϕ is a scalar variable (ξ in Eq. 2.62) and D is its diffusivity. The mean scalar dissipation rate $\tilde{\chi}$ is an important parameter that links the mixing and combustion field. Analogous to turbulent kinetic energy dissipation ε in turbulent mixing, it describes the dissipation rate of scalar variance (fluctuations) in small scales by turbulent micromixing, influencing the mixing of reactants. Scalar dissipation mainly occurs in the finest scales. In literature, various expressions have been associated with χ , though they all describe mixing. The scalar dissipation can be related to the inverse of the diffusive time,

$$\chi \approx \tau_t, \quad (2.64)$$

and as a result can be related to the Damköhler number,

$$\chi \approx (\tau_c Da)^{-1}. \quad (2.65)$$

Figure 2.3 shows a sketch of the effect of χ on flame temperature in mixture fraction space. A low $\tilde{\chi}$ indicates conditions close to the fast chemistry limit, or equilibrium conditions. An increase in $\tilde{\chi}$ indicates a departure from the fast chemistry limit, as the diffusive time decreases and the reaction zone is strained, such that mass and heat transfer through the reaction zone is enhanced and chemical reactions do not occur at equilibrium conditions. The result is a decrease in temperature due to lower reaction rates. The modelling of the scalar dissipation rate is one of the main challenges in turbulent combustion modelling.

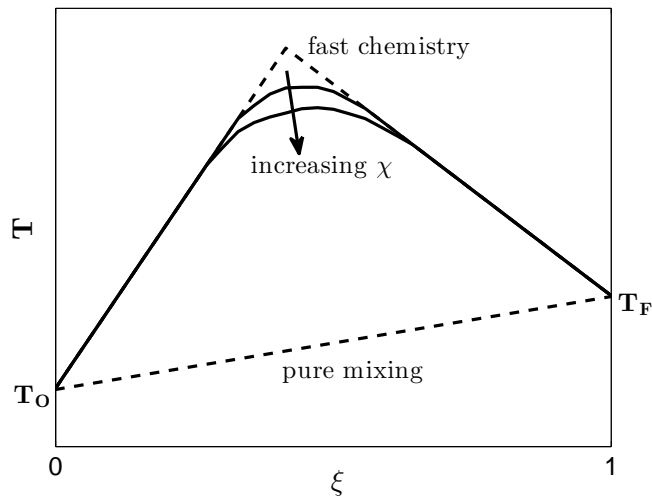


Figure 2.3: Sketch of the effect of scalar dissipation rate on temperature

2.3.4 Chemistry

The presence of chemical reactions in combustion modelling poses additional complexities not found in non-reacting flow modelling. For an irreversible, one-step global reaction consisting of a fuel (F), an oxidizer (O), and a product (P) defined by



where r is the mass of O per unit mass of F , the instantaneous fuel reaction rate is expressed by the Arrhenius law,

$$\dot{\omega}_F = -A\rho^2 T^n Y_F Y_O \exp\left(-\frac{E}{RT}\right), \quad (2.67)$$

where A is the pre-exponential factor, E the activation energy, and R the gas constant. The averaged fuel reaction rate, expanded using a Taylor's series [22], can be expressed by

$$\begin{aligned} \bar{\omega}_F = & -A\rho^2\tilde{T}^n\tilde{Y}_F\tilde{Y}_O\exp\left(-\frac{E}{R\tilde{T}}\right)\left[1+\frac{\widetilde{Y_F''Y_O''}}{\widetilde{Y_F}\tilde{Y}_O}+(P_1+Q_1)\left(\frac{\widetilde{Y_F''T''}}{\widetilde{Y_F}\tilde{T}}+\frac{\widetilde{Y_O''T''}}{\widetilde{Y_O}\tilde{T}}\right)\right. \\ & \left.+(P_2+Q_2+P_1Q_1)\left(\frac{\widetilde{Y_F''T''^2}}{\widetilde{Y_F}\tilde{T}^2}+\frac{\widetilde{Y_O''T''^2}}{\widetilde{Y_O}\tilde{T}^2}\right)+\dots\right], \end{aligned} \quad (2.68)$$

where $P_n = \sum_{k=1}^n (-1)^{n-k} \frac{(n-1)!}{(n-k)![(k-1)!]^2 k} \left(\frac{E}{R\tilde{T}}\right)^k$, and $Q_n = \frac{b(b+1)\dots(b+n-1)}{n!}$. The correlations such as $\widetilde{Y_k''Y''^n}$ require closure. As well, the highly non-linear nature of the terms in the series means that many of the higher order terms can not be excluded without large errors in the results. The handling of the mean reaction rate is one of the main modelling challenges in turbulent combustion.

2.4 Models for Turbulent Non-premixed Combustion

The wide use of turbulent non-premixed combustion in engineering applications has been a driving factor in the development and refinement of turbulence-chemistry models for these applications. The key to the development of combustion models is a balance between efficiency and accuracy, by using tools and assumptions that simplify calculations while maintaining a reasonable representation of the underlying physics. Brief introductions to a few well-known models are presented. The models and their major assumptions are summarized in Table 2.2.

2.4.1 Fast Chemistry Models

The underlying assumption in fast chemistry models is that the time scales of chemical reactions are infinitely smaller than the time scales of the mixing processes. The simplest fast chemistry model is the Burke-Schumann solution [23]. For an irreversible, one-step global reaction consisting of a fuel, an oxidizer, and a product defined by Eq. 2.66, mixing occurs between a stream containing F and another stream containing O , and reaction takes place where the mixture fraction is equal to the stoichiometric value, resulting in an infinitely-thin flame sheet. The mass fractions of F , O , and P are linear functions of ξ . Figure 2.4 shows the Burke-Schumann solution plotted as a function of ξ .

Table 2.2: Non-premixed combustion models and their major assumptions

Combustion model	Main assumptions
Flamelet modelling	<ul style="list-style-type: none"> • Flame structure made from ensemble of flamelets • Reaction zone smaller than Kolmogorov scales • Diffusion balances chemistry as in a 1-D counter-flow flame • Presumed PDF
CMC method	<ul style="list-style-type: none"> • Reduction in source term fluctuations when conditionally averaged • Diffusion captured by modelling micromixing • Presumed PDF
PDF method	<ul style="list-style-type: none"> • Diffusion captured by modelling micromixing • Closed chemical source term

The eddy dissipation model (EDM) [24] is an extension to a model initially developed for premixed combustion, the eddy breakup model (EBU) [25]. The models are devised under the assumption of high Reynolds number and Damkohler numbers. The mean reaction rate of the fuel is given by

$$\bar{\omega}_F = -C\bar{\rho}\frac{\varepsilon}{k}\sqrt{\widetilde{Y''^2}_F}, \quad (2.69)$$

for EBU, and

$$\bar{\rho\dot{\omega}}_F = \alpha\bar{\rho}\frac{\varepsilon}{k}\min\left(\widetilde{Y}_F, \frac{\widetilde{Y}_O}{r}, \beta\frac{\widetilde{Y}_P}{(1+r)}\right), \quad (2.70)$$

for EDM, where C , α , and β are model parameters that can be adjusted for different problems.

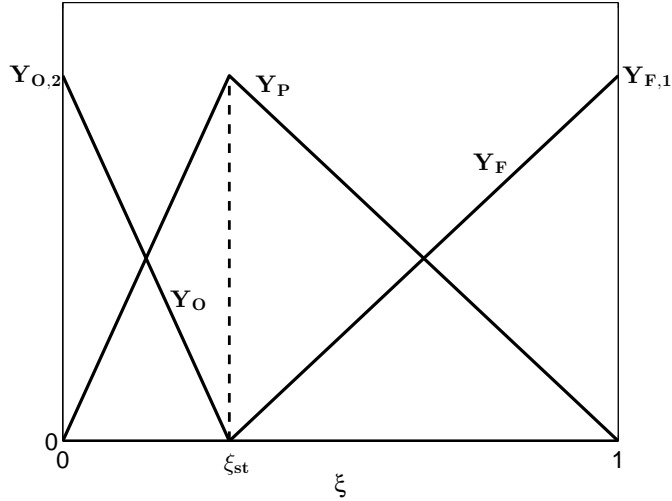


Figure 2.4: Burke-Schumann solution for fuel (F), oxidizer (O), and product (P) mass fractions against mixture fraction.

2.4.2 Laminar Flamelet Models

Laminar flamelet models [26] are finite rate chemistry models, based on the assumption that chemical reactions are fast enough so that they occur in thin regions with widths smaller than the Kolmogorov length scales, called flamelets, such that the regions are locally laminar. The laminar flamelet equation is given by

$$\frac{\partial Y_i}{\partial t} = \frac{\chi}{Le_i} \frac{\partial^2 Y_i}{\partial \xi^2} + \dot{\omega}_i. \quad (2.71)$$

The local conditions of the flamelet are characterized by ξ describing the micromixing, and χ describing the stretching of the flamelet which allows for finite rate chemistry effects. The solutions to Eq. 2.71, $Y_i(\xi, \chi)$, can be compiled for a range of χ values into a library of flamelets, which can then be referenced for local values of ξ and χ throughout the turbulent flame. The Favre mean species can be obtained by

$$\tilde{Y}_i(x_k, t) = \int_0^1 \int_0^\infty Y_i(\eta, \xi_s) \tilde{P}(\xi_s, \eta; x_k, t) d\xi_s d\eta, \quad (2.72)$$

where ξ_s is the sample space variable for ξ . The basis of the flamelet model on the assumption of thin reaction zones makes it less suitable for the larger chemical time scales, such as in autoignition or slow chemistry.

2.4.3 Conditional Moment Closure

Conditional moment closure method (CMC) for combustion modelling was first proposed independently by Bilger [27] and Klimenko [28], derived using different approaches. Bilger’s formulation involves decomposing the scalars into its conditional mean and fluctuation in their transport equations. Klimenko uses the joint PDF evolution equation of the reactive and conserved scalars. In both cases, the transport equations are conditionally averaged on a sample space variable η , taking on certain realizations of a scalar. In non-premixed combustion, the scalar is the mixture fraction ξ . The process of taking the conditional moment of the chemical source term considerably reduces its fluctuation about its mean value, such that the higher order terms in Eq. 2.68 can be neglected. Reasonable predictions of the source term is obtained by using first order closure which assumes that fluctuations in the conditional scalars are due to fluctuations in the mixture fraction [7]. Previous studies show that the first order CMC performs well for most turbulent non-premixed flames, except for flames close to extinction or ignition where significant fluctuations in temperature and species concentrations are present [29, 30, 31], so that disregarding the higher order terms in Eq. 2.68 is no longer credible. The focus of the present study is on CMC modelling, and further details on the model are presented in Section 4.

2.4.4 Transported PDF models

PDF transport models provide a general statistical description of turbulent combustion, applicable to both non-premixed and premixed regimes. Unlike in fast chemistry models, laminar flamelet model, and conditional moment closure, the form of the PDF is not presumed. Instead, the transport equations for the joint PDFs of velocity and species are solved. The transport equation for the joint PDF of velocity and reactive scalars $P(\mathbf{u}, \phi)$ is derived by Pope [32],

$$\begin{aligned} \frac{\partial \rho P}{\partial t} + \nabla \cdot (\rho \mathbf{u} P) + (\rho \mathbf{g} - \nabla p) \cdot \nabla_{\mathbf{u}} P + \frac{\partial}{\partial \psi_i} (\omega_i P) \\ = \nabla_{\mathbf{u}} \cdot (\langle -\nabla \cdot \tau + \nabla \rho' | \mathbf{v}, \psi \rangle P) - \frac{\partial}{\partial \psi_i} (\langle \nabla \cdot (\rho D \nabla \phi_i) | \mathbf{v}, \psi \rangle P). \end{aligned} \quad (2.73)$$

The chemical reaction rate is in closed form, thus no modelling is required for that term. Modelling is still required for the closure of viscous and molecular mixing terms, and the accuracy of results will depend of the submodels used. Due to the high dimensionality of the PDF transport equation, Monte Carlo techniques [33], for which memory requirements scale linearly with the dimensionality, are used over finite-volume methods,

where memory requirements scale exponentially with dimensionality. The stochastic nature of transported PDF methods requires substantial computational resources compared to deterministic methods such as flamelet modelling and CMC.

Chapter 3

Differential Diffusion in Turbulent Non-premixed Combustion

In this chapter, the topic of differential diffusion in turbulent non-premixed combustion is discussed. First, the theory behind differential diffusion (what it is and why it happens) is discussed. Various experimental investigations where differential diffusion effects had been observed and studies that used direct numerical simulation to investigate the phenomenon is presented. Lastly, a review of the previous strides in the inclusion of differential diffusion in turbulent reacting flow modelling is conducted.

3.1 Theory

Diffusion is a transport phenomena which involves the movement of mass or energy without the influence of bulk motion. The rate of diffusion between two types of molecules is dependent on the average inter-molecular distances, the average molecular speeds, and the sizes of the molecules. The dependency of the the rate of diffusion on the three factors can be quantified in the following relationship [34],

$$D \propto \frac{T^{0.7}}{\rho}, \quad (3.1)$$

where D is the mass diffusivity, a measure of the rate of diffusion between a pair of species, and a higher value of D indicates a higher diffusion rate between the pair. The temperature T offers a measure of the average kinetic energy of the molecules proportional to the square

of its velocity. An increase in the temperature results in an increase in the diffusion rate due to faster movement of the molecules. The density ρ of the mixture containing the molecules is a measure of the average distances between molecules. A lower density indicates larger inter-molecular distances, decreasing the chance of collision when diffusing towards each other and increasing the rate of diffusion. It can be noted that T and ρ in a gas are related by Eq. 2.16 such that a change in either T or ρ results in a change in the other variable unless p also varies at the same rate. In a constant pressure system, an increase in temperature results in a decrease in density, or vice versa, such that the increase in diffusivity is greater than in a system where the pressure is increased.

Larger molecules exhibit lower rates of diffusion while smaller molecules have higher rates of diffusion. Larger molecules have a higher chance of collision when attempting to diffuse across another type of molecule. In turbulent combustion modelling, it is common practice to assume equal diffusivity for all species, simplifying the modelling process. There are two main justifications made for the equal diffusivity assumption. First, many of the gaseous chemical species have similar diffusivities due to the similar sizes of three of the main elements involved in hydrocarbon combustion: carbon (C), nitrogen (N), and oxygen (O). Second, homogenization due to turbulent mixing tends to outweigh molecular diffusion effects due to the larger length and time scales of turbulence phenomena. However, there are cases where the weaknesses of the equal diffusivity assumption are seen in non-premixed flames.

The first justification is weakened when considering species with significantly different diffusivities diffusing to the other gaseous species, such as the high diffusivity of monoatomic hydrogen (H) and diatomic hydrogen molecules (H_2) due to their smaller molecular sizes, or the low diffusivity of large solid particulates such as soot. In turbulent flames, the differences in the diffusivities become prominent when high concentrations of species with significantly different diffusivities are involved, or where the differential diffusing species are of particular interest. High concentrations of H_2 or H are found in flames involving hydrogen fuels. In these flames, the light hydrogen molecules diffuse at a higher rate towards the reaction zone, thus increasing reaction rates. In heavily sooting flames, the low diffusivity of soot increases its residence time in the reaction zone after its formation, affecting the rate of enthalpy transport away from the reaction zone.

Experimental studies, which are discussed in Section 3.2, had shown that differential diffusion can be significant in turbulent nonpremixed flames near the nozzle. Various explanations were proposed to explain the presence of differential diffusion in these region, which were contrasted in the downstream regions where the effects disappeared.

In discussing the cause of differential diffusion effects in the context of turbulence mod-

elling, the prominence of the effects is related to the balance between the molecular diffusivity D and the turbulent diffusivity D_t . In high turbulence flows, D_t is many magnitudes larger than D , such that D is effectively zero and any change in D is equally negligible. However, if D_t is decreased and/or D is increased such that they are of comparable magnitudes, substantial differences between the diffusivities of the chemical species become evident. In turbulent non-premixed flames, the high temperatures and low densities result in higher molecular diffusivities compared to non-reacting flows due to the reasons noted earlier. However, the differences in temperature and densities between reacting and non-reacting cases result in an increase of one or two orders of magnitude in the diffusivities, which are still not comparable to the high turbulent diffusivities in turbulent diffusion flames. As such, an increase in molecular diffusivity alone is not enough to account for the noticeable effects of differential diffusion. More likely is the larger effect of decreasing turbulent diffusivity close to the nozzle. The turbulent diffusivity is proportional to the eddy viscosity, $D_t \propto \nu_t$, where the eddy viscosity is a function of the turbulent kinetic energy k and the inverse of its dissipation ε . Near the nozzle, the ratio of k to ε is lower, such that ν_t , and subsequently D_t , are lower.

A reason for the decrease in the ratio of k to ε can be given by examining the length scales of turbulence near the nozzle. ε is proportional to the inverse of the characteristic mixing length, $\varepsilon \propto l_m^{-1}$, where l_m is of the order of the mixing layer width between the fuel and oxidizer streams. When the mixing layer increases away from the nozzle, the ratio of k to ε increases, resulting in higher eddy viscosity. Pitsch [35] initially estimated that differential diffusion effects would be important when the characteristic mixing length is smaller than the Kolmogorov length scale η_k (the smallest scales of turbulence), but argued that the Kolmogorov eddies would have insufficient energy to contribute to transport within the layer and that a larger length scale, such as the Taylor scale λ_t might be a better criteria for the importance of differential diffusion effects. When the turbulence, or D_t , is very low, the mixing layer essentially becomes laminar sublayer, decreasing the local Reynolds number.

Another viewpoint is that the close to the nozzle, the structure of the mixing layer where the reaction zone is found, is laminar in structure. The laminar structure is the result of buoyancy effects and volumetric expansion in the reaction zone suppressing the formation of vortices.

The two viewpoints on the structure of the mixing layer are essentially the same in the physical sense (ie. the governing equations make no distinction between laminar and turbulence). However, the distinction is important in the context of computational fluid dynamics, since the modelling strategies of laminar and turbulent flows are very different, such as with the statistical description for turbulence. From the reasonings above, it is

evident that differential diffusion effects are quite possibly not only limited to laminar flames, but also in turbulent flames that satisfy the above conditions. It is also important to note that differential diffusion is not a different phenomenon from molecular diffusion, since the mechanism is the same. The concept of differential diffusion is only due to the common simplifications that are used in theoretical and numerical analyses of molecular diffusion.

The effects of differential diffusion on characteristic parameters reacting flows are of interest. One of these parameters is the Lewis number,

$$Le = \frac{\alpha}{D}, \quad (3.2)$$

describing the ratio of the thermal and mass diffusivities. Under equal species diffusivity assumption, the Lewis numbers for each species are equivalent. Often in theoretical and numerical analyses of reacting flows, the assumption is taken a step further by assuming that the species diffusivities are equal to the thermal diffusivity, such that the Lewis number has the value of 1, which greatly simplifies the analyses. The consideration of differentially diffusing species implies species Lewis numbers that differ depending on the diffusivity of the species. Examples of other characteristic parameters that are important in the study of differential diffusion are the Damköhler number (Eq. 2.57) and Schmidt number,

$$Sc = \frac{\text{viscous diffusion rate}}{\text{molecular diffusion rate}} = \frac{\nu}{D}. \quad (3.3)$$

3.2 Differential Diffusion in Experimental Studies

Various experimental studies of laboratory flames revealed trends that advocated the significance of differential diffusion. In particular, flames involving hydrogen fuels had shown that differential diffusion could explain observations of higher temperatures and radical production (such as OH and NO). This section reviews experimental studies in literature and presents their major findings in relation to differential diffusion.

Drake *et al.* [36] observed evidence of differential diffusion effects on H₂, H₂O, and N₂ concentrations in fuel rich regions of a mildly turbulent flame of Reynolds number 1500 and 2200 H₂ in air jet flame in laser-Raman spectroscopy measurements. Correlation plots of concentration versus temperature for H₂ and N₂ departed from the equal diffusivity, adiabatic, and equilibrium calculations. Temperature measurements were found to be higher than the equilibrium solution. In the fuel rich regions, N₂ and H₂O concentrations measurements were found to be higher than predicted and H₂ concentrations were lower.

Predicted departures were not consistent with the measured departures. Drake *et al.* [36] considered the effects of differential diffusion as the explanation for their observations of super-equilibrium temperatures. Drake *et al.* proposed several possible assumptions in the equilibrium calculations that might have been the source of the deviations: neglect of radiative heat loss, finite rate chemistry, buoyancy, and differential diffusion. Calculations of maximum radiative heat loss showed that the resulting changes in temperature and concentrations were much smaller than the deviations observed. The calculated time scales that brought the theoretical and measurements into agreement by considering non-equilibrium effects were not compatible with the shorter time scales in hydrogen combustion. Buoyancy effects were also not able to account for the magnitude of deviations observed. Drake *et al.* concluded that the most plausible explanation for the observations were due to differential diffusion effects of H₂ from the rich regions. Drake *et al.* [37] extended the investigation by including data for $Re = 8500$ flame and deviations were still observed close to the nozzle (less than 50 nozzle diameters), though suggested that finite-rate chemistry may also play a role.

A different set of experiments with H₂-air non-premixed flame were conducted by Barlow and Carter [38], with flames of $Re = 10,000$ and different levels of helium dilution in the fuel. In addition to Raman scattering measurements for major species concentrations (H₂, O₂, H₂O, and N₂), Rayleigh scattering techniques were used to also obtain concentrations for OH and NO. Even at this Reynolds number, differential diffusion effects were observed close to the nozzle. Super-equilibrium concentrations were observed for OH, which were found to be close to calculations for a strained laminar flame which considers differential diffusion. Interestingly, the helium dilution of the flame, which minimized the effects of radiation, resulted in trends (super-equilibrium temperature and OH concentrations) that were qualitatively the same as the undiluted case, and thereby strengthened the conjecture of the significance of differential diffusion. Temperature and O concentration in turn affected the production rate of NO [39].

Super-equilibrium temperatures and increased NO production rates near the nozzle were also observed by Meier *et al.* in the Raman/LIF measurements of H₂-air non-premixed flame with various levels of dilution by N₂, at different Reynolds numbers (6200 and 8800) [40], as well as with different nozzle diameters (at $Re = 10,000$) and with lift-off conditions (separation of flame from the nozzle) [41]. Like the helium diluted flames studied by Barlow and Carter, the nitrogen dilution reduced radiation heat losses, which reduced uncertainty caused by these losses. To further investigate the influence of differential diffusion, Meier *et al.* examined the correlation of the NO measurements to two different mixture fraction definitions, one based on the elemental mass fraction of H and another on the elemental O

mass fraction. The elemental mixture fractions were defined by the expression

$$\xi_{\alpha} = \frac{Y_{\alpha} - Y_{\alpha,o}}{Y_{\alpha,f} - Y_{\alpha,o}}, \quad (3.4)$$

where the subscript α indicates the element, and f and o indicates fuel and oxidizer streams, respectively. It was found that the peak NO shifted to the rich side of the stoichiometric mixture fraction for the H element mixture fraction and to the lean side for the O element mixture fraction. The defined mixture fraction did not conserve the stoichiometric value under the presence of differential diffusion, since the elemental mixture fractions themselves diffused differently. In other words, the stoichiometric value of mixture fraction shifted to the rich side of the hydrogen element mixture fraction due to a higher rate of diffusion of hydrogen element, and by conservation, the opposite effect occurred for the oxygen element mixture fraction. Meier *et al.* found that differential diffusion effects became more pronounced as the exit velocity was decreased, while a constant Reynolds number was kept by increasing the nozzle diameter. As well, a slightly stronger influence of differential was found when the flame was lifted.

Differential diffusion effects were also observed in CO₂ diluted hydrogen flames studied by Masri *et al.* [42] and Smith *et al.* [43]. At the high temperature of the flame, CO₂ was not completely inert, and reacted to produce CO. Masri *et al.* investigated high Reynolds numbers (15000 to 30000) flames with blowoff, and found that although differential diffusion effects on major species were not too important, the effects on minor radicals like H, which were important in controlling extinction, were significant. Smith *et al.* explored a wide range of reacting jets of Reynolds numbers 1,000 to 30,000, and found differential diffusion effects to be present throughout the range of Reynolds numbers by examining the elemental mixture fractions of H and C defined by Eq. 3.4. Significant differential diffusion effects occurred on the fuel rich side of the flame, and caused a greater net flux of hydrogen toward reaction zone from diffusion between hydrogen and H₂O compared to the diffusion between CO₂ and H₂O. Smith *et al.* also noted, by comparing with nonreacting measurements, that the presence of chemical reactions accentuated the differential diffusion of H₂ by the existence of a sink for H₂ (and source for H₂O) which caused steeper concentrations gradients. The same trends were observed by Bergmann [44] in a methane (CH₄)/H₂/N₂ flame, who also found deviations in the elemental mixture fractions of H and C from equal diffusivity results at five nozzle diameters from the jet exit.

3.3 Differential Diffusion in DNS Studies

Though the use of DNS to simulate practical combustion processes is unfeasible, DNS can nonetheless be used to assess simplified, and often theoretical cases. DNS studies can provide information that are otherwise difficult to quantify in experiment measurements. This section provides a brief outline of a few DNS studies that pertain to differential diffusion in non-premixed reacting flows.

Katta *et al.* [45] simulated the surface of a low-speed hydrogen-air nonpremixed flame to analyze the effects of differential diffusion on the flame structure, using detailed chemistry to capture finite rate effects. It was observed that the rates of mass diffusion were higher than heat diffusion on the fuel-rich side of the reaction zone due to high H_2 concentrations, while mass and heat diffusion rates were similar on the lean side. As such, differential diffusion effects were found to be important in predicting flame temperature oscillations.

Jaberi *et al.* [46] conducted a DNS study on homogeneous, turbulent box flow under reacting nonpremixed conditions. The results indicated the importance of the Damköhler number and Schmidt number in the characterization of reacting flows with differential diffusion. As reactions rates were increased, the influence of differential diffusion also increased. Scalar variances were also found to have increased for reacting scalars with higher diffusivities, while variances were decreased for lower diffusivities. Overall, changes in the scalar statistics (ie. the PDF) due to differential diffusion were observed in the presence of chemical reactions.

Nilsen and Kosaly [47] examined differential diffusion effects on fields of isotropic, decaying turbulence of reacting scalars. It was also demonstrated that differential diffusion effects increased with increasing Damköhler number. More significantly, Nilsen and Kosaly used the DNS results to assess whether flamelet and CMC methods could accurately account for differential diffusion effects. It was found that neglecting conditional fluctuations in the presence of differential diffusion misled the Reynolds number dependence of the scalar concentrations and reaction rates, due to not accounting for small scale effects at which differential diffusion occurred. In other words, careful consideration had to be taken in the modelling of conditional dissipation and diffusion rates of the conserved scalar (mixture fraction) .

Hilbert and Thévenin [48] performed two dimensional DNS of diluted turbulent hydrogen non-premixed flames to investigate the influence of differential diffusion on temperatures. Two cases were compared, where the difference was in the evaluation of the diffusion velocities in the species transport equations, where one case assumed all species Lewis numbers are unity and another case where differences in diffusivities were considered.

Analysis of equilibrium temperatures showed that the fast chemistry limit was dependent on local conditions. Hibert and Thévenin pointed out that the variation in equilibrium profiles was consistent if the diffusion coefficient of the mixture fraction differed from the thermal diffusion coefficient.

3.4 Progress in Differential Diffusion Modelling

Due to the experimental and DNS evidence, as described in Section 3.2 and 3.3, there has been interest in incorporating differential diffusion effects in existing turbulence-combustion models. This section reviews different strategies that had been used, summarizing their philosophies and results, and a discussion into their advantages and disadvantages. Extensive details on the theory and model development involved will not be covered.

One of the first attempts, to the author's best knowledge, at incorporating differential diffusion effects into turbulent non-premixed flame modelling was the perturbation analysis of Bilger [49]. Bilger introduced the effects of differential diffusion by modelling them as perturbations about the equal diffusivity, adiabatic, equilibrium solution (the fast chemistry solution described in Section 2.4.1 with linear elemental mass fractions and enthalpy). Equations for the perturbations were derived. The hydrogen-air diffusion flame of Drake *et al.* [36] was analyzed and found reasonable agreement with experimental measurements for the H_2 . The weaknesses of the method were associated with the assumption of fast chemistry. The inability to predict finite chemistry and strained flames limited its uses. This was especially important for the prediction of pollutants such as NO_x and soot.

Pitsch and Peters [50] developed an Unsteady Laminar Flamelet Model which included the effects of differential diffusion. The main assumption in this model was, as described in Section 2.4.2, that the flame could be described as an ensemble of locally laminar flames. Pitsch [35] applied the model to a turbulent $CH_4/H_2/N_2$ -air diffusion flame [44]. Good agreement with experimental measurements was obtained in the region close to nozzle, but in the downstream regions, agreement was only achieved by reverting to unity Lewis numbers at the end of the jet potential core. Some effect of the differential diffusion on species and temperature predictions remained even at downstream locations where unity Lewis numbers were used, showing a history effect in the flame. Pitsch postulated that the transition from non-equal to unity Lewis number was due to the existence of a fully laminar flow very close to the nozzle before transitioning to turbulence. However, concerns arising from the arbitrary switch in the Lewis number are expressed here. The point of transition from laminar to turbulence, assumed to have occurred 10 nozzle diameters downstream

in the flame studied by Pitsch [35], is not clear-cut. Transition is also difficult to predict using RANS models such as $k-\varepsilon$.

For transported PDF approaches to modelling combustion, the main modelling challenge is the closure of molecular mixing, as described in Section 2.4.4. Most mixing models are proposed under the assumption of equal diffusivity. Efforts to include differential diffusion in transported PDF methods had been made by [51, 52, 53]. Chen and Chang proposed a function to replace the linear relationships in the existing mixing models. The function was dependent on the Peclet number defined as,

$$Pe = \frac{\text{advective transport rate}}{\text{diffusive transport rate}} = \frac{LU}{D}, \quad (3.5)$$

where L is the characteristic length, U is the characteristic velocity, and D is the diffusion coefficient. As $Pe \rightarrow \infty$, such that advective transport dominated over diffusive transport, the mixing model reverted to the equal diffusivity approximations. Chen and Chang applied their method to H_2/CO_2 flames [43] and H_2/N_2 flames [41]. For the H_2/CO_2 flames, less agreement with the experimental data was found. For the H_2/N_2 flames, better agreement was found at downstream locations than in the near field regions. Similar to Pitsch [35], Chen and Chang attributed the discrepancy in near-field region to the laminarization of the flame, where traditional turbulence modelling was unable to perform properly. Aside from the modelling difficulties, transported PDF approaches remain on the upper end of combustion modelling approaches in terms of computational costs. Likewise, Fox [52] developed a different mixing model which considered differential diffusion and validated it against DNS data for scalars in isotropic turbulence. The model of Fox was further extended in [54] by validating it against a simple one-step chemistry DNS case and found good agreement if the conditional scalar dissipation rate could be accurately predicted. McDermott and Pope [53] proposed modifications to the Filtered Density Function (FDF) methods, the LES (Section 2.2.3) equivalent for the transported PDF. In their proposed model, the assumption of negligible variance molecular transport was made, limiting its use to high Reynold number regimes. Numerical studies involving pure mixing test cases had been performed to evaluate the accuracy and computational costs of the model [53, 55], but the model had not been applied to experimental flames, likely due to the high collective costs of performing both LES and PDF methods.

Maragkos *et al.* [56] recently presented a methodology to include differential diffusion in the solution of the species transport equation in physical space which had been projected onto a subspace of conserved scalars (no chemical source term). The chemical source term in the species transport equation was removed by taking certain linear combinations of the equations, and resulted in the separation of the diffusion term into a component expressing

the diffusion of the conserved scalars and another expressing feedback from the combustion model. Maragkos *et al.* [56] applied the method to laminar, axi-symmetric H_2/N_2 -air diffusion flames [57]. However, the formulation had not been validated for turbulent flame calculations, though it was suggested that the method can be extended to turbulent flames [56].

Kerstein [58] investigated differential diffusion using the Linear-Eddy Model (LEM) and found that differential diffusion could be considered by assigning the appropriate molecular diffusivity for each species, though the resolution which captured all relevant lengthscales in this process was needed. The model was applied to the prediction of non-reacting hydrogen-Freon jets and good agreement was found. A Multiple Mapping Conditioning (MMC) model, an extension of the CMC method combined with the transported PDF approach for differential diffusion had also been derived and tested against DNS for homogeneous, isotropic and two scalar mixing [59]. Further comparisons are needed to fully evaluate its performance to general turbulent combustion problems including differential diffusion.

Kronenburg and Bilger [60] analyzed the modelling of differential diffusion in non-reacting flows following the CMC method of Bilger [27] derived by the decomposition of the scalar into a mean and its fluctuations, and proposed models for unclosed terms that become significant when differential diffusion was considered. The model was used to investigate reacting flows by application to one turbulent hydrogen-air flame [61] with special focus on NOx predictions in the near-field of the flame, two methane-air flames [62] and three ethylene-air flames [63] for soot formation. This model required the solution of an additional transport equation for each differentially diffusing species and enthalpy in order to model a term drives the profiles towards equal diffusivity. An approximation was provided by fitting some DNS data obtained for mixing between two non-reacting scalars in homogeneous isotropic decaying turbulence [60]. For the study involving the hydrogen-air flame, the model was applied to a RANS simulation of the turbulent hydrogen jet flame of Barlow *et al.* [38]. It was reported that the differential diffusion effects of H_2 on species transport had no notable effect on temperature and OH predictions. Accounting for the effects of H_2 differential diffusivity on enthalpy resulted in improved temperature predictions around stoichiometric, as well as an increase of almost 100% in NO levels. Inclusion of H differential diffusivity resulted in further improvement in temperature predictions, but NO predictions were 20% less than when only H_2 is considered. The results reported showed that although NO mass fractions increased near the nozzle where significant underprediction due to the effects of differential diffusion occurred [64], the predictions remained noticeably underpredicted. Yunardi *et al.* [63], in their investigation of the effects of differential diffusion on soot generation in turbulent nonpremixed ethylene flames in RANS, found better agreement with experimental data when differential diffusion

of soot was considered.

The CMC approach used by Kronenburg and Bilger [60] was also studied in LES context by Navarro-Martinez *et al.* [65]. A similar formulation was implemented in LES-CMC for soot with tabulated chemistry [65] with reasonable predictions for the soot volume fraction. The modelled term in [66, 62] requiring additional transport equations, which affected small scale differential diffusion transport, was assumed to be small in LES compared to large scale transport and was neglected [65].

More recently, Hewson *et al.* [6] proposed a different approach to derive a formulation for CMC which included the effects of differential diffusion in the species transport equation, but without the need to solve additional transport equations for the differentially diffusing species. The formulation was investigated in an *a priori* sense for an ethene pool fire using mixture fraction ξ and soot mass fraction Y_s evolution predicted from the one-dimensional turbulence model to evaluate the significance of differential diffusion terms in the CMC equation [67]. It was reported that a residual term related to the term associated with differential diffusion in the CMC formulation of the soot transport equation was found to be significant. Additional investigations were carried out by Hewson *et al.* [68] and Lignell *et al.* [69] in the context of ethylene jet flame configuration in which direct numerical simulation results were used to analyse the CMC formulation. Lignell *et al.* found that for gaseous species, the model for the differential diffusion term predicts reasonably well, while an overshoot was noted for the terms associated with the product of scalar and its dissipation rate, and the cross-dissipation of the scalar and the mixture fraction.

3.5 Summary

As examined in the preceding sections, differential diffusion effects play a perceptible role in many combustion cases. A discussion of the theory behind differential diffusion in Section 3.1 provided insight into its mechanisms. Experimental and DNS investigations of different flames presented evidence in a wide range of hydrogen fuel based flames with different conditions such as Reynolds numbers. A review of the previous efforts to model differential diffusion showed the advantages and shortcomings of various numerical methods in accounting for differential diffusion effects. Of particular interest here are the CMC models of Kronenburg and Bilger [61], and Hewson *et al.* [6]. The CMC model of Kronenburg and Bilger required the solution of an additional transport equation for each differential diffusing species. In contrast, the formulation used by Hewson *et al.* did not need additional transport equations to be solved. The model was studied in an *a priori* sense for ethylene flames, but was never applied to a hydrogen flame or coupled to a CFD

simulation of a flame. The following chapter provides details on the CMC species transport formulation used by Hewson *et al.*, and introduces a similar formulation for enthalpy transport. The model is applied to a coupled CFD investigation of the hydrogen-air flame experimentally studied by Barlow and Carter [38].

Chapter 4

Conditional Moment Closure

A brief overview of the CMC method was presented in Section 2.4.3. In this chapter, the derivations of the CMC species and enthalpy transport equations, with the effects of differential diffusion, are explained. A discussion of the closure submodels for unclosed terms in the CMC formulations is given. Finally, the CMC equations with the closure models included are presented, to prelude the discretisation of the equations in Chapter 5. The following derivations of the CMC equations follow Klimenko's approach using the joint PDF equation [28].

4.1 Probability Density Function Transport Equation

The PDF and some of its properties were introduced in Section 2.1.3, and in this section, the concept of the PDF is extended to the transport phenomena. The transport of a random variable can be represented by the transport of its PDF. The derivation of a PDF transport equation starts from defining a useful function, the fine-grained PDF ψ , associated with the PDF by the following relationship,

$$P(\mathcal{Z}) = \langle \psi \rangle, \quad (4.1)$$

where $\langle \cdot \rangle$ denotes an ensemble average of the quantity inside the bracket. In other words, ψ is the one-time PDF of stochastic variable \mathcal{Y} over the sample space \mathcal{Z} . The time derivative of ψ is given by,

$$\frac{\partial \psi}{\partial t} = -\frac{\partial}{\partial \mathcal{Z}_i} \left(\psi \frac{\partial \mathcal{Y}_i}{\partial t} \right), \quad (4.2)$$

while the gradient vector of ψ is given by,

$$\nabla\psi = -\frac{\partial}{\partial\mathbf{Z}_i}(\psi\nabla\mathcal{Y}_i), \quad (4.3)$$

The identities given by Eqs. 4.2 and 4.3 are obtained by mathematical transformation from the Dirac delta function representation of ψ . The details of the delta representation and the procedures for obtaining Eqs. 4.2 and 4.3 are omitted here, but can be found in [7]. Next, a scalar ϕ_i is defined as a stochastic variable \mathcal{Y} , which is an element of the set $\phi = \{\phi_1, \phi_2, \dots, \phi_n\}$, where each element satisfies the following scalar transport equation,

$$\rho\frac{\partial\phi_i}{\partial t} + \rho\mathbf{u} \cdot \nabla\phi_i = \nabla \cdot (\rho D_i \nabla\phi_i) + \rho W_i, \quad (4.4)$$

where D_i is the diffusion coefficient of ϕ_i , and W_i is the source term of ϕ_i . Equation 4.4 is similar in form to the species transport equation assuming Fickian diffusion, Eq. 2.8.

The transport equation for the fine-grained PDF is obtained by combining Eqs. 4.2 and 4.4, and with the use of Eq. 4.3 and the continuity equation (Eq. 2.1), this results in the divergent form of the fine-grained PDF transport equation,

$$\frac{\partial\rho\psi}{\partial t} + \nabla \cdot (\rho\mathbf{u}\psi) = -\frac{\partial}{\partial\mathbf{Z}_i}(\psi\nabla \cdot (\rho D_i \nabla\phi_i)) - \frac{\partial}{\partial\mathbf{Z}_i}(\rho\psi W_i). \quad (4.5)$$

Equation 4.5 describes the evolution of $\psi(\phi)$, the fine-grained joint PDF of the set of scalars ϕ . The transport equation for the joint PDF, $P(\phi)$, can easily be obtained by averaging Eq. 4.5, and the resulting equation is

$$\begin{aligned} \frac{\partial\langle\rho|\phi=\mathbf{Z}\rangle P}{\partial t} + \nabla \cdot (\langle\rho\mathbf{u}|\phi=\mathbf{Z}\rangle P) &= -\frac{\partial}{\partial\mathbf{Z}_i}(\langle\nabla \cdot (\rho D_i \nabla\phi_i)|\phi=\mathbf{Z}\rangle P) \\ &- \frac{\partial}{\partial\mathbf{Z}_i}(\langle\rho W_i|\phi=\mathbf{Z}\rangle P). \end{aligned} \quad (4.6)$$

There are two methods in deriving the CMC equations, one involving the use of Eq. 4.5, while the other uses 4.6. Both methods are explored in the next sections; the CMC species transport equation is derived using Eq. 4.6 as the starting point, while the CMC enthalpy transport equation is derived using Eq. 4.5. However, both approaches are applicable to the derivation of either equations.

4.2 Equal Diffusivity CMC Formulation

The CMC equations in the case of equal diffusivity assumption are first presented in this section, without rigorous details on the derivation, for the interest of comparison with the

more general non-equal diffusivity CMC equations to be derived in Sections 4.3 and 4.4. In the case of unity Lewis number, the unclosed CMC equation for species i derived using Klimenko's joint PDF method, is given by [7],

$$\begin{aligned} \frac{\partial \langle \rho Y_i | \xi = \eta \rangle P_\eta}{\partial t} + \nabla \cdot (\langle \rho Y_i \mathbf{u} | \xi = \eta \rangle P_\eta) &= -\frac{\partial^2}{\partial \eta^2} (\langle \rho D_\xi (\nabla \xi)^2 Y_i | \xi = \eta \rangle P_\eta) \\ &+ \frac{\partial}{\partial \eta} (\langle 2\rho D_\xi (\nabla Y_i \nabla \xi) | \xi = \eta \rangle P_\eta) + \langle \rho \dot{\omega}_i | \xi = \eta \rangle P_\eta, \end{aligned} \quad (4.7)$$

where the notation $P_\eta = P(\eta)$ is used for convenience. The terms on the LHS of Eq. 4.7 represent the temporal rate of change and advection, while the first two terms on the RHS describe diffusion across the conserved scalar space η and the last term is the source term. It should be noted that Eq. 4.7 is derived under a high Reynolds number assumption, so that terms describing the diffusion of the conditional quantities in physical space (x, y, z) are omitted. The high Reynolds number assumption is not made in the derivation of the non-equal diffusivity CMC equations; an explanation of assumption is not presented here, but interested readers are referred to [7].

Various quantities in Eq. 4.7 require modelling for closure. The primary closure hypothesis [28], which is discussed in Section 4.5.1, attempts to model the first two terms on the RHS of Eq. 4.7, the diffusion terms. After applying the primary closure hypothesis, Eq. 4.7 can be written as

$$\frac{\partial \rho_\eta Q_i P_\eta}{\partial t} + \nabla \cdot (\langle \rho Y_i \mathbf{u} | \xi = \eta \rangle P_\eta) = \frac{1}{2} \rho_\eta \chi_\eta P_\eta \frac{\partial^2 Q_i}{\partial \eta^2} - \frac{1}{2} \frac{\partial^2 \rho_\eta \chi_\eta P_\eta}{\partial \eta^2} Q_i + \rho_\eta \dot{\omega}_{\eta,i} P_\eta, \quad (4.8)$$

where the notation ρ_η is used for the conditional density $\langle \rho | \xi = \eta \rangle$. For convenience, the density-weighted (Favre) conditional averaged mass fraction Q_i and Favre conditional averaged reaction rate $\dot{\omega}_{\eta,i}$ in Eq. 4.8 are defined as,

$$Q_i = \frac{\langle \rho Y_i | \xi = \eta \rangle}{\langle \rho | \xi = \eta \rangle}, \quad (4.9)$$

and

$$\dot{\omega}_{\eta,i} = \frac{\langle \rho \dot{\omega}_i | \xi = \eta \rangle}{\langle \rho | \xi = \eta \rangle}. \quad (4.10)$$

Additionally, the conditional Favre averaged scalar dissipation rate χ_η in Eq. 4.8 is defined as,

$$\chi_\eta = \frac{\langle 2\rho D_\xi (\nabla \xi)^2 | \xi = \eta \rangle}{\langle \rho | \xi = \eta \rangle}. \quad (4.11)$$

The closure of the conditional velocity term and the conditional source term are discussed in Section 4.5.

Similar to Eq. 4.7, the unclosed form of the CMC enthalpy transport equation can be obtained using the joint PDF method, and under high Reynolds number assumption, is

$$\begin{aligned} \frac{\partial \langle \rho h | \xi = \eta \rangle P_\eta}{\partial t} + \nabla \cdot (\langle \rho h \mathbf{u} | \xi = \eta \rangle P_\eta) &= -\frac{\partial^2}{\partial \eta^2} (\langle \rho \alpha (\nabla \xi)^2 h | \xi = \eta \rangle P_\eta) \\ &+ \frac{\partial}{\partial \eta} (\langle 2\rho \alpha (\nabla h \nabla \xi) | \xi = \eta \rangle P_\eta) + \langle \rho s_h | \xi = \eta \rangle P_\eta, \end{aligned} \quad (4.12)$$

Once again, the first two terms on the RHS of Eq. 4.12 are modelled using the primary closure hypothesis of Kllimenko, resulting in

$$\frac{\partial \rho_\eta Q_h P_\eta}{\partial t} + \nabla \cdot (\langle \rho h \mathbf{u} | \xi = \eta \rangle P_\eta) = \frac{1}{2} \rho_\eta \chi_\eta P_\eta \frac{\partial^2 Q_h}{\partial \eta^2} - \frac{1}{2} \frac{\partial^2 \rho_\eta \chi_\eta P_\eta}{\partial \eta^2} Q_h + \rho_\eta s_{\eta,h} P_\eta, \quad (4.13)$$

where $Q_h = \langle \rho h | \xi = \eta \rangle / \langle \rho | \xi = \eta \rangle$ is the Favre conditional averaged enthalpy and $s_{\eta,h} = \langle \rho s_h | \xi = \eta \rangle / \langle \rho | \xi = \eta \rangle$ is the Favre conditional averaged source term including radiation losses. In Eq. 4.13, it is assumed that the thermal diffusivity α is equal to the mixture fraction diffusivity D_ξ . A comprehensive derivation of Eqs. 4.8 and 4.13 for the case of equally diffusive species can be found in [7].

The transport equation for the mixture fraction PDF, $P(\eta)$, should be satisfied jointly with Eqs. 4.8 and 4.13. The $P(\eta)$ transport equation can be obtained from Eq. 4.6 for a single scalar variable, and with the use of some identities involving the gradient operation [7], results in the form

$$\frac{\partial \rho_\eta P_\eta}{\partial t} + \nabla \cdot (\rho_\eta \mathbf{u}_\eta P_\eta) = -\frac{1}{2} \frac{\partial^2 \rho_\eta \chi_\eta P_\eta}{\partial \eta^2}, \quad (4.14)$$

where $\mathbf{u}_\eta = \langle \rho \mathbf{u} | \xi = \eta \rangle / \langle \rho | \xi = \eta \rangle$ is the Favre conditional averaged velocity vector. The most common form of the CMC equations can be found by subtracting Eq. 4.14 multiplied by Q_i from Eq. 4.8, giving

$$\rho_\eta P_\eta \frac{\partial Q_i}{\partial t} + \nabla \cdot (\langle \rho Y_i \mathbf{u} | \xi = \eta \rangle P_\eta) - \nabla \cdot (\rho_\eta \mathbf{u}_\eta P_\eta) Q_i = \frac{1}{2} \rho_\eta \chi_\eta P_\eta \frac{\partial^2 Q_i}{\partial \eta^2} + \rho_\eta \dot{\omega}_{\eta,i} P_\eta, \quad (4.15)$$

and by subtracting Eq. 4.14 multiplied by Q_h from Eq. 4.13,

$$\rho_\eta P_\eta \frac{\partial Q_h}{\partial t} + \nabla \cdot (\langle \rho h \mathbf{u} | \xi = \eta \rangle P_\eta) - \nabla \cdot (\rho_\eta \mathbf{u}_\eta P_\eta) Q_h = \frac{1}{2} \rho_\eta \chi_\eta P_\eta \frac{\partial^2 Q_h}{\partial \eta^2} + \rho_\eta s_{\eta,h} P_\eta. \quad (4.16)$$

Equations 4.15 and 4.16 are in conservative form, suitable for discretisation using the finite volume approach, while Eqs. 4.8 and 4.13 are in non-conservative form, suitable for the finite difference discretisation approach. In the present study, the transport equations in conservative form are used, where the finite volume approach is employed in Section 5.2.

4.3 CMC Formulation of Species Equation Including Differential Diffusion

The CMC formulation for species transport used in the present investigation is derived using a similar approach to Klimenko's joint PDF method for the equal species diffusivity. The difference is that the assumption of equal diffusivity is not made, resulting in different diffusion terms in the CMC equation. This section provides a review of the derivation outlined by Hewson *et al.* [6]. Additional details of the procedure can be found in the more rigorous derivation in Appendix A.

The derivation begins from the joint PDF transport equation, Eq. 4.6, for two scalar stochastic variables, ϕ_1 and ϕ_2 , expressed as

$$\begin{aligned}
& \frac{\partial \langle \rho | \phi_1 = Z_1, \phi_2 = Z_2 \rangle P_{Z_1, Z_2}}{\partial t} + \nabla \cdot (\langle \rho \mathbf{u} | \phi_1 = Z_1, \phi_2 = Z_2 \rangle P_{Z_1, Z_2}) \\
& = - \frac{\partial}{\partial Z_1} (\langle \nabla \cdot (\rho D_1 \nabla \phi_1) | \phi_1 = Z_1, \phi_2 = Z_2 \rangle P_{Z_1, Z_2}) \\
& \quad - \frac{\partial}{\partial Z_2} (\langle \nabla \cdot (\rho D_2 \nabla \phi_2) | \phi_1 = Z_1, \phi_2 = Z_2 \rangle P_{Z_1, Z_2}) \quad (4.17) \\
& \quad - \frac{\partial}{\partial Z_1} (\langle \rho W_1 | \phi_1 = Z_1, \phi_2 = Z_2 \rangle P_{Z_1, Z_2}) \\
& \quad - \frac{\partial}{\partial Z_2} (\langle \rho W_2 | \phi_1 = Z_1, \phi_2 = Z_2 \rangle P_{Z_1, Z_2}).
\end{aligned}$$

An equation for the joint PDF, $P(Z_Y, \eta)$, of the mass fraction Y_i of species i and the mixture fraction ξ , is obtained from Eq. 4.17 by setting $\phi_1 = Y_i$ and $\phi_2 = \xi$. Consequently, the sample space variables Z_1 and Z_2 become the respective sample space variables Z_Y and η . The diffusion coefficients are $D_1 = D_i$ and $D_2 = D_\xi$, while the source term W_1 is the species production rate $\dot{\omega}_i$. Following the assumption of the existence of a conserved mixture fraction definition (Section 2.3.2), the source term W_2 becomes zero. The conserved mixture fraction assumption is consistent with previous modelling studies

involving differential diffusion [50, 67]. The resulting equation is

$$\begin{aligned}
& \frac{\partial \langle \rho | Y_i = Z_Y, \xi = \eta \rangle P_{Z_Y, \eta}}{\partial t} + \nabla \cdot (\langle \rho \mathbf{u} | Y_i = Z_Y, \xi = \eta \rangle P_{Z_Y, \eta}) \\
& = -\frac{\partial}{\partial Z_Y} (\langle \nabla \cdot (\rho D_i \nabla Y_i) | Y_i = Z_Y, \xi = \eta \rangle P_{Z_Y, \eta}) \\
& \quad - \frac{\partial}{\partial \eta} (\langle \nabla \cdot (\rho D_\xi \nabla \xi) | Y_i = Z_Y, \xi = \eta \rangle P_{Z_Y, \eta}) \\
& \quad - \frac{\partial}{\partial Z_Y} (\langle \rho \dot{\omega}_i | Y_i = Z_Y, \xi = \eta \rangle P_{Z_Y, \eta}).
\end{aligned} \tag{4.18}$$

Conducting a series of mathematical manipulation (details in Appendix A) based on the gradient operation of Eq. 4.3 and the relationship $\langle \circ | \psi \rangle = \langle \circ | \mathbf{Y} = \mathbf{Z} \rangle P(\mathbf{Z})$ where \circ is a general quantity [7], Eq. 4.18 can be expressed as

$$\begin{aligned}
& \frac{\partial \langle \rho | Y_i = Z_Y, \xi = \eta \rangle P_{Z_Y, \eta}}{\partial t} + \nabla \cdot (\langle \rho \mathbf{u} | Y_i = Z_Y, \xi = \eta \rangle P_{Z_Y, \eta}) \\
& = -\frac{\partial}{\partial \eta} (\langle \nabla \cdot (\rho (D_\xi - D_i) \nabla \xi) | Y_i = Z_Y, \xi = \eta \rangle P_{Z_Y, \eta}) \\
& \quad + \nabla^2 (\langle \rho D_i | Y_i = Z_Y, \xi = \eta \rangle P_{Z_Y, \eta}) \\
& \quad - \nabla \cdot (\langle \nabla (\rho D_i) | Y_i = Z_Y, \xi = \eta \rangle P_{Z_Y, \eta}) \\
& \quad - \frac{\partial^2}{\partial Z_Y^2} (\langle \rho D_i (\nabla Y_i)^2 | Y_i = Z_Y, \xi = \eta \rangle P_{Z_Y, \eta}) \\
& \quad - \frac{\partial^2}{\partial \eta^2} (\langle \rho D_i (\nabla \xi)^2 | Y_i = Z_Y, \xi = \eta \rangle P_{Z_Y, \eta}) \\
& \quad - 2 \frac{\partial^2}{\partial Z_Y \partial Z_\eta} (\langle \rho D_i (\nabla Y_i \nabla \xi) | Y_i = Z_Y, \xi = \eta \rangle P_{Z_Y, \eta}) \\
& \quad - \frac{\partial}{\partial Z_Y} (\langle \rho \dot{\omega}_i | Y_i = Z_Y, \xi = \eta \rangle P_{Z_Y, \eta}).
\end{aligned} \tag{4.19}$$

Eqn. 4.19 is then multiplied by Z_Y and integrated over Z_Y . The resulting equation is the

following unclosed CMC formulation of species transport equation,

$$\begin{aligned}
\frac{\partial \langle \rho Y_i | \xi = \eta \rangle P_\eta}{\partial t} + \nabla \cdot (\langle \rho Y_i \mathbf{u} | \xi = \eta \rangle P_\eta) &= -\frac{\partial^2}{\partial \eta^2} (\langle \rho D_i (\nabla \xi)^2 Y_i | \xi = \eta \rangle P_\eta) \\
&+ \frac{\partial}{\partial \eta} (\langle 2\rho D_i (\nabla Y_i \nabla \xi) | \xi = \eta \rangle P_\eta) \\
&- \frac{\partial}{\partial \eta} (\langle \nabla \cdot [\rho (D_\xi - D_i) \nabla \xi] Y_i | \xi = \eta \rangle P_\eta) \\
&+ \nabla^2 (\langle \rho D_i Y_i | \xi = \eta \rangle P_\eta) - \nabla \cdot (\langle \nabla (\rho D_i) Y_i | \xi = \eta \rangle P_\eta) \\
&+ \langle \rho \dot{\omega}_i | \xi = \eta \rangle P_\eta.
\end{aligned} \tag{4.20}$$

The terms on the LHS of Eq. 4.20 describe the transient evolution of Y_i and the advection of Y_i in physical space, respectively. The first three conditionally averaged terms on the RHS, describing the diffusion of conditionally averaged quantities across conserved scalar space, involve the product of the dissipation and the scalar Y_i (DS), the cross dissipation of ξ and Y_i (CD), and differential diffusion (DD), respectively. The next two terms involve the diffusion of conditional averaged quantities in physical space. The spatial diffusion terms are relatively small for high Reynolds number [7], and are often neglected. In the present implementation, these terms are kept due to the possibility of finding lower local Reynolds number values in the near field of the flame. The last term contains the conditional average of the chemical source term. The closure of the terms in Eq. 4.20 is presented in Section 4.5.

A comparison between the differential diffusivity formulation of Eq. 4.20 and the equal diffusivity formulation of Eq. 4.7 shows differences in the diffusion terms. The DS and CD terms in Eq. 4.20 are of a similar form to the diffusion terms in Eq. 4.7, with the exception of the diffusion coefficients, where the assumption of $D_i = D_\xi$ is not made. Also different from the formulation for equal diffusivity, is the presence of the third term on the RHS, which disappears if $D_i = D_\xi$.

An alternate approach to the derivation of Eq. 4.20 involving the formulation of a transport equation for $\psi_\eta Y_i$ results in the same equation. The $\psi_\eta Y_i$ transport equation is obtained by combining the transport equations for ψ_η (Eq. 4.5 for a single scalar variable) and Y_i (Eq. 2.8). This approach is employed for the derivation of the non-equal diffusivity formulation of the CMC enthalpy transport equation in Section 4.4.

4.4 CMC Formulation of Enthalpy Equation Including Differential Diffusion

The derivation of the enthalpy equation is proposed in the present investigation which follows a similar approach outlined in Klimenko and Bilger [7] for the derivation of the species transport equation. This approach involves the derivation of the governing equation for the product $h\psi_\eta$, by using the transport equations for h and ψ_η . The transport equation for the fine-grain PDF of the mixture fraction, $\psi_\eta = \psi(\eta)$, is obtained by setting $\phi = \xi$ in Eq. 4.5. To introduce the enthalpy h , Eq. 4.5 is multiplied by h , resulting in

$$h \frac{\partial \rho \psi_\eta}{\partial t} + h \nabla \cdot (\rho \mathbf{u} \psi_\eta) = -h \frac{\partial}{\partial \eta} (\psi_\eta \nabla \cdot (\rho D_\xi \nabla \xi)), \quad (4.21)$$

since $\phi = \xi$, then $Z = \eta$, $D = D_\xi$, and $W = 0$. Similarly, the transport equation for h , Eq. 2.15, is multiplied by ψ , resulting in

$$\psi_\eta \rho \frac{\partial h}{\partial t} + \psi_\eta \rho (\mathbf{u} \cdot \nabla h) = \psi_\eta \nabla \cdot (\rho \alpha \nabla h) - \psi_\eta \nabla \cdot \left[\sum_i (\rho h_i (\alpha - D_i) \nabla Y_i) \right] + \psi_\eta \rho s_h. \quad (4.22)$$

Equations 4.21 and 4.22 are summed, and with some rearrangement of the resulting equation, a transport equation for $h\psi_\eta$ is obtained,

$$\begin{aligned} \frac{\partial \rho h \psi_\eta}{\partial t} + \nabla \cdot (\rho \mathbf{u} h \psi_\eta) = & - \frac{\partial}{\partial \eta} (h \psi_\eta \nabla \cdot (\rho D_\xi \nabla \xi)) + \psi_\eta \nabla \cdot (\rho \alpha \nabla h) \\ & - \psi_\eta \nabla \cdot \left[\sum_i (\rho h_i (\alpha - D_i) \nabla Y_i) \right] + \psi_\eta \rho s_h. \end{aligned} \quad (4.23)$$

Similar to the derivation of the species equation in Section 4.3, a series of mathematical manipulation (details in Appendix B) based on the gradient operation of Eq. 4.3 is performed, to set Eq. 4.3 to an easier form for averaging. Subsequently, the transformed

equation is averaged to obtain the following unclosed form of the CMC enthalpy equation,

$$\begin{aligned}
\frac{\partial \langle \rho h | \xi = \eta \rangle P_\eta}{\partial t} + \nabla \cdot (\langle \rho \mathbf{u} h | \xi = \eta \rangle P_\eta) &= -\frac{\partial^2}{\partial \eta^2} (\langle \rho h D_\xi (\nabla \xi)^2 | \xi = \eta \rangle P_\eta) \\
&+ \frac{\partial}{\partial \eta} (\langle \rho (D_\xi + \alpha) (\nabla \xi \cdot \nabla h) | \xi = \eta \rangle P_\eta) \\
&- \sum_i \left(\frac{\partial}{\partial \eta} (\langle \rho h_i (\alpha - D_i) (\nabla \xi \cdot \nabla Y_i) | \xi = \eta \rangle P_\eta) \right) \\
&+ \nabla \cdot (\langle \rho D_\xi \nabla h | \xi = \eta \rangle P_\eta) + \nabla \cdot (\langle \rho (\alpha - D_\xi) \nabla h | \xi = \eta \rangle P_\eta) \\
&- \sum_i (\nabla \cdot (\langle \rho h_i (\alpha - D_i) \nabla Y_i | \xi = \eta \rangle P_\eta)) + \langle \rho s_h | \xi = \eta \rangle P_\eta.
\end{aligned} \tag{4.24}$$

The terms on the LHS of Eq. 4.24 describe the transient evolution of h and the advection of h in physical space, respectively. The first three conditionally averaged terms on the RHS describe the diffusion of conditionally averaged quantities across conserved scalar space, and involve the product of the dissipation and the scalar h , the cross dissipation of ξ and h , and differential diffusion, respectively. The differential diffusion term contains the cross dissipation term of ξ and Y_i . The next three terms involve the diffusion of conditional averaged quantities in physical space. Similar to the spatial diffusion terms in the CMC species transport equation (Eq. 4.20), the spatial diffusion terms in Eq. 4.24 are relatively small for high Reynolds number [7], and are often neglected. However, these terms are kept due to the possibility of finding lower local Reynolds number values in the near field of the flame. The last term contains the conditional average of the enthalpy source term. Additional details of the procedure covered in this section can be found in the more rigorous derivation in Appendix B. The closure of various terms in Eq. 4.24 will be presented in Section 4.5.

A comparison between the differential diffusivity formulation of Eq. 4.24 and the equal diffusivity formulation of Eq. 4.12 shows differences in the diffusion terms. The first terms on the RHS of Eq. 4.24 are of a similar form to the diffusion terms in Eq. 4.12, with the exception of the diffusion coefficients, where the assumption of $\alpha = D_\xi$ is not made. The third term on the RHS is not found in the equal diffusivity assumption where the α is assumed to be equal to D_i .

The approach used in the derivation of Eq. 4.20 in Section 4.3, starting from the joint PDF transport equation, Eq. 4.6, can also be employed to obtain the non-equal diffusivity CMC enthalpy formulation, Eq. 4.24. In this case, the two stochastic scalar variables are $\phi_1 = h$ and $\phi_2 = \xi$, such $P(Z_h, \eta)$.

4.5 Models for the Unclosed Terms

The CMC equations derived in Section 4.3 and 4.4 contain terms that require closure. In this section, the models used in the present study are provided. The terms for which closure models are provided include the conditional η space diffusion terms, the probability density function, the conditional chemical source term, the conditional enthalpy source term, the conditional velocity, and the conditional conditional scalar dissipation rate.

4.5.1 Closure Hypothesis for J_Y

The terms describing diffusion in η space in CMC equations, Eqs. 4.20 and 4.24, require closure. The diffusion fluxes in the species and enthalpy equations, J_Y and J_h , respectively are defined as

$$J_Y = -\frac{\partial}{\partial \eta} (\langle \rho D_i (\nabla \xi)^2 Y_i | \xi = \eta \rangle P_\eta) + \langle 2\rho D_i (\nabla Y_i \nabla \xi) | \xi = \eta \rangle P_\eta - \langle \nabla \cdot [\rho (D_\xi - D_i) \nabla \xi] Y_i | \xi = \eta \rangle P_\eta, \quad (4.25)$$

$$J_h = -\frac{\partial}{\partial \eta} (\langle \rho h D_\xi (\nabla \xi)^2 | \xi = \eta \rangle P_\eta) + \langle \rho (D_\xi + \alpha) (\nabla \xi \cdot \nabla h) | \xi = \eta \rangle P_\eta - \sum_i (\langle \rho h_i (\alpha - D_i) (\nabla \xi \cdot \nabla Y_i) | \xi = \eta \rangle P_\eta). \quad (4.26)$$

The η space diffusion terms in Eqs. 4.20 and 4.24 correspond to $\frac{\partial J_Y}{\partial \eta}$ and $\frac{\partial J_h}{\partial \eta}$, respectively.

The primary closure hypothesis described by [7] is used. The flux J_Y is assumed to take the following form,

$$J_Y = A Q_i + B \frac{\partial Q_i}{\partial \eta}. \quad (4.27)$$

Klimenko [28] reasoned that for particle motion time scales larger than the Kolmogorov time scale, the particle motion in η space occurred in uncorrelated increments. The particle motion in conserved scalar space η could then be likened to the Brownian motion of particles in physical space described by a Markov process, where future states depended only on the present state. Eq. 4.27 is a first-order relationship obtained for a diffusion process satisfying the Markov property in the form of a stochastic Smoluchowski equation (expressing the evolution of the PDF of the particle position). More specifically, the diffusion process

described by Eq. 4.27 is a type of diffusion process called an Ornstein-Uhlenbeck process, which is distinguished from a standard Brownian motion process (Wiener process) by non-constant stochastic drift (change in the average value of the diffusion process) characterized by the drift coefficient A [70]. The drift term tends the process to a long-term average value. B is the diffusion coefficient characterizing the fluctuation about the average value due to Brownian statistics (or Gaussian white noise). To preserve the linearity of the Markov process, A and B are independent of Q_i . A and B can be obtained in explicit form, in contrast to the dependence on the modelling of D_i in gradient diffusion modelling.

For initial and boundary conditions of Y_i that are related to ξ by the linear relationship $Y_i = a + b\xi$, then $Y_i = a + b\xi$ is a solution of the scalar transport equation describing the inert mixing field (Eq. 2.5 without the source term) for any velocity field. The solution $Y_i = a + b\xi$ corresponds to $Q_i = a + b\eta$ [7]. Subsequently, Eq. 4.27 becomes

$$J_Y = A(a + b\eta) + Bb. \quad (4.28)$$

The coefficients A and B can be obtained by substituting $Y = a + b\xi$ into Eq. 4.25, resulting in

$$J_Y = - \left(\frac{1}{2Le_i} \frac{\partial \rho_\eta \chi_\eta P_\eta}{\partial \eta} + \left(1 - \frac{1}{Le_i} \right) \rho_\eta M_\eta P_\eta \right) (a + b\eta) + \frac{\rho_\eta \chi_\eta P_\eta}{2Le_i} b, \quad (4.29)$$

where ρ_η and χ_η are as defined in Section 4.2. The conditional diffusion velocity M_η denotes,

$$M_\eta = \frac{\langle \nabla \cdot (\rho D_\xi \nabla \xi) | \xi = \eta \rangle}{\langle \rho | \xi = \eta \rangle}. \quad (4.30)$$

Klimenko and Bilger [7] suggested the following closure for M_η ,

$$M_\eta = \frac{1}{2\rho_\eta P_\eta} \frac{\partial \rho_\eta \chi_\eta P_\eta}{\partial \eta}. \quad (4.31)$$

It can be seen by comparing the corresponding terms in Eq. 4.28 and Eq. 4.29 that the coefficients take the following form,

$$A = -\frac{1}{2Le_i} \frac{\partial \rho_\eta \chi_\eta P_\eta}{\partial \eta} + \left(1 - \frac{1}{Le_i} \right) \rho_\eta M_\eta P_\eta, \quad (4.32)$$

and $B = \frac{\rho_\eta \chi_\eta P_\eta}{2Le_i}$.

Substituting the A and B from Eq. 4.32 into Eq. 4.27, the following expression is obtained,

$$J_Y = -\frac{1}{2Le_i} \frac{\partial \rho_\eta \chi_\eta P_\eta}{\partial \eta} Q_i - \frac{1}{2} \left(1 - \frac{1}{Le_i}\right) \frac{\partial \rho_\eta \chi_\eta P_\eta}{\partial \eta} Q_i + \frac{\rho_\eta \chi_\eta P_\eta}{2Le_i} \frac{\partial Q_i}{\partial \eta}. \quad (4.33)$$

To obtain the form of the diffusion terms in Eq. 4.20, the derivative of Eq. 4.33 is taken, and with some rearrangement, results in

$$\frac{\partial J_Y}{\partial \eta} = -\frac{1}{2} \frac{\partial^2 \rho_\eta \chi_\eta P_\eta}{\partial \eta^2} Q_i + \frac{\rho_\eta \chi_\eta P_\eta}{2Le_i} \frac{\partial^2 Q_i}{\partial \eta^2} - \frac{1}{2} \left(1 - \frac{1}{Le_i}\right) \frac{\partial \rho_\eta \chi_\eta P_\eta}{\partial \eta} \frac{\partial Q_i}{\partial \eta}. \quad (4.34)$$

The primary closure hypothesis is also used to model the enthalpy diffusion flux J_h described by Eq. 4.26. The same form for the diffusion process, $J_h = A Q_h + B \frac{\partial Q_h}{\partial \eta}$ is assumed. Following the procedure used for the closure of J_Y , the following expression for J_h is obtained,

$$J_h = -\frac{1}{2} \frac{\partial \rho_\eta \chi_\eta P_\eta}{\partial \eta} Q_h - \frac{\rho_\eta \chi_\eta P_\eta}{2} \sum_i \left(\left(1 - \frac{1}{Le_i}\right) \frac{\partial Q_i}{\partial \eta} \right) Q_{h_i} + \frac{\rho_\eta \chi_\eta P_\eta}{2} \frac{\partial Q_h}{\partial \eta}. \quad (4.35)$$

The assumption of $\alpha = D_\xi$ is made; however, the assumption of $D_i = D_\xi$ is relaxed. To obtain the form of the diffusion terms in Eq. 4.24, the derivative of Eq. 4.35 is taken, and with some rearrangement, results in

$$\frac{\partial J_h}{\partial \eta} = -\frac{1}{2} \frac{\partial^2 \rho_\eta \chi_\eta P_\eta}{\partial \eta^2} Q_h + \frac{\rho_\eta \chi_\eta P_\eta}{2} \frac{\partial^2 Q_i}{\partial \eta^2} - \frac{\partial}{\partial \eta} \left[\frac{\rho_\eta \chi_\eta P_\eta}{2} \sum_i \left(\left(1 - \frac{1}{Le_i}\right) \frac{\partial Q_i}{\partial \eta} \right) Q_{h_i} \right]. \quad (4.36)$$

Hewson *et al.* [6, 68, 67] proposed the presence of residual terms R_{DS} , R_{CD} , and R_{DD} , which were the differences between the exact DS, CD, and DD terms in Eq. 4.25 and modelled diffusion flux of 4.33. In other words, the residuals represented the error from assuming the form of Eq. 4.27. Although R_{DS} and R_{CD} were found to be the same magnitude as the modelled terms, they tended to balance each other and were generally neglected [6]. R_{DD} was found to be significant in the soot CMC equation, but small in the equations for gaseous species [69]. Following the findings reported in [6, 69], the residuals are neglected in the present study.

4.5.2 Presumed Probability Density Function

The probability density function, briefly introduced in 2.1.3, is an important quantity in CMC, as it is found in Eqs. 4.20 and 4.24. The PDF P_η in Eqs. 4.20 and 4.24 can be

related to the Favre averaged PDF by

$$\rho_\eta P_\eta = \bar{\rho} \tilde{P}(\eta, \mathbf{x}). \quad (4.37)$$

The PDF is also necessary to relate the Favre averaged mass fraction to the density-weighted conditional averaged mass fraction obtained from CMC calculations. The relationship between conditional and unconditional quantities is given by, Eq. 2.37, written as follows for the quantity $\rho\phi$ [22],

$$\overline{\rho\phi} = \int_0^1 \langle \rho\phi | \xi = \eta \rangle P(\eta) \partial\eta. \quad (4.38)$$

Using Eqs. 2.40 and 4.37, Eq. 4.38 can be expressed as

$$\tilde{\phi} = \int_0^1 \frac{\langle \rho\phi | \xi = \eta \rangle}{\langle \rho | \xi = \eta \rangle} \tilde{P}(\eta, \mathbf{x}) \partial\eta, \quad (4.39)$$

where $\langle \rho\phi | \xi = \eta \rangle / \langle \rho | \xi = \eta \rangle$ is the Favre conditional averaged mass fraction Q_i for $\phi = Y_i$ and enthalpy Q_h for $\phi = h$.

In CMC, the form of the PDF is presumed, so that the PDF transport equation, Eq. 4.14, does not need to be solved directly. However, the presumed form of the PDF should be able to provide a physically valid description of the quantities. Two commonly used forms of the PDF in non-premixed flames are the clipped Gaussian distribution and the β distribution. The shape of the presumed Favre averaged PDF at a certain location is parameterised by the local Favre averaged mixture fraction and mixture fraction variance, such that $\tilde{P}(\eta, \mathbf{x}) \equiv \tilde{P}(\eta; \tilde{\xi}(\mathbf{x}), \tilde{\xi}''^2(\mathbf{x}))$.

Clipped Gaussian PDF

The Gaussian distribution is a symmetrical distribution centered on the mean value, and the spread is determined by the variance. The PDF is given by

$$G(\eta) = \frac{1}{\sqrt{2\pi\tilde{\xi}''^2}} \exp\left(-\frac{(\eta - \tilde{\xi})^2}{2\tilde{\xi}''^2}\right). \quad (4.40)$$

The tails of the distribution described by Eq. 4.40 extends beyond the range of the mixture fraction sample space, $0 \leq \eta \leq 1$. The property that the sum of the PDF over the sample

space is equal to 1 (Eq. 2.22) is no longer true for sample space η ,

$$\int_0^1 P(\eta) d\eta \neq 1. \quad (4.41)$$

A modification is made to change the inequality of Eq. 4.41 by introducing the Favre averaged clipped Gaussian PDF, expressed as

$$\tilde{P}(\eta) = \alpha_1 \delta(\eta) + (1 - \alpha_1 - \alpha_2) P_T(\eta) + \alpha_2 \delta(1 - \eta), \quad (4.42)$$

where P_T is the Gaussian distribution in Eq. 4.40 normalized for the range of $0 \leq \eta \leq 1$,

$$P_T(\eta) = \frac{G(\eta)}{\int_0^1 G(\eta) d\eta}, \quad (4.43)$$

resulting in a change in the magnitude of the PDF in the range of $0 \leq \eta \leq 1$ to account for the tails of the PDF outside of the range. Equation 4.43 satisfies the integration property between 0 and 1. However, Eq. 4.43 does not provide a proper representation of unmixed fluid at the boundaries. To accommodate for this discrepancy, Dirac delta functions δ , with values of 1, are added at $\eta = 0$ and $\eta = 1$, as seen in Eq. 4.42. The delta functions represent the intermittency of the turbulent shear flow near the boundaries of the shear layer where the entrainment of unmixed or non-turbulent fluid results in spikes. The strengths of the delta functions are modified by the factors α_1 and α_2 . The values for α_1 and α_2 are assumed to be equal to the clipped tails of the Gaussian distribution, such that

$$\begin{aligned} \alpha_1 &= \int_{-\infty}^0 G(\eta) d\eta, \\ \text{and } \alpha_2 &= \int_1^{\infty} G(\eta) d\eta. \end{aligned} \quad (4.44)$$

The strengths of the α_1 and α_2 become stronger as the mean value approaches the boundaries of η ; in other words, the delta functions are strongest near the fuel inlet and far from the fuel jet. Figure 4.1a shows the clipped Gaussian PDF for various values of ξ and ξ'^2 . Care should be taken when using the clipped Gaussian distribution, since the discontinuities at the boundaries of η space may lead to unphysical behaviour.

β PDF

The Favre averaged β distribution is given by

$$\tilde{P}(\eta) = \frac{\eta^{\alpha-1} (1 - \eta)^{\beta-1}}{I_b}, \quad (4.45)$$

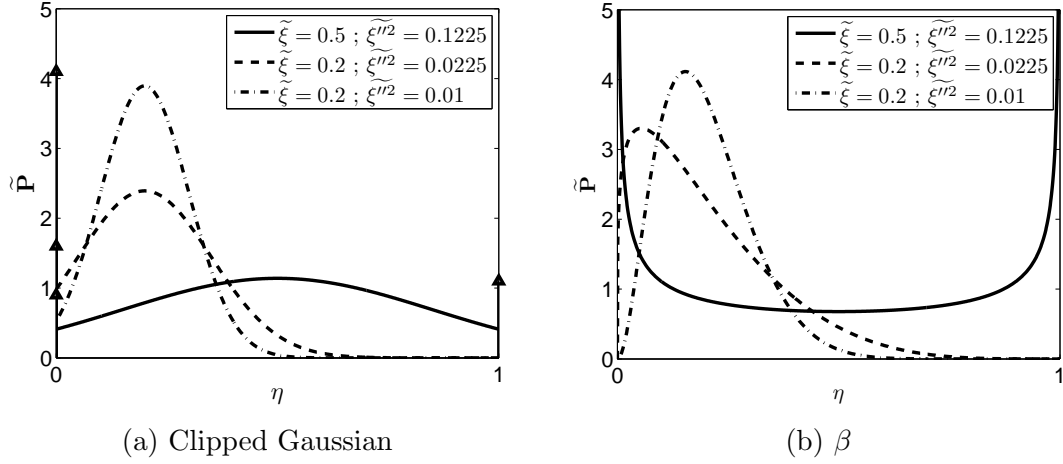


Figure 4.1: Clipped Gaussian and β distributions with for different values of $\tilde{\xi}$ and $\tilde{\xi}''^2$

where I_b is the integral

$$I_\beta = \int_0^1 \eta^{\alpha-1} (1-\eta)^{\beta-1} d\eta, \quad (4.46)$$

and the parameters α and β are

$$\alpha = \tilde{\xi} \left(\frac{\tilde{\xi}(1-\tilde{\xi})}{\tilde{\xi}''^2} - 1 \right), \quad (4.47)$$

and $\beta = (1-\tilde{\xi}) \left(\frac{\tilde{\xi}(1-\tilde{\xi})}{\tilde{\xi}''^2} - 1 \right).$

Figure 4.1b shows the β PDF for different values of $\tilde{\xi}$ and $\tilde{\xi}''^2$. The β function described by Eq. 4.45 is a smooth PDF that is generally asymmetric, but the shape approaches a symmetric Gaussian form for small ratios $\sqrt{\tilde{\xi}''^2/\tilde{\xi}}$ and $\sqrt{\tilde{\xi}''^2/(1-\tilde{\xi})}$. Unlike the discontinuous delta functions used in the clipped Gaussian distribution (Eq. 4.42) to account for the intermittency, the β distribution behaves asymptotically near the $\eta = 0$ and $\eta = 1$. Girimaji [71, 72, 73] showed that the β distribution provided an accurate representation of $\tilde{P}(\eta)$, and was supported by various DNS studies [74]. The tradeoff was the increase in computational cost due to the need to solve the integral I_b . The beta PDF tends to give

better predictions for large variances of the mixture fraction. However, both forms of the PDF have been show to perform similarly in hydrogen jet flame computations.

4.5.3 Chemical Source Term

The highly non-linear averaged reaction rates, in the form of Eq. 2.68, is described in Section 2.3.4. One of the main motivations of CMC methods is the reduction in the order of the reaction rate. When the source term is conditionally averaged on the mixture fraction, such as in Eqs. 4.15 and 4.20, the conditionally averaged terms involving the fluctuations Y'' and T'' , are found to be small [7]. The higher order terms seen in Eq. 2.68 can then be neglected by first order closure and the Favre averaged chemical reaction rate can be describe as a function of the Favre conditional species mass fraction and temperature, $\dot{\omega}_{\eta,i}(Q_i, Q_T)$, where $Q_T = \langle \rho T | \xi = \eta \rangle / \langle \rho | \xi = \eta \rangle$. The first order closure approximation to the conditional chemical source term of species i is subsequently expressed by the sum of the rates of each reaction involving the species i ,

$$\omega_{\eta,i} = \frac{M_i}{\rho_\eta} \sum_{l=1}^L (\nu''_{i,l} - \nu'_{i,l}) \left(k_{f,l} \prod_{j=1}^N [X_j | \eta]^{\nu'_{j,l}} - k_{r,l} \prod_{j=1}^N [X_j | \eta]^{\nu''_{j,l}} \right), \quad (4.48)$$

where L is the number of elementary reactions, N is the number of reactants and products for each reaction l , ν is the stoichometric coefficients of the reactants (denoted by ') and products (denoted by ") . The conditional averaged concentration of species i is related to the conditional averaged mass fraction by

$$[X_i | \eta] = \frac{\rho_\eta Q_i}{M_i}, \quad (4.49)$$

where M_i is the molecular weight of species i . k is the temperature dependent rate constant acquired in Arrhenius form,

$$k = AT^n \exp\left(-\frac{E}{RT}\right), \quad (4.50)$$

and this relationship is also seen in the unaveraged form, Eq. 2.67. The subscripts, f and r indicate forward and reverse reactions, and are related by

$$k_r = \frac{k_f}{K_c}, \quad (4.51)$$

where the equilibrium constant K_c is often found tabulated.

The validity of the first order closure depends on the magnitudes of the conditional fluctuations. The first order closure is a good approximation for flames far from extinction.

4.5.4 Radiative Heat Loss

The conditional averaged enthalpy source term, as shown in Eq. 4.13 and 4.24, typically accounts for radiation heat losses in turbulent reacting flows. Under the assumption of optically thin flame, that is, at each point the source has an unimpeded isotropic view of the cold surroundings resulting in negligible radiative heat transfer within the flame itself, the radiative heat loss rate per unit volume [$\frac{W}{m^3}$] is given by

$$s_h(T, p_i) = 4\sigma \sum_i p_i K_{P,i} (Q_T^4 - Q_{T,b}^4), \quad (4.52)$$

where $\sigma = 5.670373 \cdot 10^{-8} \frac{W}{m^2 K^4}$ is the Stefan-Boltzmann constant, p_i is the partial pressure of the i th species, $K_{P,i}$ is the Planck mean absorption coefficient of the i th species, and $Q_{T,b}$ is the Favre conditional background temperature. The Planck mean absorption coefficient is a path-length independent quantity that is a function of temperature, and various empirical correlations had been proposed for $K_{P,i}$. The partial pressure is obtained by the use of the ideal gas law (Eq. 2.16) weighted with the mass fraction,

$$p_i = \frac{Y_i \rho R Q_T}{M_i}. \quad (4.53)$$

4.5.5 Conditional Velocity and Turbulent Flux

The advection term in CMC species equation, Eq. 4.20, can be decomposed as,

$$\begin{aligned} \nabla \cdot (\langle \rho Y_i \mathbf{u} | \xi = \eta \rangle P_\eta) &= \nabla \cdot [(\langle \rho Y_i | \xi = \eta \rangle \langle \mathbf{u} | \xi = \eta \rangle + \langle \rho Y_i' \mathbf{u}' | \xi = \eta \rangle) P_\eta] \\ &= \nabla \cdot [(\rho_\eta Q_i \mathbf{u}_\eta P_\eta + \rho_\eta \langle Y_i'' \mathbf{u}'' | \xi = \eta \rangle P_\eta)]. \end{aligned} \quad (4.54)$$

The conditional turbulent flux $\langle Y_i'' \mathbf{u}'' | \xi = \eta \rangle$ is modelled using the gradient diffusion hypothesis for the scalar Q_i ,

$$\langle Y_i'' \mathbf{u}'' | \xi = \eta \rangle = -D_t \nabla Q_i, \quad (4.55)$$

such that Eq. 4.54 becomes

$$\nabla \cdot (\langle \rho Y_i \mathbf{u} | \xi = \eta \rangle P_\eta) = \nabla \cdot [(\rho_\eta Q_i \mathbf{u}_\eta P_\eta - D_t \rho_\eta P_\eta \nabla Q_i)]. \quad (4.56)$$

The turbulent diffusivity D_t is given by

$$D_t = \frac{\nu_t}{Sc_t} = \frac{C_\mu k^2}{Sc_t \varepsilon}, \quad (4.57)$$

where ν_t is the turbulent kinematic viscosity, Sc_t is the turbulent Schmidt number, and C_μ is an empirically constant typically with a value of 0.09. Similarly, the advection in the CMC enthalpy equation, Eq. 4.24, can be expressed as,

$$\nabla \cdot (\langle \rho h \mathbf{u} | \xi = \eta \rangle P_\eta) = \nabla \cdot [(\rho_\eta Q_h \mathbf{u}_\eta P_\eta - D_t \rho_\eta P_\eta \nabla Q_h)]. \quad (4.58)$$

The Favre conditional averaged velocity \mathbf{u}_η is approximated using the linear model proposed by Kuznetsov and Sabelnikov [75]. The model assumes a linear relationship in η space, expressed as,

$$u_{\eta,k} = \tilde{u}_k + \frac{\widetilde{u_k'' \xi''}}{\widetilde{\xi''^2}} (\eta - \tilde{\xi}), \quad (4.59)$$

where $u_{\eta,k}$ is one component of the vector \mathbf{u}_η . The $\widetilde{u_k'' \xi''}$ is once again modelled by the gradient diffusion hypothesis described by Eq. 2.61, such that

$$u_{\eta,k} = \tilde{u}_k - \frac{D_t}{\widetilde{\xi''^2}} \frac{\partial \tilde{\xi}}{\partial x_k} (\eta - \tilde{\xi}). \quad (4.60)$$

The linear model is considered a good approximation for many flows for η values within two standard deviations of $\tilde{\xi}$ [76]. The linear model is commonly used due to its ease of implementation and low computational requirement.

4.5.6 Conditional Scalar Dissipation Rate

The modelling of the conditional scalar dissipation rate, χ_η , is one of the major areas of ongoing research in CMC methods. Various models have been proposed under different assumptions, such as constant value for all η values, homogeneous turbulence [77, 78], and inhomogeneous turbulence [76]. In the present investigation, χ_η is modelled using the Amplitude Mapping Closure (AMC) model developed by O'Brien and Jiang [77]. The model is derived from the homogeneous PDF transport equation using the mapping closure solution for the scalar PDF. The PDF initially has a double delta distribution and later relaxes to a Gaussian distribution. The model assumes that χ_η is proportional to a function of η independent of $\tilde{\xi}$ and $\widetilde{\xi''^2}$, $G(\eta) = \exp(-2 \cdot \text{erf}^{-1}(2\eta - 1)^2)$ such that,

$$\chi_\eta = \frac{\tilde{\chi} G(\eta)}{\int_0^1 G(\eta) P(\eta) d\eta}, \quad (4.61)$$

where $\tilde{\chi}$ is the Favre averaged scalar dissipation rate described by Eq. 2.63. Equation 2.63 is also unclosed due to the correlation $\widetilde{\nabla\phi'' \cdot \nabla\phi''}$. Peters [11] proposes the expression

$$\tilde{\chi} = C_\chi \frac{\varepsilon}{k} \widetilde{\xi''^2}, \quad (4.62)$$

where C_χ is a constant of proportionality dependent on the nature of the flow. The value of $C_\chi = 2$ is found to provide good results in the study of an inert jet [79], and this value is retained in the present study. Equation 4.62 is obtained by assuming proportionality between the integral time scale of the mixing field $\tau_i = \widetilde{\xi''^2}/\tilde{\chi}$, and time scale of the turbulent flow $\tau = k/\varepsilon$, such that

$$\tau = C_\chi \tau_i. \quad (4.63)$$

Other models have also been proposed for the closure of $\tilde{\chi}$, but are not examined in the present investigation.

The form of χ_η is shown in Fig. 4.2. The AMC model results in a χ_η profile that is symmetrical and centered at $\eta = 0.5$. AMC requires some unmixed fluid to be present. The AMC model is used for its good compromise between accuracy and ease of implementation.

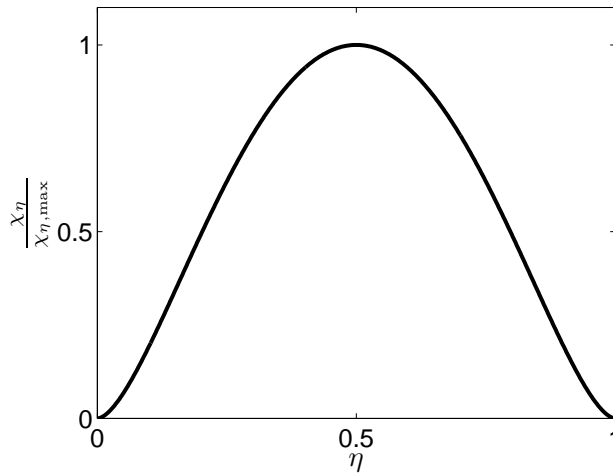


Figure 4.2: χ_η distribution modelled by AMC

4.6 Summary of CMC Equations with Differential Diffusion

The closed form of the CMC equations are presented in this section. Substitution of Eqs. 4.34, 4.36, 4.56, and 4.58 into Eqs. 4.20 and 4.24, results in

$$\begin{aligned}
\frac{\partial \rho_\eta Q_i P_\eta}{\partial t} + \nabla \cdot [(\rho_\eta Q_i \mathbf{u}_\eta P_\eta - D_t \rho_\eta P_\eta \nabla Q_i)] &= -\frac{1}{2} \frac{\partial^2 \rho_\eta \chi_\eta P_\eta}{\partial \eta^2} Q_i + \frac{\rho_\eta \chi_\eta P_\eta}{2L e_i} \frac{\partial^2 Q_i}{\partial \eta^2} \\
&- \frac{1}{2} \left(1 - \frac{1}{L e_i}\right) \frac{\partial \rho_\eta \chi_\eta P_\eta}{\partial \eta} \frac{\partial Q_i}{\partial \eta} + \nabla^2 (\langle \rho D_i Y_i | \xi = \eta \rangle P_\eta) \\
&- \nabla \cdot (\langle \nabla (\rho D_i) Y_i | \xi = \eta \rangle P_\eta) + \rho_\eta \dot{\omega}_{\eta,i} P_\eta,
\end{aligned} \tag{4.64}$$

and

$$\begin{aligned}
\frac{\partial \rho_\eta Q_h P_\eta}{\partial t} + \nabla \cdot [(\rho_\eta Q_h \mathbf{u}_\eta P_\eta - D_t \rho_\eta P_\eta \nabla Q_h)] &= -\frac{1}{2} \frac{\partial^2 \rho_\eta \chi_\eta P_\eta}{\partial \eta^2} Q_h + \frac{\rho_\eta \chi_\eta P_\eta}{2} \frac{\partial^2 Q_i}{\partial \eta^2} \\
&- \frac{\partial}{\partial \eta} \left[\frac{\rho_\eta \chi_\eta P_\eta}{2} \sum_i \left(\left(1 - \frac{1}{L e_i}\right) \frac{\partial Q_i}{\partial \eta} \right) Q_{h_i} \right] \\
&+ \nabla \cdot (\langle \rho D_\xi \nabla h | \xi = \eta \rangle P_\eta) + \nabla \cdot (\langle \rho (\alpha - D_\xi) \nabla h | \xi = \eta \rangle P_\eta) \\
&- \sum_i (\nabla \cdot (\langle \rho h_i (\alpha - D_i) \nabla Y_i | \xi = \eta \rangle P_\eta)) + \rho_\eta s_{\eta,h} P_\eta.
\end{aligned} \tag{4.65}$$

Similar to the equal diffusivity formulation in Section 4.2, Eqs. 4.64 and 4.65 can be modified to conservative form by subtracting Eq. 4.14 multiplied Q_i and Q_h , respectively. The resulting equations are

$$\begin{aligned}
\rho_\eta P_\eta \frac{\partial Q_i}{\partial t} + \nabla \cdot [(\rho_\eta Q_i \mathbf{u}_\eta P_\eta - D_t \rho_\eta P_\eta \nabla Q_i)] - \nabla \cdot (\rho_\eta \mathbf{u}_\eta P_\eta) Q_i &= \frac{\rho_\eta \chi_\eta P_\eta}{2L e_i} \frac{\partial^2 Q_i}{\partial \eta^2} \\
&- \frac{1}{2} \left(1 - \frac{1}{L e_i}\right) \frac{\partial \rho_\eta \chi_\eta P_\eta}{\partial \eta} \frac{\partial Q_i}{\partial \eta} + \nabla^2 (\langle \rho D_i Y_i | \xi = \eta \rangle P_\eta) \\
&- \nabla \cdot (\langle \nabla (\rho D_i) Y_i | \xi = \eta \rangle P_\eta) + \rho_\eta \dot{\omega}_{\eta,i} P_\eta,
\end{aligned} \tag{4.66}$$

and

$$\begin{aligned}
\rho_\eta P_\eta \frac{\partial Q_h}{\partial t} + \nabla \cdot [(\rho_\eta Q_h \mathbf{u}_\eta P_\eta - D_t \rho_\eta P_\eta \nabla Q_h)] - \nabla \cdot (\rho_\eta \mathbf{u}_\eta P_\eta) Q_h &= \frac{\rho_\eta \chi_\eta P_\eta}{2} \frac{\partial^2 Q_i}{\partial \eta^2} \\
- \frac{\partial}{\partial \eta} \left[\frac{\rho_\eta \chi_\eta P_\eta}{2} \sum_i \left(\left(1 - \frac{1}{Le_i} \right) \frac{\partial Q_i}{\partial \eta} \right) Q_{h_i} \right] & \\
+ \nabla \cdot (\langle \rho D_\xi \nabla h | \xi = \eta \rangle P_\eta) + \nabla \cdot (\langle \rho (\alpha - D_\xi) \nabla h | \xi = \eta \rangle P_\eta) & \\
- \sum_i (\nabla \cdot (\langle \rho h_i (\alpha - D_i) \nabla Y_i | \xi = \eta \rangle P_\eta)) + \rho_\eta s_{\eta,h} P_\eta. &
\end{aligned} \tag{4.67}$$

In Eq. 4.66, the first term on the RHS is of a similar form to the diffusion term found in the Eq. 4.15, except for the presence of the inverse of the Lewis number. Hewson *et al.* [67] found this term to be relatively small for the soot transport equation, due to the high Lewis number of soot. For the low Lewis number of hydrogen, the converse is expected; the term will have a greater significance when differential diffusivity is considered. Also different from the formulation in the η space diffusion for equal diffusivity is the presence of the second term on the RHS of Eq. 4.66. The term increases in magnitude as the Lewis number deviates from unity, and approaches zero as the Lewis number tends to unity.

In Eq. 4.67, the first term on the RHS is the same as the diffusion term in Eq. 4.16, due to the assumption of $\alpha = D_\xi$. The second term on the RHS of Eq. 4.67, is not found in the equal species diffusivity formulation, since the term tends to zero as the value of D_i approaches α . This term accounts for the differential diffusion effects of chemical species.

Equations 4.66 and 4.67 are used in the discretisation and implementation of CMC in Chapter 5.

Chapter 5

Implementation of Conditional Moment Closure

The CMC transport equations derived in Chapter 4 are used in the solution of a turbulent flame. This chapter describes the general methodology in applying the CMC model in turbulent flame simulations. The chapter begins by providing an overview of the computational routine used in the present investigation in obtaining the results in Chapter 6. However, the details described in this chapter are for a general implementation and are not for any specific flame, while the procedure involved specific to the flame investigated in the current study are deferred to Chapter 6. In this chapter, the CMC equations are discretised using the finite volume method. The advection scheme, PDF ratio, Lewis number approximations, and numerical solver used in the current study are discussed.

5.1 Overview of Computational Methodology

The methodology of the computations is important in obtaining accurate results in an efficient time. In CMC modelling, good initial values can aid convergence, by promoting stability and decreasing time of computation. The flow chart, shown in Fig. 5.1, provides an overview of the structure of the computation.

The first step of the computation code is to read an input file, which contains specifications of the simulation set by the user. The file includes parameters related to the initial and boundary conditions (such as initial temperature and boundary velocities), computational grid, numerical solver (such as number of iterations), turbulence model, combustion

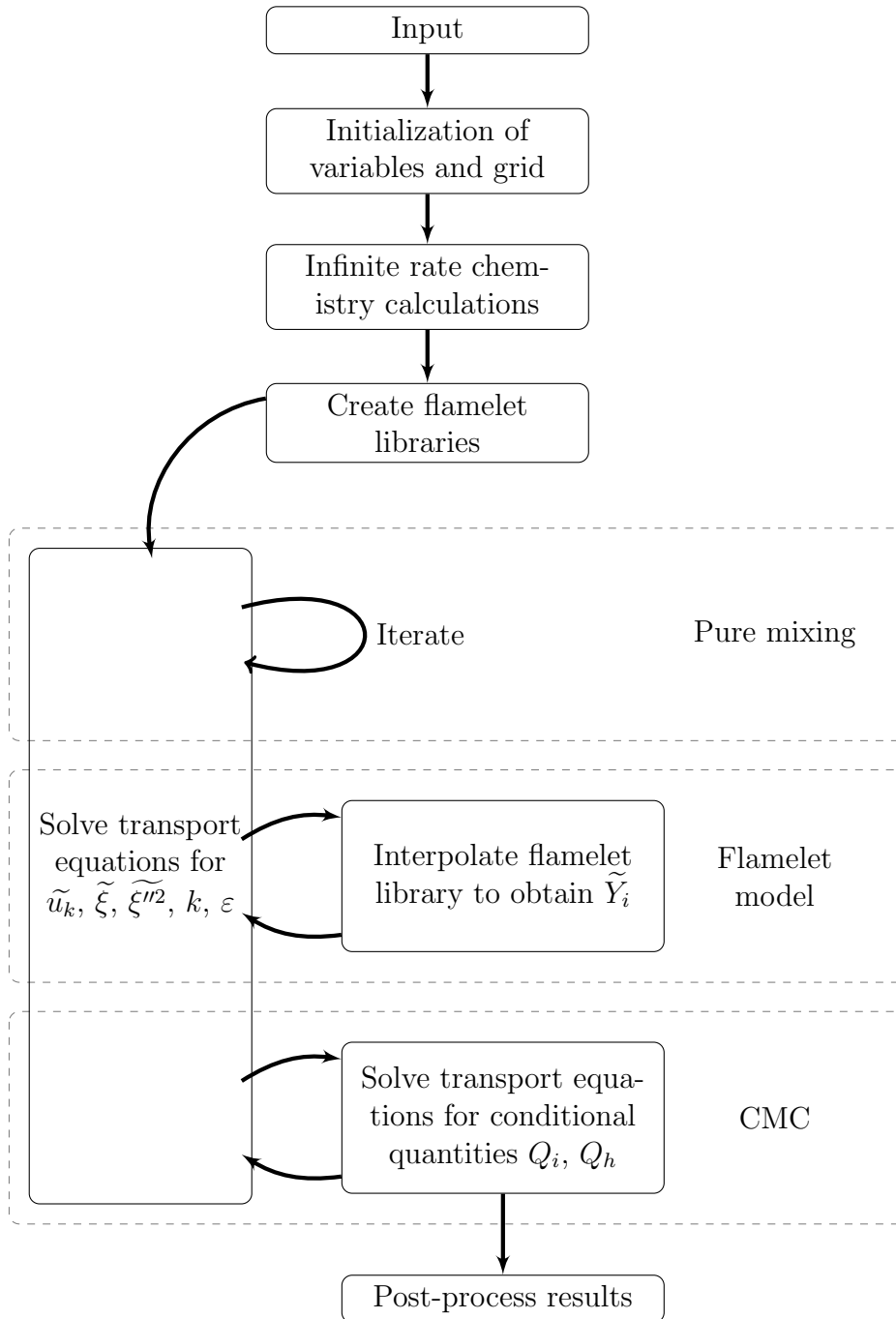


Figure 5.1: Computational methodology

model, thermodynamic (enthalpy polynomials), and chemistry mechanism. Variables are initialised based on the input parameters, such as the creation of matrices of appropriate sizes for the computational grid.

The first set of calculations are performed using a infinite rate chemistry model of an one-step irreversible reaction described in Section 2.4.1, generating the Burke-Schumann solution, and resulting in mass fractions of major species and temperature which are linear functions of η . The next step is the generation of laminar flamelet model libraries for preset values of $\tilde{\chi}$ used for interpolation in the field solution of the laminar flamelet model described in Section 2.4.2.

The flow field is first solved in the case of mixing only, i.e. no chemical reactions. This involves iteration of the discretized equations for turbulent kinetic energy k , turbulent kinetic energy dissipation ε , mixture fraction $\tilde{\xi}$, mixture fraction variance $\tilde{\xi}''$, and specific enthalpy h . After obtaining a converged pure mixing field, iterations are performed including chemistry by using the flamelet libraries. The mean scalar dissipation rate calculated from the mixture fraction field is used to interpolate the species mass fractions. The change in the mean density and temperature from chemistry considerations affects the mixing field variables, and is used in the equations for the flow field variables. The iteration between the flamelet libraries and the flow field equations is performed until convergence. The reacting flow field provides an initial condition for the CMC calculations that follows.

The CMC equations are solved for the conditional species mass fractions and enthalpy by using the value of the mean scalar dissipation from the mean mixture fraction field to obtain the conditional scalar dissipation rate, and by using the mean mixture fraction and variance to obtain the Favre averaged PDF. The Favre averaged mass fractions and enthalpy are then obtained from the conditional results by using Eq. 4.39. Subsequently, the flow field variables are updated with the mean density and temperature changes from the updated mean mass fractions and enthalpy. This process is iterated until both conditional and unconditional results reach convergence. The post-processing include outputting the conditional and unconditional quantities to data files, which can then be use for interpretation, such as in graphical representation.

5.2 Finite Volume Discretisation of the CMC equations

The method of solution employed in the present study is the finite volume method. The finite volume method lends itself well to physical interpretation, expressing the conservation

principles for a finite volume. The advantage of the method is that the integral conservation of mass, momentum, species, and energy is always satisfied over for any group of control volumes.

The CMC transport equations, Eqs. 4.66 and 4.67, are integrated over a control volume to yield discretised equations that can be solved numerically. The equations are discretised on a structured two-dimensional rectangular grid, as shown in Fig. 5.2. The positive axial direction ($x_k = x$) is designated as west (w) to east (e), while the positive radial direction $x_k = r$ is designated as south (s) to north (n). Variables with lower case subscripts indicate values at the cell boundaries, upper case subscripts indicate values at the cell center of adjacent nodes, and no direction subscript refers to the value at the node of the current computational cell. For the purpose of demonstration, the steps to obtain the

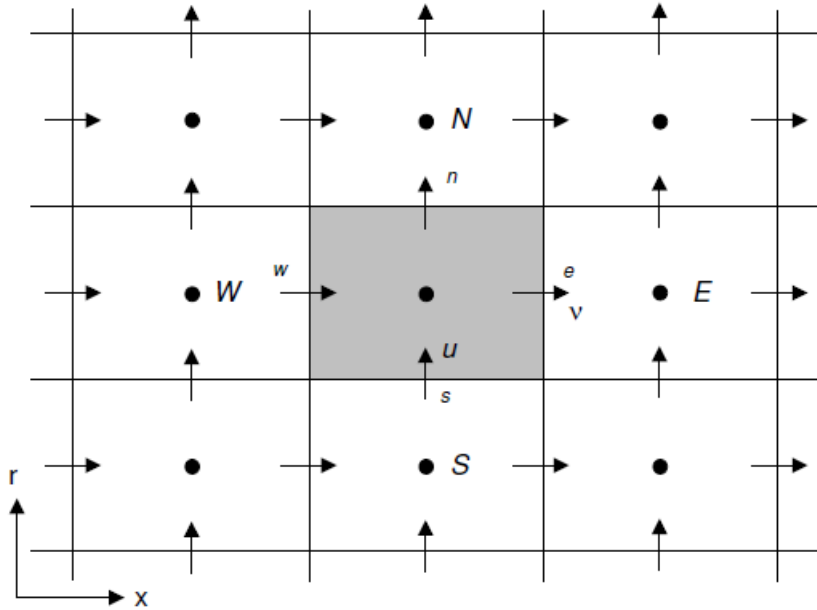


Figure 5.2: Section of computational grid, reproduced from Cleary [80]

finite volume formulation of the conditional species equation (Eq. 4.66) are presented in this section; the conditional enthalpy equation (Eq. 4.67) finite volume formulation can be obtained by following the same steps, and only the final form is presented at the end of this section. The derivation begins by integrating Eq. 4.66 over the computational cell volume. With the use of Gauss' divergence theorem expressing the volume integral of a vector field as a surface integral, and second-order midpoint approximations for volume

and surface integrals, the resulting equation becomes

$$\begin{aligned}
& \bar{\rho}_e \tilde{P}_e A_e \left(u_\eta Q_i - D_t \frac{\partial Q_i}{\partial x} \right)_e - \bar{\rho}_w \tilde{P}_w A_w \left(u_\eta Q_i - D_t \frac{\partial Q_i}{\partial x} \right)_w \\
& + \bar{\rho}_n \tilde{P}_n A_n \left(v_\eta Q_i - D_t \frac{\partial Q_i}{\partial r} \right)_n - \bar{\rho}_s \tilde{P}_s A_s \left(v_\eta Q_i - D_t \frac{\partial Q_i}{\partial r} \right)_s \\
& - \left((\bar{\rho} \tilde{P} u_\eta A)_e - (\bar{\rho} \tilde{P} u_\eta A)_w + (\bar{\rho} \tilde{P} v_\eta A)_n - (\bar{\rho} \tilde{P} v_\eta A)_s \right) Q_i \\
& = \frac{\bar{\rho} \chi_\eta \tilde{P} V}{2 L e_i} \frac{\partial^2 Q_i}{\partial \eta^2} - \frac{1}{2} \left(1 - \frac{1}{L e_i} \right) V \frac{\partial \bar{\rho} \chi_\eta \tilde{P}}{\partial \eta} \frac{\partial Q_i}{\partial \eta} \\
& + \left(\bar{\rho} D_i A \frac{\partial Q_i \tilde{P}}{\partial x} \right)_e - \left(\bar{\rho} D_i A \frac{\partial Q_i \tilde{P}}{\partial x} \right)_w + \left(\bar{\rho} D_i A \frac{\partial Q_i \tilde{P}}{\partial r} \right)_n - \left(\bar{\rho} D_i A \frac{\partial Q_i \tilde{P}}{\partial r} \right)_s \\
& + \bar{\rho} \tilde{P} V \dot{\omega}_{i,\eta},
\end{aligned} \tag{5.1}$$

where $V = r dx dr$ is the volume of the cell, $A_e = A_w = r dr$ are the area of the east and west faces, $A_n = r_n dx$ is the area of the north face, and $A_s = r_s dx$ is the area of the south face.

The first components of the advective terms in Eq. 5.1 are approximated by,

$$\bar{\rho}_k \tilde{P}_k A_k (u_{\eta,k} Q_i)_k \approx \bar{\rho}_k \tilde{P}_k A_k u_\eta [f_k Q_{i,K} + (1 - f_k) Q_i], \tag{5.2}$$

where the subscript k represents each of the directions (e, w, n, s). f_k is the weighting factor describing the relative influence of the current and adjacent computational cell, and will be discussed in Section 5.3. The quantities at the cell faces, such as in Eq. 5.2, are determined by linear interpolation between the current and adjacent computational nodes. For example, the mean density at the cell face is given by the expression,

$$\bar{\rho}_k = \bar{\rho} + \Delta x_k \frac{\bar{\rho}_K - \bar{\rho}}{\Delta x}, \tag{5.3}$$

where $\Delta x_k = x_k - x$ is the distance between the current node and the cell face and $\Delta x = x_K - x$ is the distance from the current node to the adjacent node. The second components of the advection terms are approximated using central differencing,

$$-\bar{\rho}_k \tilde{P}_k A_k \left(D_t \frac{\partial Q_i}{\partial x} \right)_k \approx -\bar{\rho}_k \tilde{P}_k A_k D_{t,k} \frac{\pm (Q_{i,K} - Q_i)}{\Delta x_k}, \tag{5.4}$$

where \pm takes the addition operator for north and east terms and the subtraction operator for south and west terms. The fluxes are then expressed by

$$\bar{\rho}_k \tilde{P}_k A_k \left(u_{\eta,k} Q_i - D_t \frac{\partial Q_i}{\partial x_k} \right)_k \approx \bar{\rho}_k \tilde{P}_k A_k \left(u_{\eta,k} [f_k Q_{i,K} + (1 - f_k) Q_i] - D_{t,k} \frac{\pm (Q_{i,K} - Q_i)}{\Delta x_k} \right). \quad (5.5)$$

Combining Eq. 5.5 with the last term on the LHS of Eq. 5.1 resulting from the conversion to conservative form, Eq. 5.5 becomes

$$J_k \approx \bar{\rho}_k \tilde{P}_k A_k \left(u_{\eta,k} f_k (Q_{i,K} - Q_i) - D_{t,k} \frac{\pm (Q_{i,K} - Q_i)}{\Delta x_k} \right). \quad (5.6)$$

The flux leaving one cell face is exactly equal to the flux entering its neighbouring cell.

The terms involving fluxes in η space also require discretisation. The η space, with boundaries at $\eta = 0$ and $\eta = 1$, is discretised on a one dimensional grid. The η nodes are centered in each η cells. The subscripts $+$ and $-$ refer to values at adjacent η nodes. Second order central differencing obtained from the truncation of Taylor series expansions is used for the derivatives in η space such that,

$$\frac{\partial Q_i}{\partial \eta} = \frac{\Delta \eta_- (Q_{i,+} - Q_i)}{\Delta \eta \Delta \eta_+} + \frac{\Delta \eta_+ (Q_i - Q_{i,-})}{\Delta \eta \Delta \eta_-}, \quad (5.7)$$

and

$$\frac{\partial^2 Q_i}{\partial \eta^2} = \frac{Q_{i,+} \Delta \eta_- + Q_{i,-} \Delta \eta_+ - Q \Delta \eta}{\frac{1}{2} \Delta \eta \Delta \eta_+ \Delta \eta_-}, \quad (5.8)$$

where $\Delta \eta = \frac{1}{2} (\eta_+ - \eta_-)$, $\Delta \eta_+ = \eta_+ - \eta$, and $\Delta \eta_- = \eta - \eta_-$.

The resulting finite volume form of conditional species equation, Eq. 4.66, is given as

$$\begin{aligned} & \sum_k \pm \frac{\bar{\rho}_k A_k}{\bar{\rho} \tilde{P} V} \left(u_{\eta,k} f_k \tilde{P}_k (Q_{i,K} - Q_i) - D_{t,k} \tilde{P}_k \frac{\pm (Q_{i,K} - Q_i)}{\Delta x_k} - D_i \tilde{P}_k \frac{\pm (Q_{i,K} - Q_i)}{\Delta x_k} \right) \\ &= \frac{\chi_\eta}{2Le_i} \left(\frac{Q_{i,+} \Delta \eta_- + Q_{i,-} \Delta \eta_+ - Q \Delta \eta}{\frac{1}{2} \Delta \eta \Delta \eta_+ \Delta \eta_-} \right) \\ & - \frac{1}{2} \left(1 - \frac{1}{Le_i} \right) \left(\frac{\partial \chi_\eta}{\partial \eta} + \frac{\chi_\eta}{\bar{\rho} \tilde{P}} \frac{\partial \bar{\rho} \tilde{P}}{\partial \eta} \right) \left(\frac{\Delta \eta_- (Q_{i,+} - Q_i)}{\Delta \eta \Delta \eta_+} + \frac{\Delta \eta_+ (Q_i - Q_{i,-})}{\Delta \eta \Delta \eta_-} \right) \\ & + \dot{\omega}_{i,\eta}, \end{aligned} \quad (5.9)$$

where $\frac{\partial \chi_\eta}{\partial \eta}$ is also discretized by central differencing similar to Eq. 5.7. Equation 5.9 is arranged into the following form to facilitate numerical solution by expressing as a sum of species mass fractions and coefficients,

$$a_p Q_i = a_e Q_{i,e} + a_w Q_{i,w} + a_n Q_{i,n} + a_s Q_{i,s} + a_+ Q_{i,+} + a_- Q_{i,-} + b, \quad (5.10)$$

where the coefficients are,

$$a_e = \frac{\bar{\rho}_e \tilde{P}_e A_e}{\bar{\rho} \tilde{P} V} \left(-u_\eta f_e + \frac{(D_t + D_i)}{\Delta x} \right), \quad (5.11a)$$

$$a_w = \frac{\bar{\rho}_w \tilde{P}_w A_w}{\bar{\rho} \tilde{P} V} \left(u_\eta f_w + \frac{(D_t + D_i)}{\Delta x} \right), \quad (5.11b)$$

$$a_n = \frac{\bar{\rho}_n \tilde{P}_n A_n}{\bar{\rho} \tilde{P} V} \left(-v_\eta f_n + \frac{(D_t + D_i)}{\Delta r} \right), \quad (5.11c)$$

$$a_s = \frac{\bar{\rho}_s \tilde{P}_s A_s}{\bar{\rho} \tilde{P} V} \left(v_\eta f_s + \frac{(D_t + D_i)}{\Delta r} \right), \quad (5.11d)$$

$$a_+ = \frac{\chi_\eta}{Le_i \Delta \eta \Delta \eta_+} - \frac{1}{2} \left(1 - \frac{1}{Le_i} \right) \left(\frac{\Delta \eta_-}{\Delta \eta \Delta \eta_+} \right) \left(\frac{\partial \chi_\eta}{\partial \eta} + \frac{\chi_\eta}{\bar{\rho} \tilde{P}} \frac{\partial \bar{\rho} \tilde{P}}{\partial \eta} \right), \quad (5.11e)$$

$$a_- = \frac{\chi_\eta}{Le_i \Delta \eta \Delta \eta_-} - \frac{1}{2} \left(1 - \frac{1}{Le_i} \right) \left(\frac{\Delta \eta_+}{\Delta \eta \Delta \eta_-} \right) \left(\frac{\partial \chi_\eta}{\partial \eta} + \frac{\chi_\eta}{\bar{\rho} \tilde{P}} \frac{\partial \bar{\rho} \tilde{P}}{\partial \eta} \right), \quad (5.11f)$$

$$a_p = a_e + a_w + a_n + a_s + a_+ + a_-, \quad (5.11g)$$

$$b = \dot{\omega}_{i,\eta}. \quad (5.11h)$$

The conditional enthalpy transport equation, Eq. 4.67 is also discretized in similar fashion, resulting in the form,

$$a_p Q_h = a_e Q_{h,e} + a_w Q_{h,w} + a_n Q_{h,n} + a_s Q_{h,s} + a_+ Q_{h,+} + a_- Q_{h,-} + b, \quad (5.12)$$

with coefficients,

$$a_e = \frac{\bar{\rho}_e \tilde{P}_e A_e}{\bar{\rho} \tilde{P} V} \left(-u_\eta f_e + \frac{(D_t + D_i)}{\Delta x} \right), \quad (5.13a)$$

$$a_w = \frac{\bar{\rho}_w \tilde{P}_w A_w}{\bar{\rho} \tilde{P} V} \left(u_\eta f_w + \frac{(D_t + D_i)}{\Delta x} \right), \quad (5.13b)$$

$$a_n = \frac{\bar{\rho}_n \tilde{P}_n A_n}{\bar{\rho} \tilde{P} V} \left(-v_\eta f_n + \frac{(D_t + D_i)}{\Delta r} \right), \quad (5.13c)$$

$$a_s = \frac{\bar{\rho}_s \tilde{P}_s A_s}{\bar{\rho} \tilde{P} V} \left(v_\eta f_s + \frac{(D_t + D_i)}{\Delta r} \right), \quad (5.13d)$$

$$a_+ = \frac{\chi_\eta}{\Delta \eta \Delta \eta_+}, \quad (5.13e)$$

$$a_- = \frac{\chi_\eta}{\Delta \eta \Delta \eta_-}, \quad (5.13f)$$

$$a_p = a_e + a_w + a_n + a_s + a_+ + a_-, \quad (5.13g)$$

$$b = s_{\eta,h} - \frac{1}{\bar{\rho} \tilde{P}} \frac{\partial}{\partial \eta} \left[\frac{\bar{\rho} \chi_\eta \tilde{P}}{2} \sum_i \left(\left(1 - \frac{1}{Le_i} \right) \frac{\partial Q_i}{\partial \eta} \right) Q_{h_i} \right] - \sum_i \left(\frac{\partial}{\partial x_k} (\bar{\rho} Q_{h_i} \tilde{P} (\alpha - D_i)) \frac{\partial Q_i}{\partial x_k} \right), \quad (5.13h)$$

where the second term in b is expressed as,

$$\begin{aligned} & - \frac{1}{\bar{\rho} \tilde{P}} \frac{\partial}{\partial \eta} \left[\frac{\rho_\eta \chi_\eta P_\eta}{2} \sum_i \left(\left(1 - \frac{1}{Le_i} \right) \frac{\partial Q_i}{\partial \eta} \right) Q_{h_i} \right] \\ & = - \sum_i \frac{1}{2} \left[\left(1 - \frac{1}{Le_i} \right) \left(\chi_\eta \frac{\partial^2 Q_i}{\partial \eta^2} Q_{h_i} + \frac{1}{\bar{\rho} \tilde{P}} \frac{\partial \bar{\rho} \chi_\eta \tilde{P}}{\partial \eta} \frac{\partial Q_i}{\partial \eta} Q_{h_i} + \chi_\eta \frac{\partial Q_i}{\partial \eta} \frac{\partial Q_{h_i}}{\partial \eta} \right) \right] \\ & - \sum_i (\nabla \cdot (\langle \rho h_i (\alpha - D_i) \nabla Y_i | \xi = \eta \rangle P_\eta)). \end{aligned} \quad (5.14)$$

5.3 Advection Scheme

The weighting factor f_k for the advection term, Eq. 5.5 is required, in order to estimate the scalar quantities at the cell faces. A power-law interpolation scheme [81], which is a

modification of the hybrid scheme developed by Spalding [82] switching between central and upwind differencing, is used in the calculation of the advective terms. Central differencing corresponds to a linear interpolation between the centers of adjacent cells. In central differencing, a node is equally influenced by all its neighbouring nodes, such that the direction of flow is not considered. For large Peclet numbers ($Pe \geq 2$) described by Eq. 3.5, the transportiveness is not captured by the central differencing scheme, resulting in unbounded solutions. The upwind differencing scheme accounts for the direction of the flow by obtaining values at cell faces from the upwind node, resulting in solutions that are bounded. The tradeoff is a decrease in accuracy from the second-order Taylor series truncation error of the central differencing scheme to first-order error. The hybrid scheme of Spalding [82] switches from central differencing for low Peclet numbers ($|Pe| \leq 2$) to the upwind scheme for high Peclet numbers ($|Pe| > 2$). For the hybrid scheme, Patankar [81] found that the error at ($|Pe| = 2$) was rather large, and subsequently proposed a power-law expression. For the power-law scheme, the weighting factor is given by

$$\begin{aligned}
 f_k &= -u_k && \text{for } Pe < 10, \\
 f_k &= \frac{(1 - 0.1|Pe_k|)^5}{Pe_k} - \frac{1}{Pe_k} - 1 && \text{for } -10 \leq Pe \leq 0, \\
 f_k &= \frac{(1 - 0.1|Pe_k|)^5}{Pe_k} + \frac{1}{Pe_k} && \text{for } 0 \leq Pe \leq 10, \\
 f_k &= -Pe_k && \text{for } Pe > 10.
 \end{aligned} \tag{5.15}$$

The power-law scheme is identical with the hybrid scheme for $|Pe| > 10$. Using Eq. 5.15, the advective coefficients in Eqs. 5.11 and 5.13 can be expressed in a compact form,

$$a_k = \frac{\bar{\rho}_k \tilde{P}_k A_k}{\bar{\rho} \tilde{P} V} \left(\llbracket \pm u_k, 0 \rrbracket + \left\llbracket \frac{D_t (1 - 0.1|Pe_k|)^5}{\Delta x_k}, 0 \right\rrbracket \right), \tag{5.16}$$

where the $\llbracket \rrbracket$ indicates the maximum of the quantities contained. The power-law scheme requires little additional computational expense compared to the hybrid scheme, but performs significantly better [81].

5.4 PDF Ratio

Two commonly presumed probability density functions, the clipped Gaussian and the β PDFs, were introduced in Section 4.5.2. Due to the attractive properties of the β distribution (it is continuous), it is chosen for \tilde{P} in the present investigation.

The discretized CMC equations coefficients, Eqs. 5.11 and 5.13, contain ratios involving the PDF. The convective term involves the ratio of \tilde{P} at the cell face to \tilde{P} at the cell center, which characterises the relative influence of the spatial advection terms to the chemical source term and η space diffusion terms. If the PDF ratio is large, the evolution of the conditional quantities, Q_i or Q_h , is determined mainly by spatial flux. On the other hand, small PDF ratios indicates that the solution is close to the SLFM solution. Using the definition of the β distribution, Eq. 4.45, the ratio can be expressed as,

$$\frac{\tilde{P}_k}{\tilde{P}} = \frac{I_\beta}{I_{\beta,k}} \eta^{\alpha_k - \alpha} (1 - \eta)^{\beta_k - \beta}. \quad (5.17)$$

The integrals I_β and $I_{\beta,k}$ must still be determined numerically. \tilde{P}_k/\tilde{P} tends to zero or infinity as $\eta \rightarrow 0$ or $\eta \rightarrow 1$.

The coefficients $a+$ and $a-$ in Eqs. 5.11 and 5.13 involve the ratio of the gradient of \tilde{P} to \tilde{P} , which can conveniently be expressed as,

$$\frac{1}{\tilde{P}} \frac{\partial \tilde{P}}{\partial \eta} = \frac{\alpha - 1}{\eta} - \frac{\beta - 1}{1 - \eta}. \quad (5.18)$$

Equation 5.18 is a function which at $\eta = \tilde{\xi}$ has a value of 0 and a slope of $\frac{2\tilde{\xi}-1}{\tilde{\xi}(1-\tilde{\xi})}$. The magnitude of the slope increases as $\eta \rightarrow 0$ and $\eta \rightarrow 1$, and asymptotes at $\eta = 0$ and $\eta = 1$.

5.5 Numerical Solver

A numerical solver is required to solve the system of equations involving Eq. 5.10 for each chemical species and 5.12. The numerical method for the solution of the discretized equations employed in the present investigation is a modified Newton-Raphson (N-R) solver [83]. For a system of equations given by

$$\mathbf{f}(\mathbf{Q}) = 0, \quad (5.19)$$

the N-R method solves each equation $\mathbf{f} = \{f_1, f_2, \dots, f_n\}$ for each element $\mathbf{Q} = \{Q_1, Q_2, \dots, Q_n\}$ simultaneously at a one η and spatial location (x, r) . From Eq. 5.10, f_i is given by

$$f_i = -a_p Q_i + \sum a_k Q_{i,k} + b. \quad (5.20)$$

Taking a Taylor series expansion of each function f_i about Q_i and truncating terms that are higher than second order, results in

$$\mathbf{Q}^{k+1} = \mathbf{Q}^k + \Delta^k, \quad (5.21)$$

where Δ^k is obtained by the equation

$$[J]^k \Delta^k = -\mathbf{f}(\mathbf{Q}^k), \quad (5.22)$$

solved by using Gaussian elimination assisted by the LU decomposition method [83]. The elements of the Jacobian matrix $[J]$ are given by

$$J_{i,j} = \frac{\partial f_i}{\partial Q_j} = -a_{p,i} \delta_{ij} + \frac{\partial b_i}{\partial Q_j}. \quad (5.23)$$

For elementary reactions where the stoichiometric coefficients are 1, $\frac{\partial b_i}{\partial Q_j}$ can be determined analytically. Due to the large Jacobian matrix, it is impossible to solve all species at every η and spatial grid point simultaneously. Instead, the method employed here is explicit to transport in physical and mixture fraction space; in other words, Eq. 5.21 is solved at a one η and location (x, r) before marching to the next. In this case, all conditional quantities are solved for each η first at a spatial location before moving to the next spatial location.

The N-R method is generally a very efficient numerical method. However, the global convergence of the method can be poor for large changes between in the predicted values, and requires a good initial guess for the solution to converge stably. The use of SFLM solution provides reasonable initial conditions that aid convergence. In addition, the changes in the solution are usually small for steady-state CMC calculations. Additional restrictions are applied by setting limits for the possible upper value for each species, and a limit on the change in the solution for each iteration. The restriction allows the a change in the solution between iterations up to a fraction of $Q_{\max,i}$, but never exceeding $Q_{\max,i}$. The limitation set on the species mass fractions prediction can be expressed by

$$Q_i^k \leq \min(Q_i^{k-1} + CQ_{\max,i}; Q_{\max,i}), \quad (5.24)$$

where C is a fraction of $Q_{\max,i}$ that the solution can change per iteration, typically with the value of 0.1. The bound is removed as the solution reaches convergence, so not to artificially limit the solution.

5.6 Lewis Number

The Lewis number describing the ratio between thermal diffusivity and mass diffusivity (Eq. 3.2) is found in the coefficients a_+ and a_- in Eqs. 5.11 and 5.13. The Lewis number is

a function of α and D_i which are both dependent on temperature. Smooke [34] generated data for the Lewis number using detailed chemistry model for a laminar counterflow diffusion flame and found that the Lewis number for various chemical species could be fitted to a constant with reasonable agreement, except at low temperature regions. Lewis numbers approximated as constants obtained from Smooke *et al.* [34] are presented in Table 5.1.

Table 5.1: Lewis numbers from simplified transport model of Smooke [34]

Species	Le
CH_4	0.97
O_2	1.11
H_2O	0.83
CO_2	1.39
H	0.18
O	0.70
OH	0.73
HO_2	1.10
H_2	0.30
CO	1.10
H_2O_2	1.12
HCO	1.27
CH_2O	1.28
CH_3	1.00
CH_3O	1.30
N_2	1.00

The species diffusivities D_i found in the advection coefficients in Eqs. 5.11 and 5.13 is also required. The species diffusivities are estimated from the constant Lewis number using the relationship [34],

$$\rho D_i = \frac{2.58 \cdot 10^{-4}}{Le_i} \left(\frac{T}{298} \right)^{0.7}. \quad (5.25)$$

The Prandtl-Schmidt number is assumed constant, expressed by

$$\sigma = \frac{\mu}{\rho D} = 0.7. \quad (5.26)$$

Chapter 6

Hydrogen Flame Calculations

The focus of this chapter is to provide an analysis of the performance of the current CMC method with the effects of differential diffusion, as described in Chapter 4. First, the selected test case, a laboratory turbulent hydrogen-air jet flame, and the numerical setup used to replicate the experimental conditions are described. Results for the calculation of conditional and unconditional scalars are presented. Comparison is made between the results for equal and non-equal species diffusivity calculations. An analysis is also given for accounting for species diffusivities individually. A budget of the contribution of terms in the CMC equations provides a qualitative analysis. Finally, a sensitivity analysis of various factors in the simulations is presented.

6.1 Description of Experimental Study

The flame selected for the present study is one of the laboratory flames studied by Barlow and Carter [38, 39]. The flame serves as a good baseline for comparison with the CMC study with differential diffusion by Kronenburg and Bilger [61] described in Section 3.2. Other investigations [84, 85] had also pointed out the need to consider differential diffusion effects in the modelling of this flame. The measurement data and documentation are obtained from the Turbulent Nonpremixed Flames (TNF) library from Sandia National Laboratories [86].

In the experimental study, three jet flames were investigated with the following fuel compositions; undiluted hydrogen (H_2), 20% helium dilution in hydrogen, and 40% helium dilution in hydrogen. The primary objective of the experimental study of the flames was

to provide data on NO production. Raman scattering was used to measure major species concentrations (H_2 , O_2 , H_2O , N_2), while Rayleigh scattering was used for temperature measurements, and Laser-Induced Fluorescence (LIF) was used for the measurement of OH and NO concentrations. Velocity measurements were conducted at ETH Zurich [87] using Laser-Doppler Velocimetry. Measurements were made at several streamwise locations along the flame. In this study, only the undiluted hydrogen flame is studied.

Table 6.1: Summary of flame conditions

Nozzle diameter (mm)	3.75
Jet Reynolds number	10,000
Jet velocity ($\frac{m}{s}$)	296
$\frac{L_v}{D}$	180
Stoichiometric mixture fraction, ξ_{st}	0.028
Coflow velocity ($\frac{m}{s}$)	1.0
Coflow humidity ($\frac{kg-H_2O}{kg-air}$)	0.0072

The experimental setup consisted of a 0.55 m straight nozzle with an inner diameter of 3.75 mm and an outer diameter of 4.84 mm, centered at the exit of a 30 cm by 30 cm vertical wind tunnel. The coflow air stream from the wind tunnel had an average velocity of $1.0\frac{m}{s}$ ($\pm 0.06\frac{m}{s}$), temperature of $294K$ ($\pm 2K$), and an average humidity ratio of $0.0072\frac{kg}{kg_{air}}$. The complete data set included radial profiles at several streamwise locations of three different conditions for the H_2 flame: undiluted, 20% He dilution, and 40% He dilution. In this study, only the undiluted flame is investigated, to avoid the need to consider the differential diffusion of He . The temperature, Reynolds number, and average velocity of the fuel at the nozzle exit were $295K$ ($\pm 2K$), 10,000, and $296\frac{m}{s}$ ($\pm 1.5\%$), respectively. The approximate visible flame length was reported to be 180 nozzle diameters, while the stoichiometric flame length, where the centerline mean mixture fraction matches the stoichiometric mixture fraction of 0.028, was at the streamwise location 127 diameters downstream of the nozzle. The flame conditions are summarized in Table 6.1.

The mixture fraction reported in the experimental measurements was the Bilger's mixture fraction [88] given by

$$\xi_{blgr} = \frac{\frac{2(Y_C - Y_{C,o})}{M_C} + \frac{(Y_H - Y_{H,o})}{2M_H} + \frac{(Y_O - Y_{O,o})}{M_O}}{\frac{2(Y_{C,F} - Y_{C,o})}{M_C} + \frac{(Y_{H,F} - Y_{H,o})}{2M_H} + \frac{(Y_{O,F} - Y_{O,o})}{M_O}}. \quad (6.1)$$

The experimental data provided measurements for the mean Bilger's mixture fraction $\tilde{\xi}_{blgr}$

and its rms $\sqrt{\tilde{\xi}_{blgr}^{1/2}}$, and also presented scalars conditionally averaged on the Bilger’s mixture fraction sample space η_{blgr} . The mixture fraction described by Eq. 6.1 is a linear combination of the elemental mixture fractions ξ_H , ξ_C , and ξ_O defined by the Eq. 3.4. Bilger’s mixture fraction retains the stoichiometric value of the mixture fraction even with the presence of differential diffusion effects.

The experimental systematic uncertainties, affecting the accuracy of the mean scalar values, and standard deviations are given in Table 6.2 [86]. The estimates of the uncertainties were based on repeatability of Raman calibrations, changes in the Raman/Rayleigh laser characteristics during experiments, drift in the LIF dye laser wavelengths, and uncertainties in the fluorescence calibrations and corrections. The uncertainties were based on conditions close to the stoichiometric mixture fraction (approximately $0.5 < \xi/\xi_{st} < 2.0$). Barlow and Carter [38] suggested that uncertainties may be greater for very rich and for lean samples due to limitations in the calibration procedures.

Table 6.2: Estimates of experimental accuracy [86]

Scalar	Systematic Uncertainty	% rms
N ₂	±3 – 4%	3.8
H ₂ O	±3 – 4%	4.8
OH	±15%	7.5
T	±3%	2.5
ξ	±3 – 4%	5.1
NO	±15 – 20%	12.5

The experimental flame had been studied using CMC under various contexts. Smith *et al.* was the first to apply the CMC model, with equal diffusivity, to the flame in [89] and compared the CMC results with those obtained from the transported PDF model in [64]. Barlow *et al.* [84] examined radiation modelling with CMC. Fairweather and Woolley [85] used CMC modelling and compared results using different RANS turbulence modelling approaches (k - ϵ and RSM) and chemical mechanisms of varying complexity. As described in Section 3.4, Kronenburg and Bilger [61] studied differential diffusion effects using a CMC formulation different from the model used in the present study.

6.2 Computational Setup

This section provides the details of the computational setup used for the modelling of the turbulent hydrogen-air jet flame discussed in Section 6.1. The simulation details are con-

figured to replicate the experimental conditions as closely as possible. The computational grid, boundary, and initial conditions used are described.

6.2.1 Computational Domain, Boundary Conditions, and Initial Conditions

The computational domain, boundary conditions, and initial conditions are established to replicate the experimental set up as closely as possible with the known parameters and conditions. The computational domain is shown in Fig. 6.1. The domain is represented by a hexahedral two dimensional axisymmetric computational domain, such that all gradients in the azimuthal component are zero. The domain has a total length of 1.5 m in the axial direction (x) and a radius of 0.2 m, which is over twice the visible flame length from the experiment and approximately ten times the maximum flame width based on experimental data at the half-length of the flame. The fuel jet inlet extends over a radial distance (r) of 1.875 mm located at the base of the domain and starting from the centerline. An adiabatic wall of 0.545 mm separates the fuel and the air coflow streams. The air coflow inlet occupies the rest of the radial width at the base of the domain. An outlet is placed along the top boundary far downstream of the flame length which allows fluid to flow out of the domain without restriction. The outer side boundary is sufficiently far from the flame such that there is no impact on the flame structure, and specified as an opening allowing fluid to move through.

Dirichlet boundary conditions are set for the fuel and oxidizer inlets. A profile for the Favre averaged velocity, shown in Fig. 6.2, is specified for the fuel stream inlet with an average velocity of 296 m/s. The turbulent intensity at the inlet is 5%. Since the computation is two dimensional and axisymmetric, the azimuthal length spans 2π radians. Due to the low velocity of the air stream, a uniform velocity profile of 1 m/s is used for the oxidizer stream. The composition of the coflowing air is specified as $Y_{O_2} = 0.2303$, $Y_{N_2} = 0.7625$, and $Y_{H_2O} = 0.0072$, neglecting the small ($< 1\%$) amount of inert Argon (Ar) and the trace gases found in atmospheric air. The fuel and air temperatures are set to 293 K and atmospheric pressure is imposed. Zero gradient conditions are specified for the outer boundary on the air side.

The inlet conditional profiles are obtained from the SLFM, where the conditional profiles are obtained from a balance between chemistry and diffusion. The local mean scalar dissipation rate is $\tilde{\chi} = 0$, so that the conditional profiles are at equilibrium conditions. This provides the necessary boundary conditions for the CMC calculations, where the conditional profiles affect the advection terms for the CMC calculations. Zero gradient, or

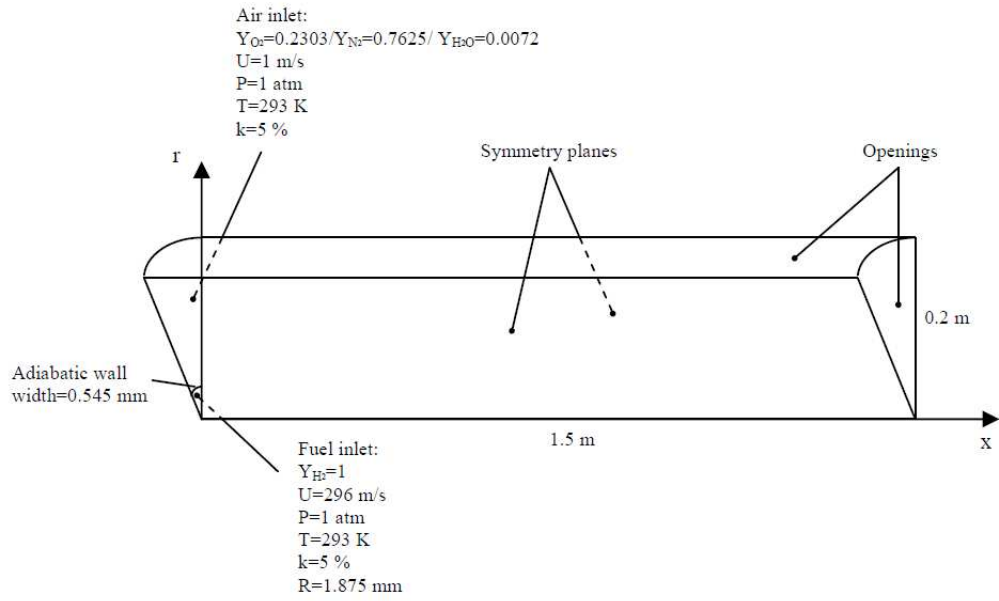


Figure 6.1: Computational domain and boundary conditions (not to scale)

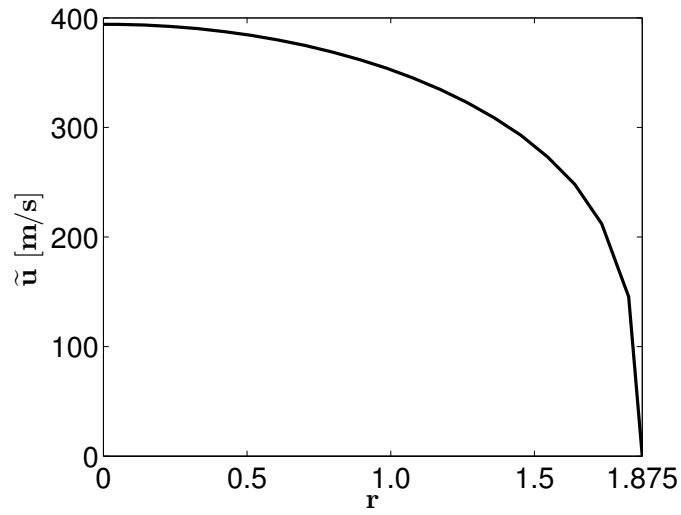


Figure 6.2: Specified inlet velocity profile

zero Neumann boundary conditions, are applied to the wall boundaries, such that

$$\frac{\partial Q}{\partial x_{\perp}} = 0, \quad (6.2)$$

where x_{\perp} is the component perpendicular to the boundary.

The computational domain is discretized into 380 cells and 160 cells in the axial and radial direction, respectively. A higher density of nodes is placed in the jet core and shear layer to better resolve the higher gradients in the flow and mixing fields. The distribution of spatial nodes is summarized in Table 6.3.

Table 6.3: Distribution of nodes in spatial grid

Axial Direction	
Range	Number of Nodes
0 - 0.003	10
0.003 - 0.04	70
0.04 - 0.09	70
0.09 - 0.7	50
0.7 - 1.5	20
Radial Direction	
0 - 0.001875	20
0.001875 - 0.00242	7
0.00242 - 0.0375	103
0.0375 - 0.075	20
0.075 - 0.2	10

The CMC spatial mesh is set to a one-to-one correspondance with the CFD mesh, so that the CMC equations are solved for each CFD cell. A coarser CMC grid can be selected due to reduced spatial dependence of the conditional averages, but is not investigated further due to tractable computational run times. The mixture fraction sample space is discretized into 115 nodes with a higher number of nodes between the values of 0 and 0.1. The distribution of nodes for the η grid is summarized in Table 6.4.

The mixture fraction grid is used for both the SLFM and CMC calculations. The extent of the mixture fraction grid refinement is large in order to take into account the fact that the stoichiometric value does not remain constant in the present differential diffusion CMC calculations. Additional details on the sensitive analysis on computational grid are presented in Section 6.3. Some previous CMC studies employed dynamic CMC spatial and

Table 6.4: Distribution of nodes in η grid

Range	Number of Nodes	Distribution
0 - 0.09794	50	uniform
0.09794 - 0.4197	50	uniform
0.4197 - 0.5037	8	uniform
0.5037 - 1	7	growth factor 1.64

mixture fraction grids which did not perform CMC calculations in nodes where chemical reactions were not expected to occur (very high and low mixture fractions) [80, 90]. However, since differential diffusion, which can occur even at mixture fractions without chemical reactions, is taken into account in the CMC calculations in this study, no restriction is placed on the CMC grid and all nodes are solved.

In the present CMC implementation, thirteen discretized governing equations are solved for the conditional species mass fractions (Eq. 5.10) and one transport equation for the conditional enthalpy (Eq. 5.12) for each mixture fraction and spatial node. The conditional mass fraction of the fourteenth species, N_2 , is obtained by conservation of mass at each η value of the grid. Non unity Lewis number are only included for H_2 , H , OH , and O , which possess the largest differences from the value of 1.

6.2.2 Turbulence Model

The mean flow transport equations are solved using a RANS approach (Section 2.2.2). Two additional equations, one for the turbulent kinetic energy and one for its dissipation, are solved using a $k - \varepsilon$ model. The $k - \varepsilon$ model with standard parameters had been widely reported to have trouble with accurately predicting axisymmetric jets [91]. With standard values for modelling constants, the radial spreading rate of the jet was largely overpredicted. A change to the $k - \varepsilon$ model parameters, most commonly $C_{\varepsilon 1}$ or $C_{\varepsilon 2}$, was often necessary to adequately predict the flow and mixing fields for specific configurations. Various attempts to improve predictions had been proposed such as the modification of $C_{\varepsilon 1}$ [92]. The aim of the modifications was to generate the effect of reducing the spreading rate. In previous studies, the selection of a constant was typically based on fitting to the centerline predictions. However, although spreading rates were reduced to provide good predictions near the centerline, the predictions were less satisfactory away from the centerline [84, 93]. In the present study, a modification of the $C_{\varepsilon 1}$ constant from the standard value of 1.44 to 1.7 is found to provide the best agreement between the radial profiles of the predicted mean mixture fraction (using Bilger's definition, Eq. 6.1) and its variance, and

the experimental values in the regions close to the stoichiometric mixture fraction, where NO formation is expected to be most prominent. Though the $k - \varepsilon$ model possesses the difficulties mentioned above, Fairweather and Woolley [85] found that the model produced superior predictions of the mixing field close to the nozzle, which is the region of interest in the current study, compared to the RSM approach. A sensitivity analysis for the $k-\varepsilon$ modifications is presented in Section 6.3 for different values of $C_{\varepsilon 1}$.

6.2.3 Temperature

Various sources provide thermodynamic properties as a power series. In the present study, the conditional temperatures are obtained from the conditional enthalpy values, such that

$$Q_h = a_0 + a_1 (Q_T - 298.15) + a_2 (Q_T - 298.15)^2, \quad (6.3)$$

where Q_h is the conditional enthalpy in $\frac{kJ}{kmol}$ and a_0 , a_1 , and a_2 are parameters tabulated in Table 6.5. The unconditional temperatures are obtained with the same method, with \tilde{h} and \tilde{T} replacing Q_h and Q_T , respectively in Eq. 6.3. The parameters in Table 6.5 were obtained by a second order polynomial curve fit of NASA data [94], which consisted of pinned polynomials for the ranges of $T \leq 1000K$ and $T \geq 1000K$. The thermodynamical data were obtained by simultaneous least squaring of C_P° , S_T° , and $H_T^\circ - H_{ref}^\circ$. Compared to only fitting C_P , this gave better reproducibility of the properties and lower deviation, with errors usually less than half of the previous method [95]. The temperature range of the polynomial fitting was between 300 to 5000 K, enough to cover the range of combustion of fuels.

6.2.4 Chemical Kinetics

The chemical source term is often the cause for the divergence of iterations in the system of stiff equations. In order to improve the effectiveness of the numerical solver, described in Section 5.5, Patankar [81] suggested the linearization of the chemical source term, into the form

$$\omega_{\eta,i} = S_{U,i} + S_{P,i}Q_i, \quad (6.4)$$

and from Eq. 4.48, the terms $S_{U,i}$ and $S_{P,i}$ can be expressed as

$$S_{U,i} = \frac{M_i}{\rho_\eta} \sum_{l=1}^L \left(\nu''_{i,l} k_{f,l} \prod_{j=1}^N [X_j|\eta]^{\nu'_{j,l}} - \nu'_{i,l} k_{r,l} \prod_{j=1}^N [X_j|\eta]^{\nu''_{j,l}} \right), \quad (6.5)$$

Table 6.5: Enthalpy coefficients

Species	a_0	a_1	a_2
O_2	-318.5359	31.9258	0.0017
H_2O	-241800.0	34.6674	0.0048
H_2	81.5507	28.0397	0.0018
H_2O_2	-136980.0	53.0956	0.0058
OH	39267.0	28.6722	0.0017
H	217860.0	20.3981	0.0001139
O	248880.0	21.0771	-0.0000883
HO_2	11834.0	40.9080	0.0042
N_2	-299.8299	30.2975	0.0016
N	471870.0	20.6962	0.00004856
NO	90710.0	31.6996	0.0014
HNO	105240.0	39.1926	0.0059
NO_2	33166.0	46.7331	0.0032
N_2O	80539.0	48.6296	0.0035

and

$$S_{U,i} = \frac{M_i}{\rho_\eta Q_i} \sum_{l=1}^L \left(\nu'_{i,l} k_{f,l} \prod_{j=1}^N [X_j | \eta]^{\nu'_{j,l}} - \nu''_{i,l} k_{r,l} \prod_{j=1}^N [X_j | \eta]^{\nu''_{j,l}} \right). \quad (6.6)$$

A chemistry mechanism is required for H , O , and N chemistry in order to obtain the rate constant k . The three parameters A , E , and n in Eq. 4.50 for the forward rate k_f are obtained from the chemical mechanism in Chen *et al.* [96]. The detailed hydrogen-nitrogen mechanism, shown in Table 6.6, consists of 48 elementary reactions involving 14 chemical species. For the reactions involving third bodies M , the third body efficiencies for species that are not specified has a value of 1.0. The reverse rate constant k_r is obtained using Eq. 4.51, where the equilibrium constant K_C is

$$K_C = K_P \left(\frac{P}{RT} \right)^{\sum_i \nu_i}, \quad (6.7)$$

and the equilibrium constant expressed in terms of partial pressure K_P is the ratio of $K_{P,i}$ for each reactants over the products. $K_{P,i}$ values for each species are obtained from JANAF tables, where they are tabulated for different temperatures.

Table 6.6: Hydrogen-nitrogen chemical mechanism

Reaction	A (cm,sec,K,mole)	n	E (cal/mole)
$H + O_2 \rightarrow OH + O$	2.00E14	0.0	16800.0
$OH + O \rightarrow H + O_2$	1.57E13	0.0	841.3
$O + H_2 \rightarrow OH + H$	5.06E4	2.67	6286.0
$OH + H \rightarrow O + H_2$	2.22E4	2.67	4371.0
$OH + H_2 \rightarrow H_2O + H$	1.00E8	1.60	3298.0
$H_2O + H \rightarrow OH + H_2$	4.31E8	1.60	18274.0
$2OH \rightarrow O + H_2O$	1.50E9	1.14	100.4
$O + H_2O \rightarrow 2OH$	1.47E10	1.14	16991.0
$O_2 + H + M \rightarrow HO_2 + M$	2.30E18	-0.80	0.0
$H_2O/6.5, H_2/1.0, O_2/0.4, N_2/0.4$			
$HO_2 + M \rightarrow O_2 + H + M$	3.19E18	-0.80	46699.3
$H_2O/6.5, H_2/1.0, O_2/0.4, N_2/0.4$			
$H + HO_2 \rightarrow 2OH$	1.50E14	0.00	1004.0
$H + HO_2 \rightarrow H_2 + O_2$	2.50E13	0.00	693.1
$OH + HO_2 \rightarrow H_2O + O_2$	6.00E13	0.00	0.0
$HO_2 + H \rightarrow H_2O + O$	3.00E13	0.00	1721.0
$HO_2 + O \rightarrow OH + O_2$	1.80E13	0.00	-406.3
$HO_2 + HO_2 \rightarrow H_2O_2 + O_2$	2.50E11	0.00	-1242.0
$OH + OH + M \rightarrow H_2O_2 + M$	3.25E22	-2.00	0.0
$H_2O/6.5, H_2/1.0, O_2/0.4, N_2/0.4$			
$H_2O_2 + M \rightarrow OH + OH + M$	1.69E24	-2.00	48348.0
$H_2O/6.5, H_2/1.0, O_2/0.4, N_2/0.4$			
$H_2O_2 + H \rightarrow H_2O + OH$	1.00E13	0.00	3585.0
$H_2O_2 + OH \rightarrow H_2O + HO_2$	5.40E12	0.00	1003.8
$H_2O + HO_2 \rightarrow H_2O_2 + OH$	1.80E13	0.00	32206.0
$H + H + M \rightarrow H_2 + M$	1.80E18	-1.00	0.0
$H_2O/6.5, H_2/1.0, O_2/0.4, N_2/0.4$			
$OH + H + M \rightarrow H_2O + M$	2.20E22	-2.00	0.0
$H_2O/6.5, H_2/1.0, O_2/0.4, N_2/0.4$			
$O + O + M \rightarrow O_2 + M$	2.90E17	-1.00	0.0
$H_2O/6.5, H_2/1.0, O_2/0.4, N_2/0.4$			
$H_2O_2 + H \rightarrow HO_2 + H_2$	4.79E13	0.00	7945.8
$HO_2 + H_2 \rightarrow H_2O_2 + H$	3.42E13	0.00	24134.8

Hydrogen-nitrogen chemical mechanism

Reaction	A (cm,sec,K,mole)	n	E (cal/mole)
$OH + O + M \rightarrow HO_2 + M$	1.00E16	0.00	0.0
$HO_2 \rightarrow OH + O$	1.41E19	-0.55	66580.0
$H_2 + O_2 \rightarrow OH + OH$	1.70E13	0.00	47780.0
$OH + OH \rightarrow H_2 + O_2$	5.89E11	0.00	29820.0
$H + O + M \rightarrow OH + M$	6.20E16	-0.60	0.0
$OH + M \rightarrow H + O + M$	3.22E17	-0.60	105548.6
$H_2O/6.5, H_2/1.0, O_2/0.4, N_2/1.0$			
$O + N_2 \rightarrow N + NO$	1.82E14	0.00	76210.0
$N + NO \rightarrow O + N_2$	1.01E14	-0.11	1330.0
$O + NO \rightarrow N + O_2$	3.80E9	1.00	41360.0
$N + O_2 \rightarrow O + NO$	3.64E10	0.92	9640.0
$H + NO \rightarrow N + OH$	2.63E14	0.00	50390.0
$N + OH \rightarrow H + NO$	6.88E12	0.31	1520.0
$NO + M \rightarrow N + O + M$	3.98E20	-1.50	149945.6
$N + O + M \rightarrow NO + M$	2.74E19	-1.50	-3519.9
$N_2 + M \rightarrow 2N + M$	3.72E21	-1.60	224850.3
$2N + M \rightarrow N_2 + M$	5.64E19	-1.60	-3854.5
$N_2O + O \rightarrow NO + NO$	6.92E13	0.00	26615.8
$NO + NO \rightarrow N_2O + O$	1.81E12	0.00	64625.7
$N_2O + O \rightarrow N_2 + O_2$	1.00E14	0.00	28006.2
$N_2 + O_2 \rightarrow N_2O + O$	5.66E13	0.00	109283.7
$N_2O + N \rightarrow N_2 + NO$	1.00E13	0.00	19862.1
$N_2 + NO \rightarrow N_2O + N$	1.19E12	0.00	133111.3
$N + HO_2 \rightarrow NO + OH$	1.00E13	0.00	1985.3
$NO + OH \rightarrow N + HO_2$	3.18E12	0.00	85277.9
$N_2O + H \rightarrow N_2 + OH$	7.60E13	0.00	15096.1
$N_2 + OH \rightarrow N_2O + H$	3.24E12	0.00	80428.4
$HNO + O \rightarrow NO + OH$	5.01E11	0.50	1985.3
$NO + OH \rightarrow HNO + O$	3.91E9	0.94	53960.0
$HNO + OH \rightarrow NO + H_2O$	1.26E12	0.50	1985.3
$NO + H_2O \rightarrow HNO + OH$	2.57E11	0.82	71130.0
$NO + HO_2 \rightarrow HNO + O_2$	2.00E11	0.00	1985.3
$HNO + O_2 \rightarrow NO + HO_2$	9.85E11	0.00	55.3

Hydrogen-nitrogen chemical mechanism

Reaction	A (cm,sec,K,mole)	n	E (cal/mole)
$HNO + HO_2 \rightarrow NO + H_2O_2$	3.16E11	0.50	1985.3
$NO + H_2O_2 \rightarrow HNO + HO_2$	3.90E11	0.50	36652.7
$HNO + H \rightarrow NO + H_2$	1.26E13	0.00	3972.9
$NO + H_2 \rightarrow HNO + H$	1.63E11	0.48	57760.0
$HNO + M \rightarrow H + NO + M$	1.78E16	0.00	48663.9
$H + NO + M \rightarrow HNO + M$	4.12E14	0.25	-1140.0
$HO_2 + NO \rightarrow NO_2 + OH$	2.11E12	0.00	-479.0
$NO_2 + OH \rightarrow HO_2 + NO$	2.43E13	-0.10	6340.0
$NO_2 + H \rightarrow NO + OH$	3.50E14	0.00	1500.0
$NO + OH \rightarrow NO_2 + H$	7.26E9	0.84	29890.0
$NO_2 + O \rightarrow NO + O_2$	1.00E13	0.00	600.0
$NO + O_2 \rightarrow NO_2 + O$	3.11E12	0.00	47505.2
$NO_2 + M \rightarrow NO + O + M$	1.10E16	0.00	66000.0
$NO + O + M \rightarrow NO_2 + M$	6.78E11	0.65	-7390.0

6.2.5 Radiative Heat Loss

The source term of the CMC enthalpy transport equation, with accounts for radiative heat loss (Eq. 4.52), requires the estimation of the Planck mean absorption coefficient $K_{P,i}$. For the hydrogen flame studied, the radiative losses are assumed to only be due to the energy loss from H₂O molecules. Barlow *et al.* [84] investigated various functional fits that had been proposed [75, 97, 98] for the Planck mean absorption coefficient of H₂O, K_{P,H_2O} . Barlow *et al.* found that the K_{P,H_2O} obtained from a curve fit of the results from the RADCAL code [98], performed best compared to other models of similar complexity. Following their findings, the RADCAL correlation is employed in this study, given by the expression

$$K_{P,H_2O} = \exp \left[278.713 - 153.24 \ln(T) + 32.1971 [\ln(T)]^2 - 3.0097 [\ln(T)]^3 + 0.104055 [\ln(T)]^4 \right], \quad (6.8)$$

where K_{P,H_2O} has units of $\frac{1}{m \cdot atm}$. The RADCAL curve of K_{P,H_2O} is shown in Fig. 6.3.

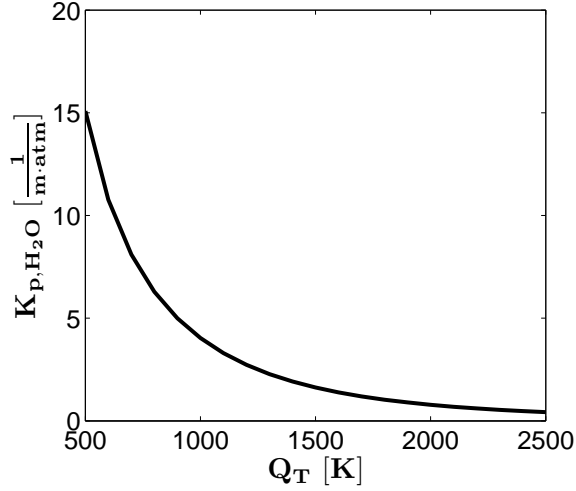


Figure 6.3: Planck mean absorption coefficient K_{p,H_2O}

6.2.6 Cross-stream averaging

Often in CMC studies where equal diffusivity is assumed, the solution is performed on radially averaged transport equations, reducing the dimensionality and computational time. The solution of radially averaged solution was suggested by Klimenko [28] by assuming that the radial dependence of the mixture fraction PDF was greater than the radial dependence of the conditional scalars, called the shear flow approximation. Kronenburg and Bilger [61] also performed calculations with cross-stream averaged CMC equations with differential diffusion modelling. In the present study, small radial dependence of the conditional scalars is not assumed and cross-stream averaging is not employed to the CMC equations, so that the effects of differential diffusion on radial dependence can be examined.

For the purpose of comparing the predictions with the experimental measurements [86], which presented cross-stream averaged conditional scalars, the conditional scalars obtained from the solution of the CMC equations are cross-stream averaged, as a post-process, at the specified axial locations, such that

$$Q_i^*(\eta) = \frac{\int_R \bar{\rho} Q_i \tilde{P}(\eta, r) r \partial r}{\int_R \bar{\rho} \tilde{P}(\eta, r) r \partial r}, \quad (6.9)$$

where the superscript * indicates cross-stream averaged quantities and R is the radius of the computational domain. Performing the procedure as a post-process allows comparison

of the results with the experimental data, without influencing the calculations with the additional assumption during the simulation.

6.3 Sensivity Analysis

Investigation of the sensivity of modelling parameters is crucial in reducing error and uncertainty in numerical methods. The highly dynamical nature of turbulence and combustion phenomena causes the outcomes to be highly susceptible to small variations in the conditions. In this section, the effects of varying the spatial grid, mixture fraction grid, and $k-\varepsilon$ parameter are discussed.

6.3.1 Grid Spacing

Three physical space grids, summarized in Table 6.7, are tested to examine the grid independence of the calculations. The distribution of nodes in all three grids exhibit a higher concentration closer to the nozzle and the near the centerline.

Table 6.7: Various spatial grids

Grid	Number of axial nodes	Number of radial nodes
1	120	80
2	380	160
3	420	200

The results, such as the axial profile of $\tilde{\xi}$ in Fig. 6.4 show noticeable differences in the change from grid 1 to grid 2. Differences between the results of grid 2 and 3 were sufficiently small $> 1\%$, therefore grid independance is achieved for grid 2. Grid 2 is chosen for performing subsequent calculations.

Two mixture fraction grids with 90 and 115 nodes are examined. For both grids, the distributions of nodes are concentrated at the lower values of η , in the region of the stoichiometric mixture fraction. The unconditional Favre averaged results show negligible change between the two mixture fraction grids. For the conditional profiles that are narrow, such as Q_{OH}^* , the resolution of the grid at the lower and higher end of the mixture fraction grid does not fully capture smooth profiles, resulting in profiles that are not smooth. However, since the mixture fraction PDFs for such locations are far from the peak values, the effect on the unconditional Favre averaged results are sufficiently small.

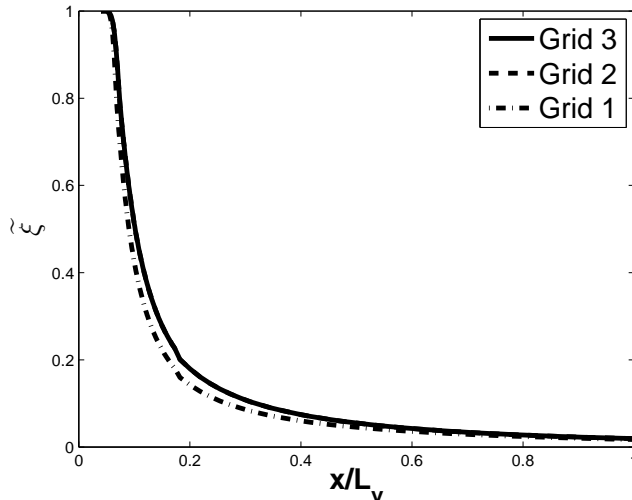


Figure 6.4: Axial Favre averaged mixture fraction profile with differential diffusion effects for various grids

6.3.2 Turbulence Modelling Constant

As discussed in Section 6.2.2, the parameters $C_{\varepsilon 1}$ and $C_{\varepsilon 2}$ are not universal, and are often adjusted for different fluid flow configurations. It is common that only one of the two parameters are modified at a time, therefore the adjustment of $C_{\varepsilon 1}$ is investigated. The following cases were tested: $C_{\varepsilon 1} = 1.6$, $C_{\varepsilon 1} = 1.7$, and $C_{\varepsilon 1}$ proposed by Morse [92] with the expression,

$$C_{\varepsilon 1} = 1.4 - 3.4 \left(\frac{k}{\varepsilon} \frac{\partial \tilde{u}}{\partial x} \right)_c^3, \quad (6.10)$$

where the subscript c indicates values at the centerline.

Figure 6.5 shows $\tilde{\xi}_{blgr}$ results with differential diffusion effects using the forementioned values of $C_{\varepsilon 1}$, at two axial locations. For all choices of $C_{\varepsilon 1}$, radial decay of $\tilde{\xi}_{blgr}$ is underpredicted. At $x/L_v = 1/8$, setting $C_{\varepsilon 1} = 1.6$ results in the closest results to the experimental measurements near the centerline. However, the $C_{\varepsilon 1} = 1.6$ profile has the largest difference from the measurements for $r/d > 2$, where chemical reactions occur. $C_{\varepsilon 1} = 1.7$ results in the best agreement for $r/d > 2$, though the centerline predictions are compromised. $\tilde{\xi}_{blgr}$ obtained using Eq. 6.10 for $C_{\varepsilon 1}$ lie between the values for $C_{\varepsilon 1} = 1.6$ and $C_{\varepsilon 1} = 1.7$. Downstream at $x/L_v = 1/2$, $\tilde{\xi}_{blgr}$ from Eq. 6.10 is the closest to measurements at the centerline,

while $C_{\varepsilon 1} = 1.6$ and $C_{\varepsilon 1} = 1.7$ results are lower and higher than the centerline value, respectively. However, the radial decay is underpredicted for all three cases, resulting in higher $\tilde{\xi}_{blgr}$ in the region of the reaction zone.

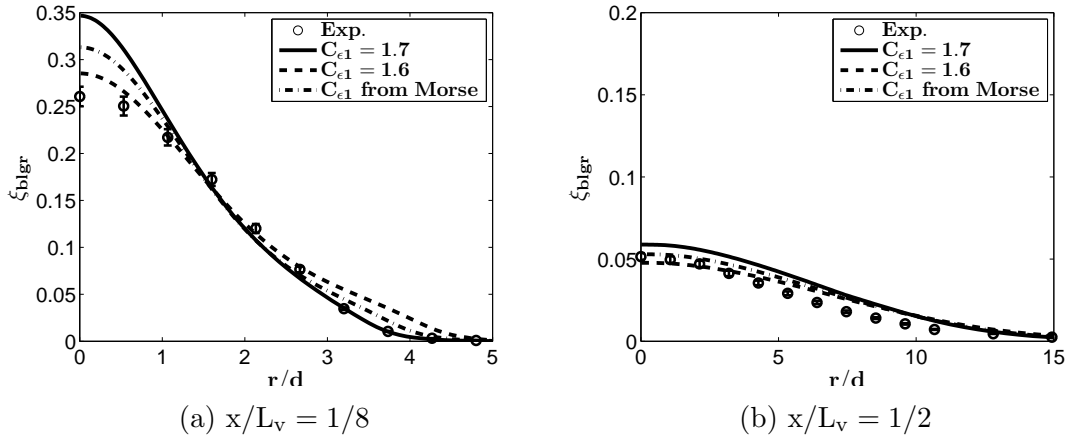


Figure 6.5: Radial profiles of Favre averaged Bilger's mixture fraction with differential diffusion effects for various $C_{\varepsilon,1}$

6.4 Velocity Field Results

The turbulent velocity field and mixing field are obtained with the aid of the k - ε model. k and ε modelling affect the calculation of \tilde{u} , $\tilde{\xi}$, and $\tilde{\xi}''^2$. In the present study, the main measures used to assess the CMC model are the predictions of scalar production, especially NO. Therefore, it is most important to obtain satisfactory mean mixture fraction predictions in the region where NO is generated. Most of the production and destruction of species scalars occur in the reaction zone, which corresponds to the region where the mean mixture fraction is close to the stoichiometric mixture fraction value. As discussed in Section 6.2.2, a value of $C_{\varepsilon 1} = 1.7$ is used in the results presented here, which provided the best predictions of mean mixture fraction and mixture fraction variance values close to the stoichiometric locations of the flame. The mean mixture fraction and variance results are discussed in following sections. In this section, the distributions of $\tilde{\mathbf{u}}$ and k are compared with the experimental measurements from [86]. The profiles at two axial locations are examined; at $x/L_v = 1/8$, where L_v is the visible flame length from [38] and differential diffusion effects are expected to have a noticeable impact, and at $x/L_v = 1/2$ where differential diffusion effects are expected to be diminished.

Figure 6.6 shows the radial profile of Favre averaged velocity \tilde{u} at the two chosen axial locations. At $x/L_v = 1/8$, overpredictions in \tilde{u} of approximately 40% are observed near the centerline, while underpredictions of up to 50% are found for radial distances between 1.5d and 3.5d. As shown in Fig. 6.6, at $x/L_v = 1/2$, \tilde{u} values are larger than the measurements by approximately 10%. Better estimates of \tilde{u} can be obtained with a different choice of $C_{\varepsilon 1}$, however the current value is chosen to obtain good predictions for the mean Bilger's mixture fraction ξ_{blgr} and mixture fraction variance ξ''^2 as discussed in Section 6.3.2.

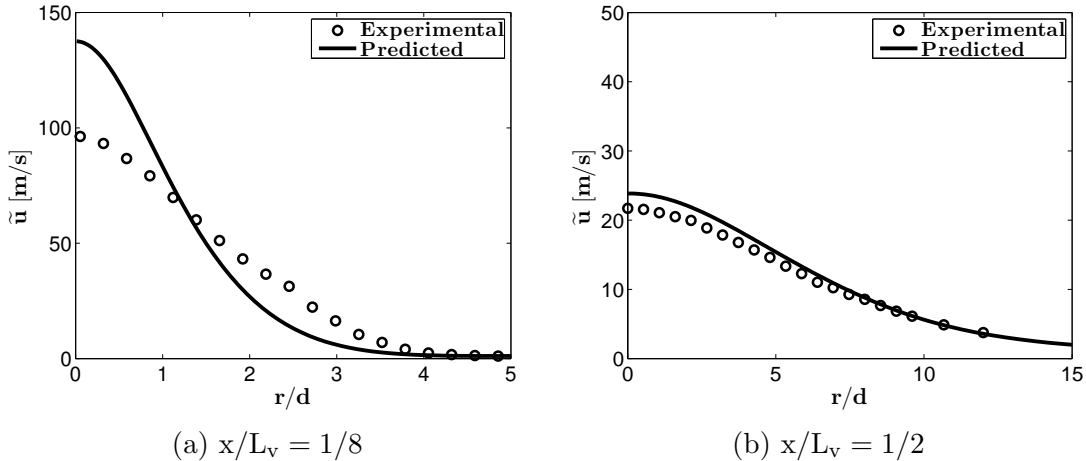


Figure 6.6: Predicted radial profiles of Favre averaged velocity. Experimental measurements are from the TNF library [86].

The mean turbulent kinetic energy distributions are shown in Fig. 6.7 alongside experimental data. The k profiles exhibit similar trends to the mean velocity profiles. At $x/L_v = 1/8$, k results are overpredicted near the centerline, while the values are underestimated for radial distances between 2.2d and 4d. The k profile is overpredicted at $x/L_v = 1/2$ for radial distances less than $r/d = 10$.

Though calculated mean turbulent energy dissipation rates are available, there are no experimental measurements of ε for comparison. The predicted ε results alone are not useful, so they are not presented here. However, numerous previous studies had found that the k - ε model has difficulties modelling the dissipation rate [91, 93]. It is likely that the inability to predict ε is the cause for the discrepancies in the k .

It is observed that differential diffusion has minimal effect on the velocity field. At $x/L_v = 1/8$, differences between \tilde{u} for equal and non-equal diffusivity calculations are insignificant, while at $x/L_v = 1/2$, a maximum increase of approximately 1% is observed. It

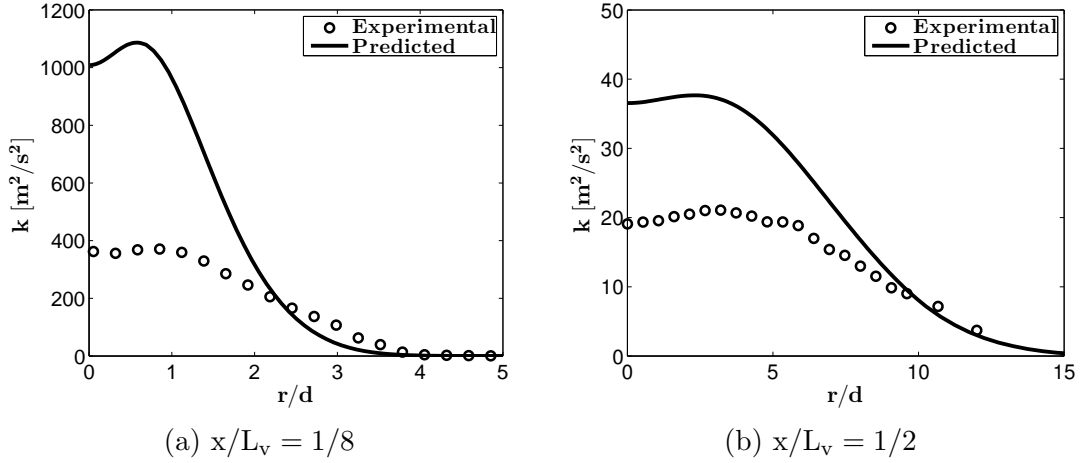


Figure 6.7: Predicted radial profiles of Favre averaged turbulent kinetic energy. Experimental measurements are from the TNF library [86].

can then be concluded that density changes from the temperature changes due to differential diffusion have small effect compared to the momentum of the flow.

6.5 Equal Diffusivity Results

This section focuses on the results of the calculations performed under the assumption of unity Lewis number. The mean mixing field quantities, unconditional scalars, and conditional scalars are presented. The equal diffusivity calculations are performed as a validation of previous studies [89, 84, 85] that have observed inadequacies in the modelling of the hydrogen flame due to the neglect of differential diffusion effects.

6.5.1 Mixing Field

Figure 6.8 shows radial profiles of the mean Bilger's mixture fraction $\widetilde{\xi}_{blgr}$ at the axial locations of interest. These profiles are obtained from Eq. 6.1 using local elemental compositions from the predicted Favre average species mass fractions to be discussed in Section 6.5.3. Though not explicitly shown here, it should be noted that the evolution of the conserved mixture fraction is unaffected by differential diffusion; in other words the plots of $\widetilde{\xi}$

and $\tilde{\xi}_{blgr}$ are equivalent under equal diffusivity assumptions. However, for consistency with the experimental data, $\tilde{\xi}_{blgr}$ results are presented in Fig. 6.8.

As can be seen in Fig. 6.8, the mean mixture fraction is overpredicted near the centreline by approximately 30 % at $x/L_v = 1/8$ and 5% at $x/L_v = 1/2$. At $x/L_v = 1/8$, farther away from the jet centreline, for radial distances between $1.5d$ and $3.5d$, $\tilde{\xi}_{blgr}$ values are lower than the measurements; at $r/d \approx 2.8d$, the underprediction reaches 37 %. In contrast, at $x/L_v = 1/2$, the mean mixture fraction remains overpredicted by 20% for most radial locations, except for $r/d > 12$. The overpredictions of the mean mixture fraction, were also observed in previous RANS studies of the same flame [84, 85]. The discrepancies between the calculated mixture fraction and the experimental data near the centreline are due to the difficulty in obtaining accurate radial decay of the mean mixture fraction with the $k-\varepsilon$ model. As such the value of $C_{\varepsilon 1}$ is chosen to take into account the lower radial decay in order to obtain good predictions near the stoichiometric mixture fraction. At this point, it may seem that the choice in the $C_{\varepsilon 1}$ is poor due to the underprediction of the mixture fraction at $x/L_v = 1/8$ in the region of the stoichiometric value, $r/d \approx 3.5$; however, it is shown in Section 6.6.2 that the underprediction is due to the assumption of equal species diffusivities. There is an additional justification for the current mixing field: the $\tilde{\xi}_{blgr}$ results at $x/L_v = 1/2$ shown in Fig. 6.8b, where differential diffusion are diminished, are significantly better than $\tilde{\xi}_{blgr}$ values for the same axial location obtained by Barlow *et al.* [84] where a different $C_{\varepsilon 1}$ was used and overpredictions up to 150% were observed.

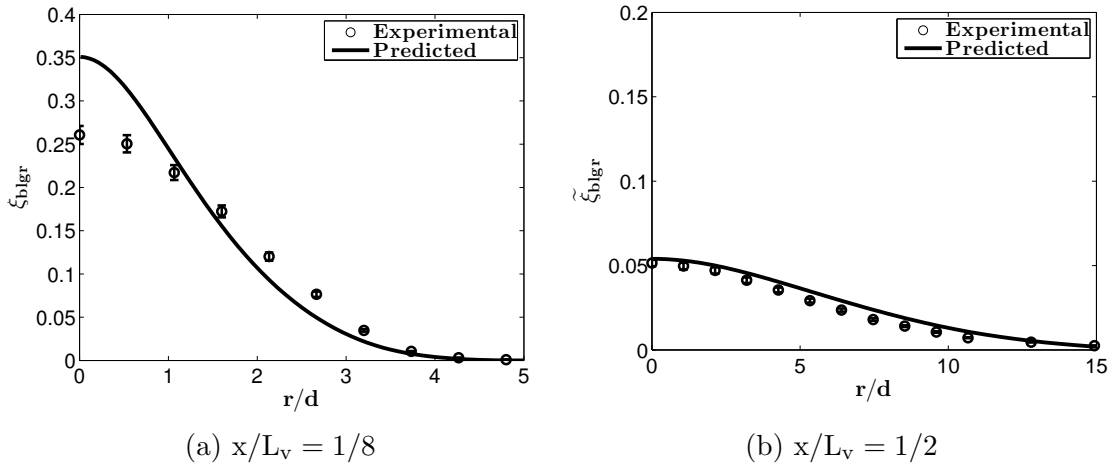


Figure 6.8: Predicted radial profiles of Favre averaged Bilger’s mixture fraction. Experimental measurements are from the TNF library [86].

It is not possible to calculate the variance of Bilger's mixture fraction $\widetilde{\xi_{blgr}''^2}$ without solving a transport equation, since there is no simple relationship such as Eq. 6.1 for $\widetilde{\xi}$. Without any further information, it is only possible to assume that the variance of the conserved mixture fraction $\widetilde{\xi''^2}$, which is solved with Eq. 2.62, and the variance of the Bilger's mixture fraction $\widetilde{\xi_{blgr}''^2}$, are equivalent. Figure 6.9 shows the radial profiles of the root mean square (rms) of mixture fraction, $\sqrt{\widetilde{\xi''^2}}$. At $x/L_v = 1/8$, the mixture fraction rms is overpredicted by a maximum of 30% for $r/d < 2$. At larger radial distances, $\sqrt{\widetilde{\xi''^2}}$ is in good agreement with the experimental data. The good agreement near the reaction zone suggests that the prediction of $\widetilde{\xi_{blgr}}$ in this region is valid and further justifies the choice of $C_{\varepsilon 1}$ to account for the inability of the $k-\varepsilon$ model to properly capture radial decay. Kronenburg and Bilger [61] showed similar overestimation of $\sqrt{\widetilde{\xi''^2}}$ at $x/L_v = 1/8$ near the centerline, though $\sqrt{\widetilde{\xi''^2}}$ away from the centerline was predicted to be approximately 10% higher than values presented in Fig. 6.9. At $x/L_v = 1/2$, $\sqrt{\widetilde{\xi''^2}}$ is well predicted for $r/d > 7$ and underpredicted by up to 10% for $r/d < 7$.

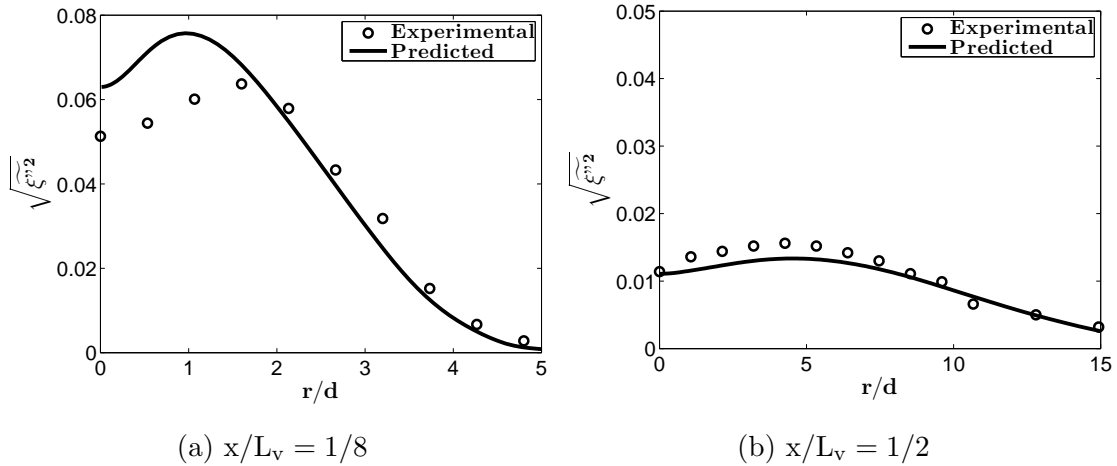


Figure 6.9: Predicted radial profiles of rms of Favre averaged mixture fraction variance. Experimental measurements are from the TNF library [86].

6.5.2 Conditional Scalars

Conditional mass fraction and temperature profiles obtained from CMC calculations under the unity Lewis number assumption are presented in this section. Since the conditional profiles from the experimental data are provided in terms of ξ_{blgr} , the calculated conditional profiles presented here are mapped to the sample space variable of Bilger's mixture fraction η_{blgr} using Eq. 6.1, though the CMC calculations are performed using the sample space variable of the conserved mixture fraction, η . However, as seen in Section 6.5.1, η_{blgr} values correspond to η under the assumption of unity Lewis number, such that there is no difference between the conditional profiles in the two sample spaces. The conditional profiles are cross-stream averaged using Eq. 6.9, so that comparisons can be made with the experimental data.

Figure 6.10 presents the conditional H_2 , O_2 , and H_2O mass fraction profiles at the two axial locations of interest. There are no estimates on the experimental uncertainties for H_2 and O_2 , but the calculated profiles of conditional mass fractions are in good agreement with the thel measurements at both locations. At $x/L_v = 1/8$, $Q_{H_2O}^*$ for $\eta_{blgr} > 0.03$ is lower than the experimental mean by 4%, lying on the lower range of the experimental uncertainty bounds. $Q_{H_2O}^*$ at $x/L_v = 1/2$ shows approximately 4% higher predictions than the measurement in the range of $0.015 < \eta_{blgr} < 0.035$, such that the results are on the upper end of the experimental uncertainty. Outside the range, the results are in good agreement with the experimental measurements.

The conditional N_2 mass fraction results, shown in Fig. 6.11, are in good agreement with the experimental data at both axial locations. Consistent with previous results [64, 84], the conditional temperatures are underpredicted by 200-300K in the region of $0.01 < \eta_{blgr} < 0.03$ at $x/L_v = 1/8$, outside of the uncertainty estimates. Q_T^* results are in better agreement with experiments farther downstream at $x/L_v = 1/2$, where the largest difference is found in the vicinity of $\eta_{blgr} = 0.022$, predicting temperatures approximately 50K higher than the experimental mean. Figure 6.12 presents the conditional OH mass fraction profiles at the two axial locations. At the first axial location, good agreement with experiments is found on the fuel rich side of the stoichiometric mixture fraction, $\eta_{blgr} > \eta_{blgr,st} = 0.028$. The artifact in the experimental data near $\eta_{blgr} = 0.052$, with an unexpected increase in Q_{OH}^* , is likely due to inaccuracies in the experimental measurement procedure. On the fuel lean side of the stoichiometric mixture fraction, Q_{OH}^* is lower than the experimental measurements. For $0.02 < \eta_{blgr} < 0.28$, the calculated values are still within experimental uncertainty, though the results are greatly underpredicted at the lower mixture fractions. At $x/L_v = 1/2$, CMC results are lower than the measurements throughout the range of η_{blgr} . In the vicinity of $\eta_{blgr,st}$, Q_{OH}^* is within the uncertainty estimates.

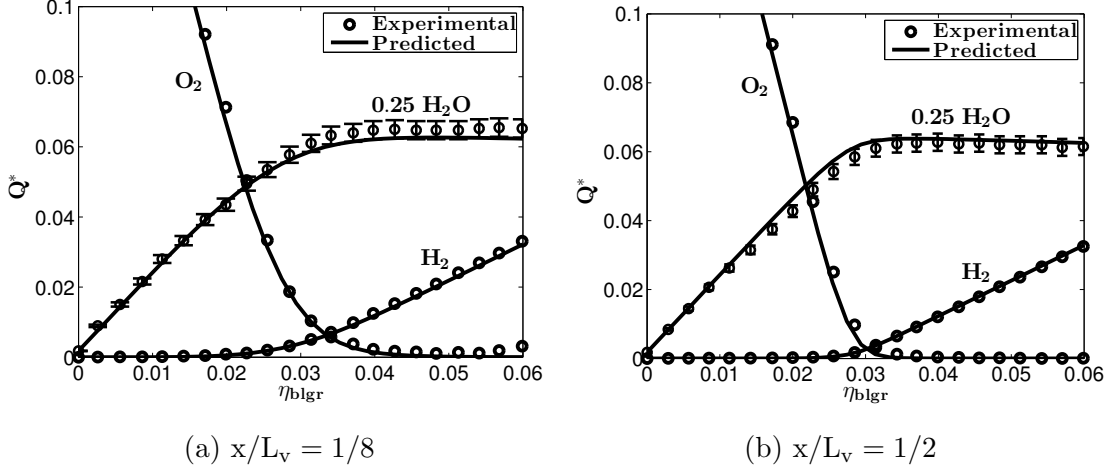


Figure 6.10: Predicted profile of conditional radially averaged H_2 , O_2 , and H_2O mass fraction with $Le_i = 1$. Experimental measurements with uncertainties taken from the TNF library [86].

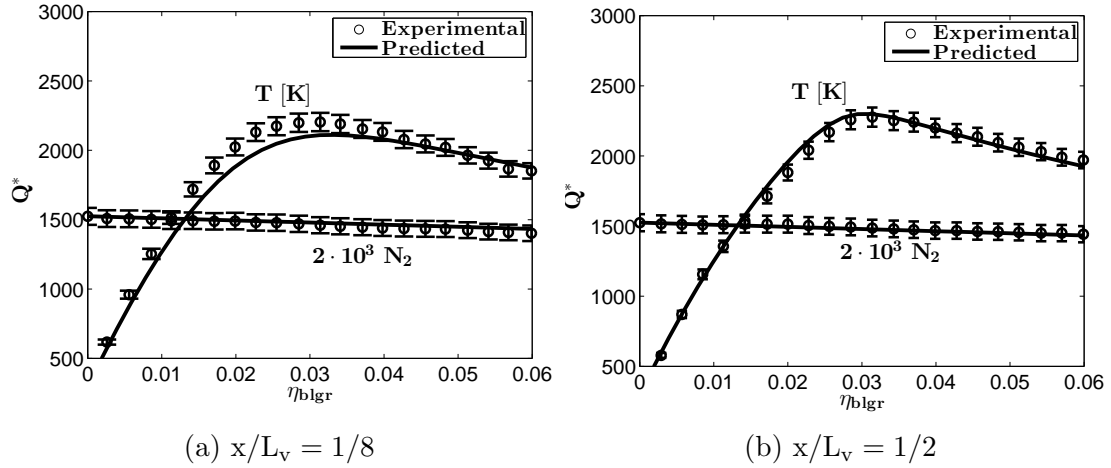


Figure 6.11: Predicted profile of conditional radially averaged N_2 mass fraction and temperature with $Le_i = 1$. Experimental measurements with uncertainties taken from the TNF library [86].

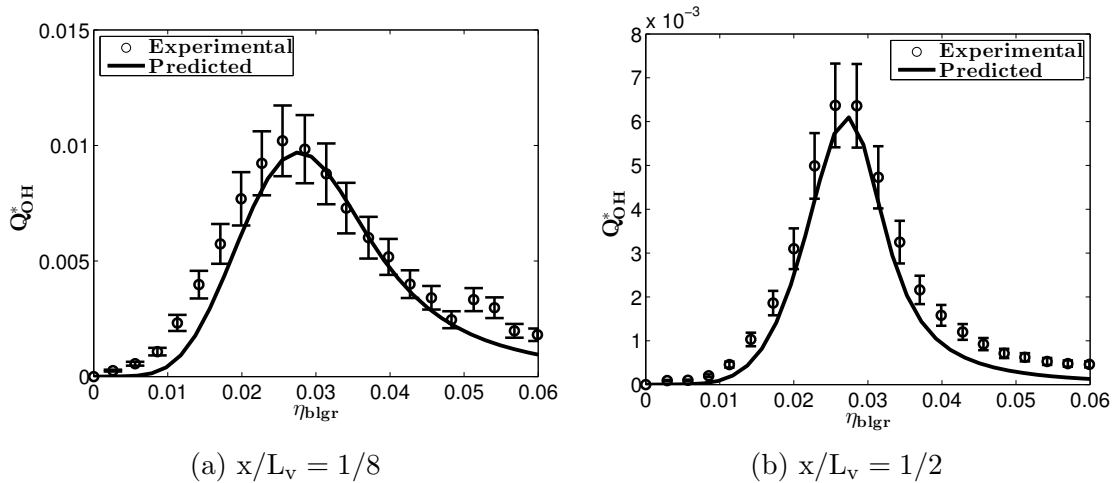


Figure 6.12: Predicted profile of conditional radially averaged OH mass fraction with $Le_i = 1$. Experimental measurements with uncertainties taken from the TNF library [86].

The conditional NO mass fraction results in Fig. 6.13 show the same trend found in other equal diffusivity CMC studies [64, 84, 85]. Q_{NO}^* close to the nozzle at $x/L_v = 1/8$ is significantly underpredicted, with the peak value being 60% lower than the experimental data. Advancing downstream, Q_{NO}^* becomes higher than experimental measurement, which was also observed in the aforementioned CMC studies. On the fuel rich side of stoichiometry, $\eta_{blgr} > 0.028$, Q_{NO}^* lies close to the upper edge of the uncertainty estimates, with values up to 20% higher than the experimental mean. For leaner mixture fractions, Q_{NO}^* is approximately 40% greater than the measurements.

The calculations of conditionally averaged quantities show good predictions for the major reactant species (H_2 , O_2 , and N_2). At the axial location close to the nozzle, lower values for the CMC results compared to the measurements are found for the product species (H_2O , OH , and NO). The discrepancies indicate underpredictions in the reaction rates, which are also signified by the lower temperatures. Farther downstream, the CMC results are generally in better agreement with the measurements.

6.5.3 Unconditional Mean Scalar Field

Favre averaged unconditional scalars predictions are obtained with Eq. 4.39, using the CMC results of Section 6.5.2 and the Favre averaged mixture fraction PDF based on the $\tilde{\xi}$ and $\tilde{\xi}''^2$ results of Section 6.5.1. Note that both definitions of the mixture fraction, ξ

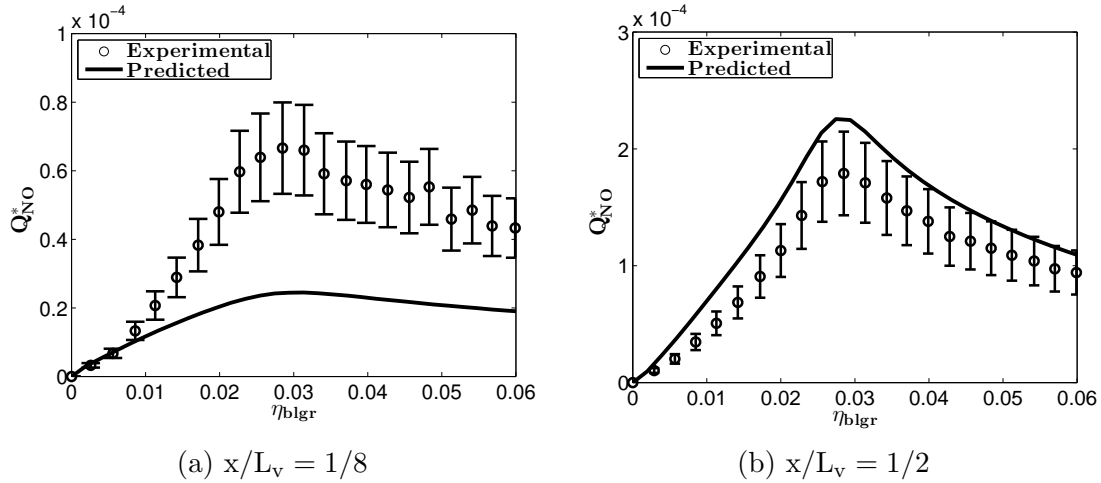


Figure 6.13: Predicted profile of conditional radially averaged NO mass fraction with $Le_i = 1$. Experimental measurements with uncertainties taken from the TNF library [86].

and ξ_{blgr} , can be used to calculate the unconditional scalars; however, the mixture fraction used for the conditional scalar and the PDF in Eq. 4.39 should be consistent.

The unconditional Favre averaged H_2 and H_2O mass fraction profiles are shown in Fig. 6.14. The \tilde{Y}_{H_2} results follow a similar trend to the $\tilde{\xi}_{blgr}$ profile, underpredicting the penetration of \tilde{Y}_{H_2} into the lean regions. An overprediction is found near the centreline by approximately 40% at $x/L_v = 1/8$. At the same axial location, farther away from the jet centreline, \tilde{Y}_{H_2} is underpredicted for radial distances between $1d$ and $3.5d$. In contrast, \tilde{Y}_{H_2} values are higher than the measurements by 10% for most radial locations at $x/L_v = 1/2$, except for $r/d > 6$. \tilde{Y}_{H_2O} production is generally underpredicted at $x/L_v = 1/8$, except in the vicinity of $r/d = 1.5$. At the centerline, \tilde{Y}_{H_2O} results are 18% lower than the measurements, while the peak value at $r/d \approx 2.7$ is underpredicted by approximately 10%. At $x/L_v = 1/2$, \tilde{Y}_{H_2O} values are higher than experimental measurements by up to approximately 30% for $r/d < 15$.

The unconditional Favre averaged O_2 and N_2 mass fraction profiles are presented in Fig. 6.15. \tilde{Y}_{O_2} is overpredicted at the first axial location for $2.5 < r/d < 4.25$, which may indicate lower determined reaction rates than measured. Conversely, \tilde{Y}_{O_2} values at the downstream location are lower than the experimental data for $r/d < 15$. \tilde{Y}_{N_2} results at $x/L_v = 1/8$ are higher than measurements by up to 10% for the range of $0.5 < r/d < 3.5$, outside of the uncertainty estimates; however, good agreement is found outside the range. Agreement with the experimental data is also observed at $x/L_v = 1/2$.

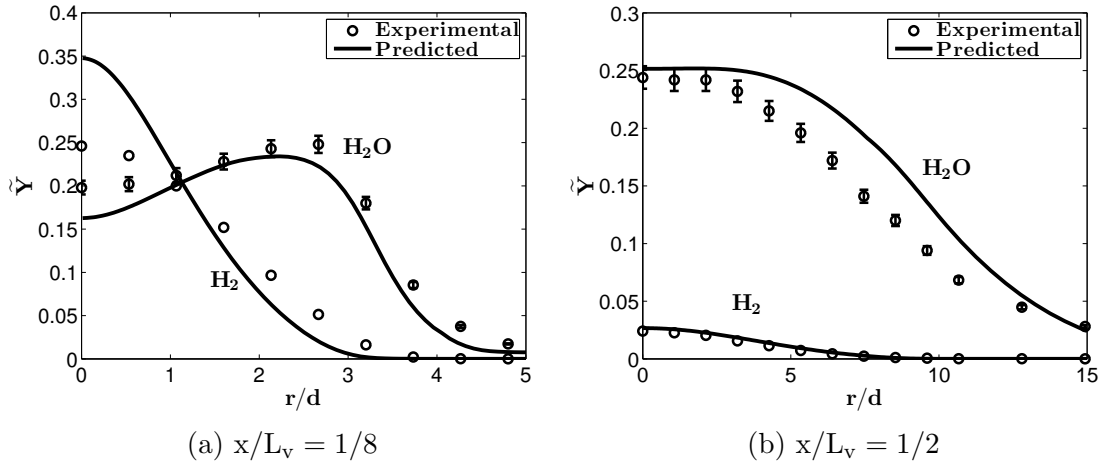


Figure 6.14: Predicted profile of unconditional Favre averaged H_2 and H_2O mass fraction with $Le_i = 1$. Experimental measurements with uncertainties taken from the TNF library [86].

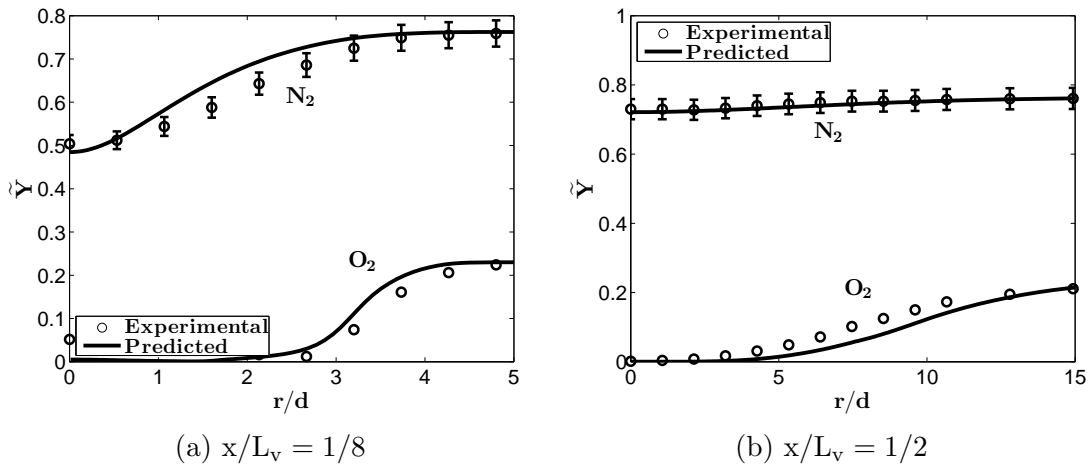


Figure 6.15: Predicted profile of unconditional Favre averaged O_2 and N_2 mass fraction with $Le_i = 1$. Experimental measurements with uncertainties taken from the TNF library [86].

Figure 6.16 shows the unconditional Favre averaged O_2 mass fraction predictions with equal diffusivity calculations. The calculated peak value of \tilde{Y}_{OH} close to the nozzle is 38% higher than the measured peak. However, the lack of data points around the region may not have properly captured the peak value in the measurements. In addition to the difference in the peak value, it is clear that the overall profile is shifted in the direction of the centerline. Though the conditional profile in Fig. 6.12 does not indicate the shift, the likely cause is due to lower penetration of $\tilde{\xi}_{blgr}$ outwards from the jet core in Fig. 6.8. At $x/L_v = 1/2$, the predicted peak value of \tilde{Y}_{OH} is close to the measured peak from the experiment data. However, \tilde{Y}_{OH} is lower than measurements on the fuel rich side of the peak, where the value at the centerline is 65% lower. On the lean side, \tilde{Y}_{OH} is higher than the experimental measurements by approximately 30%.

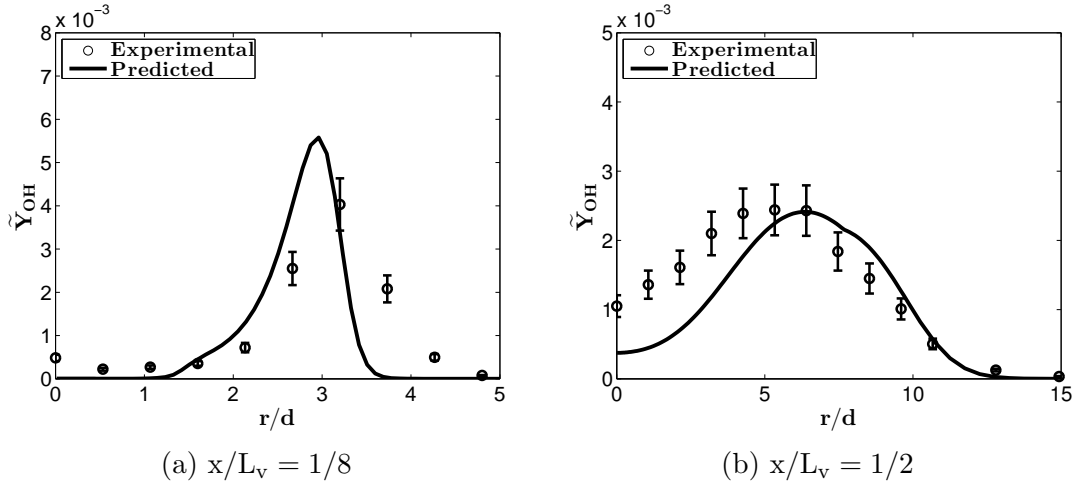


Figure 6.16: Predicted profile of unconditional Favre averaged OH mass fraction with $Le_i = 1$. Experimental measurements with uncertainties taken from the TNF library [86].

The unconditional Favre averaged NO mass fraction results are presented in Fig. 6.17. As expected from the results of $Q_{H_2O}^*$ in Fig. 6.13, \tilde{Y}_{NO} is largely underpredicted throughout the radial profile close to the nozzle at $x/L_v = 1/8$. The peak value of \tilde{Y}_{NO} is 56% lower than the measured value. The difference between calculated and measured values increases away from the peak, for both fuel rich and lean regions. Downstream at $x/L_v = 1/2$, calculated \tilde{Y}_{NO} is higher than the experimental measurements. Close to the centerline, predicted values lie on the upper edge of the uncertainty estimates, overpredicting the mean value by around 20%. Away from the centerline, \tilde{Y}_{NO} predictions are more than double the measurements.

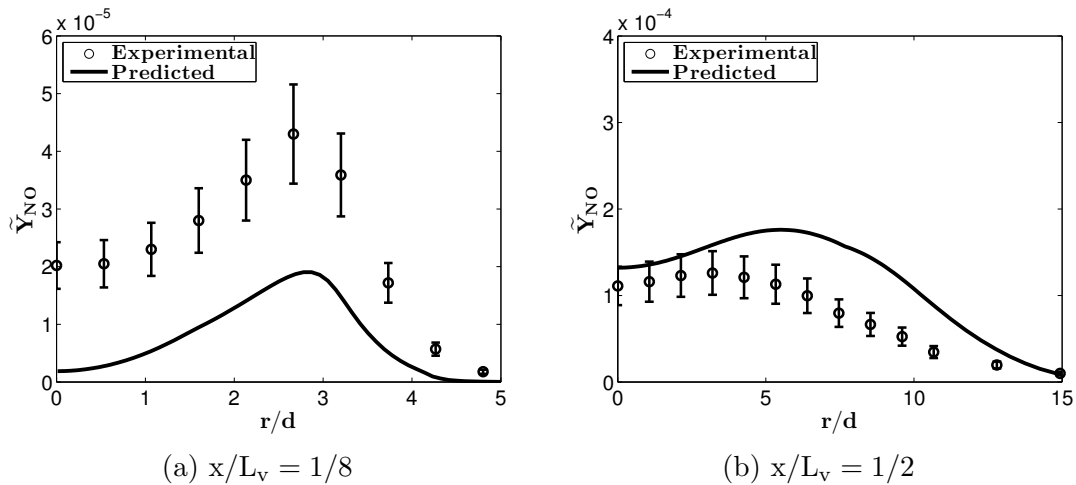


Figure 6.17: Predicted profile of unconditional Favre averaged NO mass fraction with $Le_i = 1$. Experimental measurements with uncertainties taken from the TNF library [86].

The unconditional Favre averaged temperatures are presented in Fig. 6.18. At $x/L_v = 1/8$, the peak temperature near $r/d = 2.9$ is calculated to be 150 K higher than the measurements, though the lack of data points around the peak again suggest that the peak may not be represented well. Away from the peak, temperatures are underpredicted by approximately 270 K near the centerline and 150 K for $r/d \approx 4.25$. At $x/L_v = 1/2$, the value of the peak temperature of approximately 2150 K is close to the measured value, though the locations differ. The measured peak temperature is found at $r/d \approx 2.1$ and the calculated peak at $r/d \approx 5$. There appears to be an overprediction in the spread outwards from the centerline, resulting in higher predictions than experiments for $r/d > 3.5$.

6.6 Differential Diffusivity Results

This section focuses on the modelling results of the hydrogen flame with differential diffusion effects included. The mean mixing field quantities, unconditional scalars, and conditional scalars are presented. Comparison is made between the differential diffusion results, the equal diffusivity calculations of Section 6.5, and the experimental measurements. Kronenburg and Bilger [61] reported some conditional scalars, and for those that are available, the trends observed in the present study are compared to the reported findings.

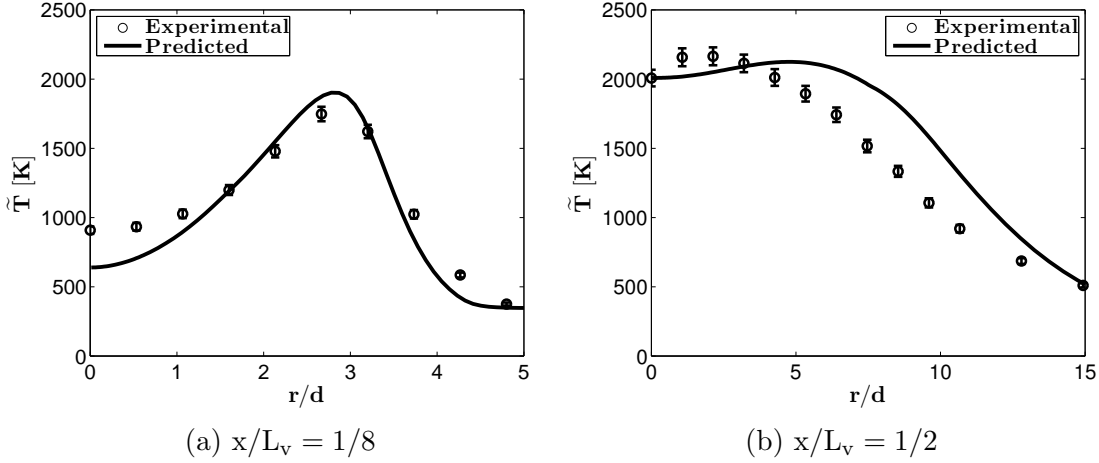


Figure 6.18: Predicted profile of unconditional Favre averaged temperature with $Le_i = 1$. Experimental measurements with uncertainties taken from the TNF library [86].

6.6.1 Conditional Scalars

The focus of this section is the presentation and comparison of conditional mass fraction profiles obtained from CMC calculations with differential diffusion effects. As described in Section 6.5.2, the conditional profiles are mapped to the sample space variable of Bilger’s mixture fraction η_{blgr} using Eq. 6.1 with the calculated local conditional species mass fraction, so that comparison with measurements can be made. An investigation of the results in conserved mixture fraction space ξ is found in Section 6.6.2. The conditional profiles presented in this section are cross-stream averaged using Eq. 6.9, so that comparison can be made with the experimental data. The radial dependence of the conditional scalars is examined in Section 6.6.3.

Figure 6.19 compares the cross-stream averaged conditional H_2 , O_2 , H_2O , and N_2 mass fraction profiles at $x/L_v = 1/8$ in η_{blgr} space in the cases of unity and non unity Lewis numbers. The profiles still show reasonable agreement with the experimental measurements for $Q_{H_2}^*$ and $Q_{O_2}^*$ when differential diffusion effects are included. In Fig. 6.19c, $Q_{H_2O}^*$ for $\eta_{blgr} > 0.035$ is increased from the equal diffusivity values by 4%, resulting in a close agreement with the experimental measurements. Conversely, $Q_{H_2O}^*$ is reduced for $\eta_{blgr} < 0.035$, with a decrease of approximately 4% around $\eta_{blgr} = 0.025$, so that the profile lies on the lower range of the experimental uncertainty bounds. The increased H_2O in the fuel rich regions is consistent with the observation in experiments described in Section 3.2. $Q_{N_2}^*$ is reduced when differential diffusion is considered, resulting in better agreement with the

experimental mean.

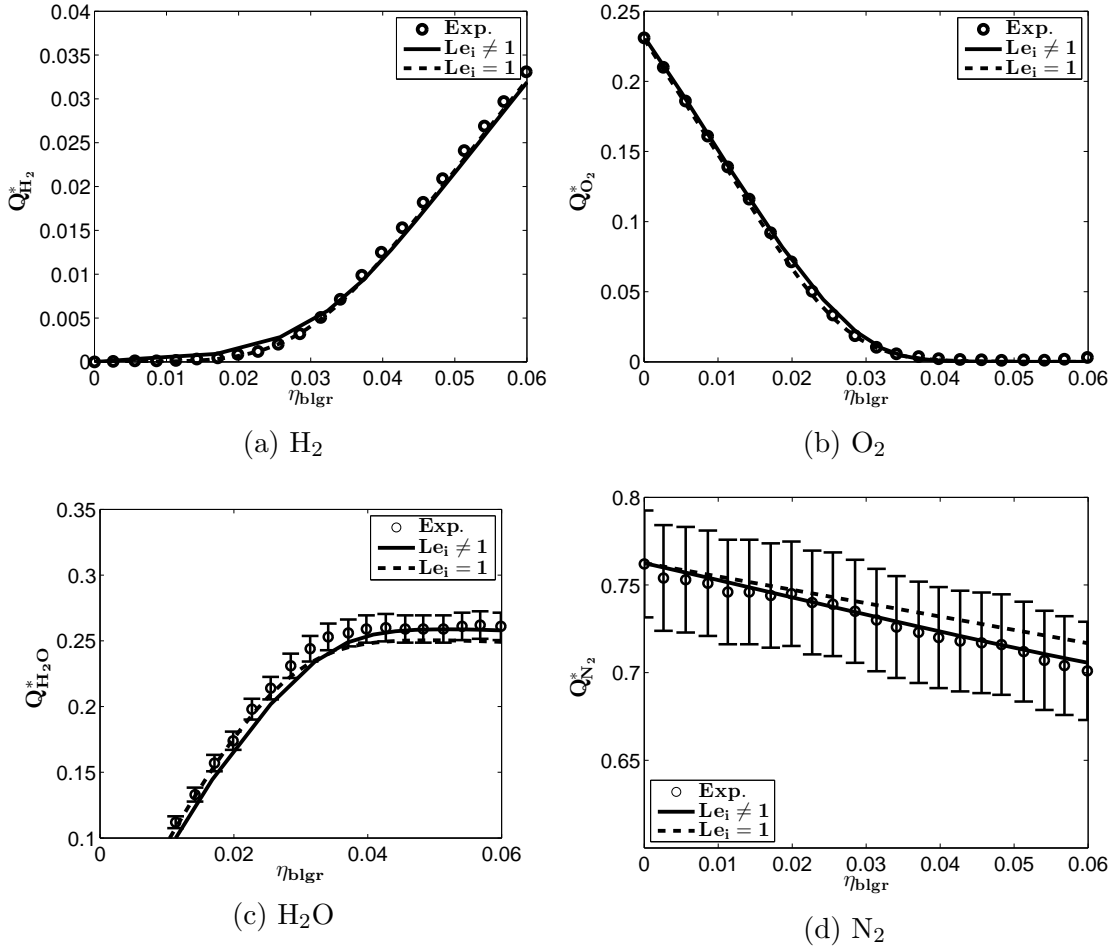


Figure 6.19: Predicted profiles of conditional means of major species mass fractions with differential diffusion effects at $x/L_v = 1/8$. Experimental measurements taken from the TNF library [86].

A comparison of cross-stream averaged conditional OH and NO mass fraction and temperature profiles at $x/L_v = 1/8$ is presented in Fig. 6.20. In comparison with the equal diffusivity diffusion values, the predicted Q_{OH}^* shown in Fig. 6.20a is increased for lean mixtures ($\eta_{blgr} < 0.02$), such that there is better agreement with the measurements and the values now lie within the uncertainty estimates. There is no significant change in Q_{OH}^* for $\eta_{blgr} > 0.02$, except near $\eta_{blgr} = 0.028$ where determined results are lower. It is suspected

that the cause of the lower peak is due to the resolution in the vicinity not capturing the peak OH due to cross-averaging and conversation to ξ_{blgr} , and will be further discussed in Section 6.6.3. Kronenburg and Bilger [61] also observed a similar increase Q_{OH}^* for the lean mixture fractions when differential diffusion was considered; however, it was also reported that an increase was found near the stoichiometric mixture fraction, whereas it is not present in the current results. Examining the conditional NO results in Fig. 6.20b, Q_{NO}^* is improved on the rich side of stoichiometry ($\eta_{blgr} > 0.028$) when differential diffusion is considered; an increase of approximately 40% for $\eta_{blgr} > 0.0375$ is obtained. However, Q_{NO}^* remains underpredicted compared to the experimental measurements. Additionally, Q_{NO}^* is decreased up to 10% on the lean side of the stoichiometric mixture fraction. The present findings are contrasted with those reported by Kronenburg and Bilger [61] where a higher increase of approximately 60% was observed. An increase in the conditional temperature is observed in Fig. 6.20c for mixture fraction values on the fuel rich side of the stoichiometric mixture fraction, $0.025 < \eta_{blgr} < 0.05$, when differential diffusion is included, with an increase in peak temperature of approximately 100 K. For fuel lean mixtures, $\eta_{blgr} < 0.025$, Q_T^* is lower by 100 K compared to the equal diffusivity results and remains underpredicted compared to the experimental results. The changes in Q_T^* considering differential diffusion effects are consistent with the trends observed for the conditional species mass fractions. The decreased temperatures for lower mixture fractions corresponds to the lower production of H₂O in Fig. 6.19 and NO in Fig. 6.20, whereas the higher temperatures for richer mixture fractions correspond to higher values of the same species.

Figure 6.21 shows the cross-stream averaged conditional H₂, O₂, H₂O, and NO mass fraction profiles farther downstream of the nozzle at $x/L_v = 1/2$. No significant changes are observed for $Q_{H_2}^*$ and $Q_{O_2}^*$ when differential diffusion effects are included. $Q_{H_2O}^*$ in the vicinity of $\eta_{blgr,st}$ are slightly lower, by approximately 2%, resulting in closer agreement with the experimental mean. Negligible changes are observed for $Q_{H_2O}^*$ away from $\eta_{blgr,st}$. A small decrease in Q_{NO}^* is found for $0.02 < \eta_{blgr} < 0.06$, though the results are still well within uncertainty estimates.

The cross-stream averaged conditional OH, NO mass fraction and temperature profiles at $x/L_v = 1/2$ are presented in Fig. 6.22. As shown in Fig. 6.22a, a larger increase in OH mass fractions compared to what is displayed in Fig. 6.20 is observed around $\eta_{blgr,st}$, with a change of 8% in the peak values, bringing Q_{OH}^* closer to the experimental mean. On the lean side, Q_{OH}^* is increased from the equal diffusivity value by 35% near $\eta_{blgr} = 0.02$, resulting in values at the upper bound of the uncertainty estimates. Conversely, Q_{OH}^* is decreased on the rich side near $\eta_{blgr} = 0.0375$, with differences of approximately 35% from the equal diffusivity values. Conditional NO mass fractions, as shown in Fig. 6.22b, are

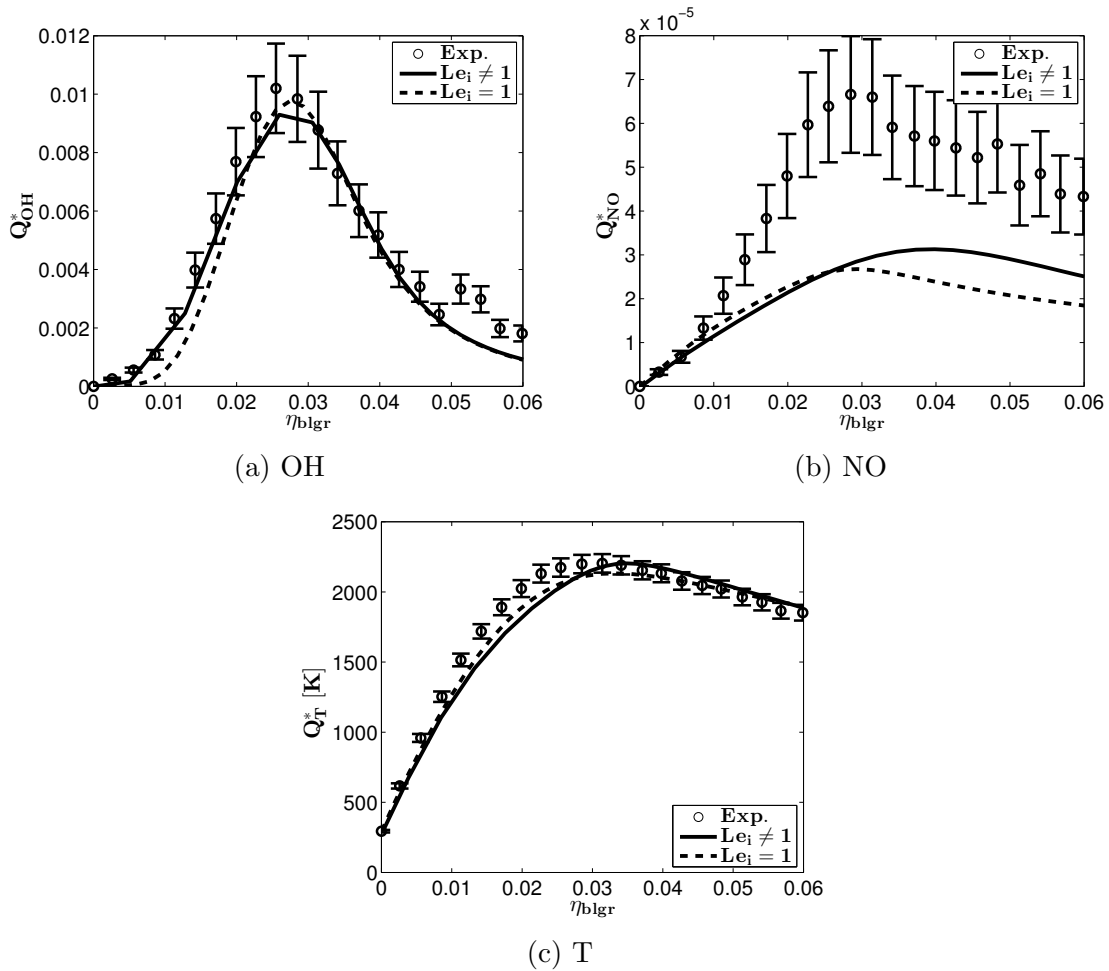


Figure 6.20: Predicted profiles of conditional means of minor species mass fraction and temperature with differential diffusion effects at $x/L_v = 1/8$. Experimental measurements taken from the TNF library [86].

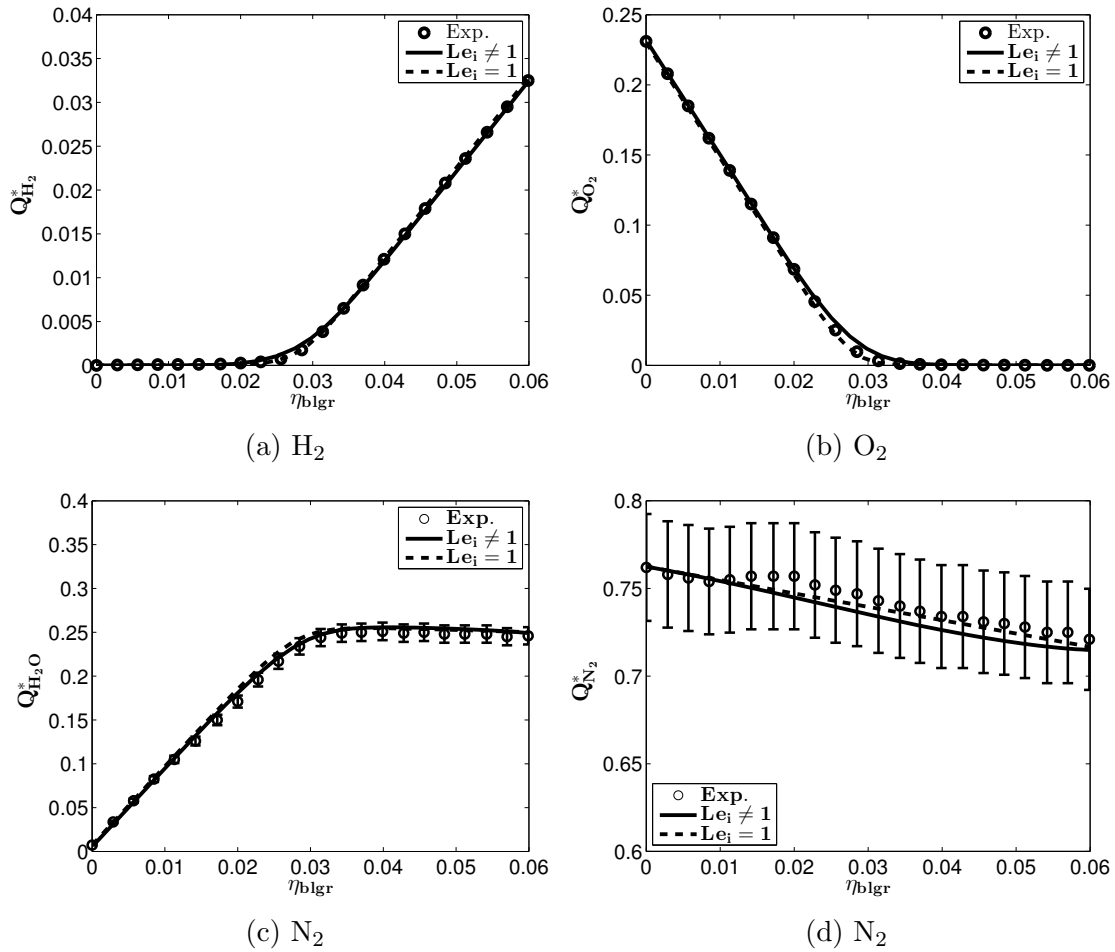


Figure 6.21: Predicted profiles of conditional means of major species mass fractions with differential diffusion effects at $x/L_v = 1/2$. Experimental measurements taken from the TNF library [86].

increased by up to 5% for $\eta_{blgr} > 0.03$. As expected at this axial location, only small changes in the predictions are observed when differential diffusion is included. The changes at the downstream location may be due to the history effect described by Pitsch [35] which is discussed in Section 3.4. As shown in Fig. 6.22c, there is a decrease in Q_T^* of approximately 20 K for $0.02 < \eta_{blgr} < 0.03$ when differential diffusion effects are included, and negligible change outside of the range.

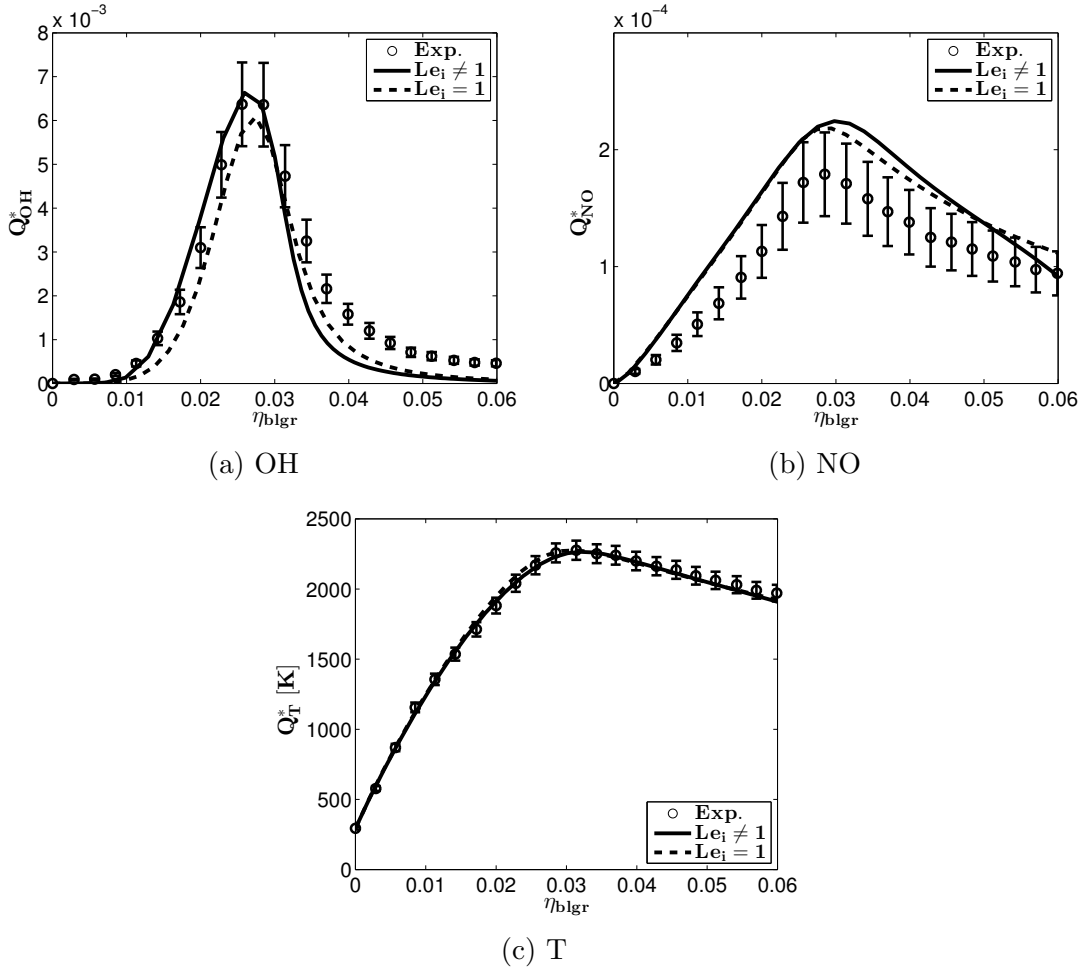


Figure 6.22: Predicted profiles of conditional means of minor species mass fraction and temperature with differential diffusion effects at $x/L_v = 1/2$. Experimental measurements taken from the TNF library [86].

The conditionally averaged scalars from the CMC calculations with differential diffusion

effects in general show improvement near the nozzle when comparing to equal diffusivity calculations. Particularly promising is the increase in conditional NO mass fractions. Farther downstream, the conditional scalars show the expected diminished effects of differential diffusion.

6.6.2 Mean Mixing and Unconditional Scalar Field

This section presents and compares the unconditional Favre averaged mixture fraction, chemical species, and temperatures results including differential diffusion effects to equal diffusivity calculations and experimental measurements. The profiles of $\tilde{\xi}_{blgr}$, shown in Fig. 6.23, are obtained from the local species concentration predictions using Eq. 6.1 and the effects of differential diffusion are clearly seen. At $x/L_v = 1/8$, the influence of differential diffusion on $\tilde{\xi}_{blgr}$ is greater diffusion towards the lower values $\tilde{\xi}_{blgr}$. The largest differences between $\tilde{\xi}$ and $\tilde{\xi}_{blgr}$ occur for radial distances between $1.5d$ and $3.5d$. In comparison with $\tilde{\xi}$, $\tilde{\xi}_{blgr}$ is lower for $r/d < 1$ (approximately 3% near the centerline), and larger by up to 40% for $1.5 < r/d < 4$. This is explained by the fact that diffusion of H_2 and H occurs from fuel rich to lean regions. As can be seen in Fig. 6.23, $\tilde{\xi}_{blgr}$ is in better agreement with the experimental values for $r/d > 1$, locations where significant reaction rates are expected to occur. It can be seen that the $C_{\varepsilon 1}$ value used is justified for the good agreement near the reaction zone, though the sacrifice of accuracy in predictions near the centerline in favour of predictions near stoichiometry is unavoidable. Though better predictions of radial decay can be obtained using more rigorous turbulence models, the additional computational demand of these models is a major consideration, and an intensive study of turbulence models is outside the scope of the present study. At $x/L_v = 1/2$, the values of $\tilde{\xi}_{blgr}$ are larger than those for $\tilde{\xi}$ for most radial locations, with the largest increase of 10% occurring near the centerline. Overall, the two mixture fraction profiles are closer to each other farther downstream where differential diffusion diminishes. The radial locations where $\tilde{\xi}_{blgr}$ corresponds to the stoichiometric value of 0.028, are shifted towards the leaner regions, resulting in new locations of $3.5d$ for $x/L_v = 1/8$ and $7.4d$ for $x/L_v = 1/2$.

Similar to the equal diffusivity results in Section 6.5.3. Favre averaged unconditional scalars predictions are determined with Eq. 4.39, using the CMC results of Section 6.6.1 and Favre averaged mixture fraction PDF based on the $\tilde{\xi}$ and $\tilde{\xi}''^2$ results.

Figure 6.24 shows the unconditional Favre averaged radial profiles of H_2 , O_2 , H_2O , and N_2 mass fraction at $x/L_v = 1/8$, in the cases of equal diffusivity assumption and differential diffusivity. Following the trend observed for $\tilde{\xi}_{blgr}$, \tilde{Y}_{H_2} , shown in Fig. 6.24a, is increased for $1 < r/d < 3.5$ due to an increase in the rate of diffusion from the higher concentrations

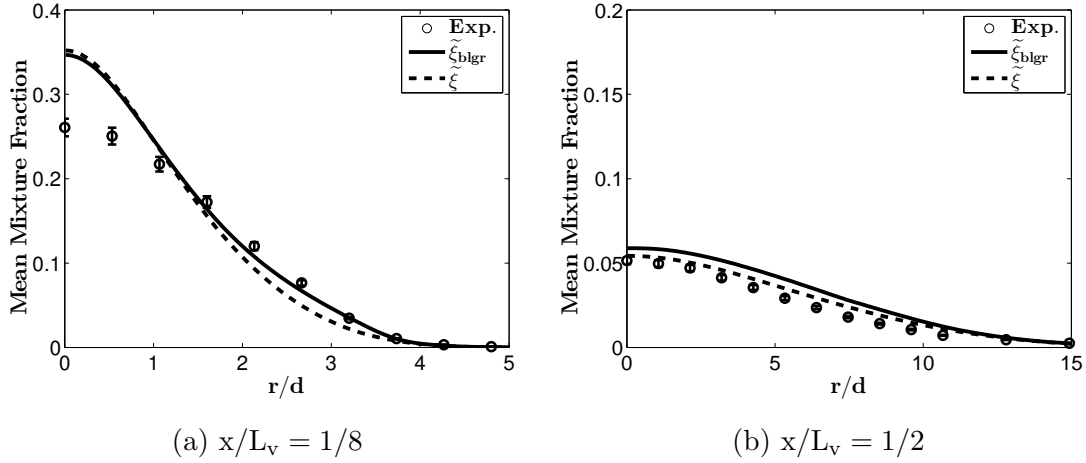


Figure 6.23: Predicted radial profiles of Favre averaged Bilger's mixture fraction with differential diffusion. Experimental measurements are from the TNF library [86].

in the jet core, resulting in better agreement with the experimental data. \tilde{Y}_{H_2} is decreased near the centerline, but not sufficiently, and predictions are still overpredicted both with and without differential diffusion due to the overprediction of $\tilde{\xi}_{blgr}$. The increase of H_2 penetration to the leaner regions results in a shift of the reaction zone outwards, as well as increased reaction rates. In Fig. 6.24b, \tilde{Y}_{O_2} for $r/d < 3.8$ is shifted to the right, resulting in a decrease of \tilde{Y}_{O_2} and better agreement with the experimental measurements. On the lean side of the reaction zone, \tilde{Y}_{O_2} is unaffected, since H_2 is not present and has no effect on \tilde{Y}_{O_2} in this region. In the experimental data, higher \tilde{Y}_{O_2} is observed in the fuel-rich region, which seems unrealistic. Barlow [86] noted that the inconsistency may be due to imperfect correction for the crosstalk of H_2 rotational Raman scattering onto the O_2 detector, therefore the difference between the calculated results and the measurement for this region is assumed to be due to an artifact in the experiment. The \tilde{Y}_{H_2O} profile in Fig. 6.24c shows an increase for $2 < r/d < 4$, corresponding to the rise in $Q_{H_2O}^*$ in Fig. 6.19c on the rich side of the stoichiometric value of mixture fraction. The higher mean H_2O mass fraction predictions lead to a better agreement with the experimental measurements. The increase of H_2O production can be related to the increased reaction rate due to greater fuel diffusion rates towards the reaction zone. Similar to the effect of H_2 penetration on \tilde{Y}_{O_2} , Fig. 6.24d shows a shift in \tilde{Y}_{N_2} for $1 < r/d < 3.8$ toward the fuel lean region, resulting in a decrease of \tilde{Y}_{N_2} and closer agreement with the experimental measurements, especially in the regions closer to the reaction zone.

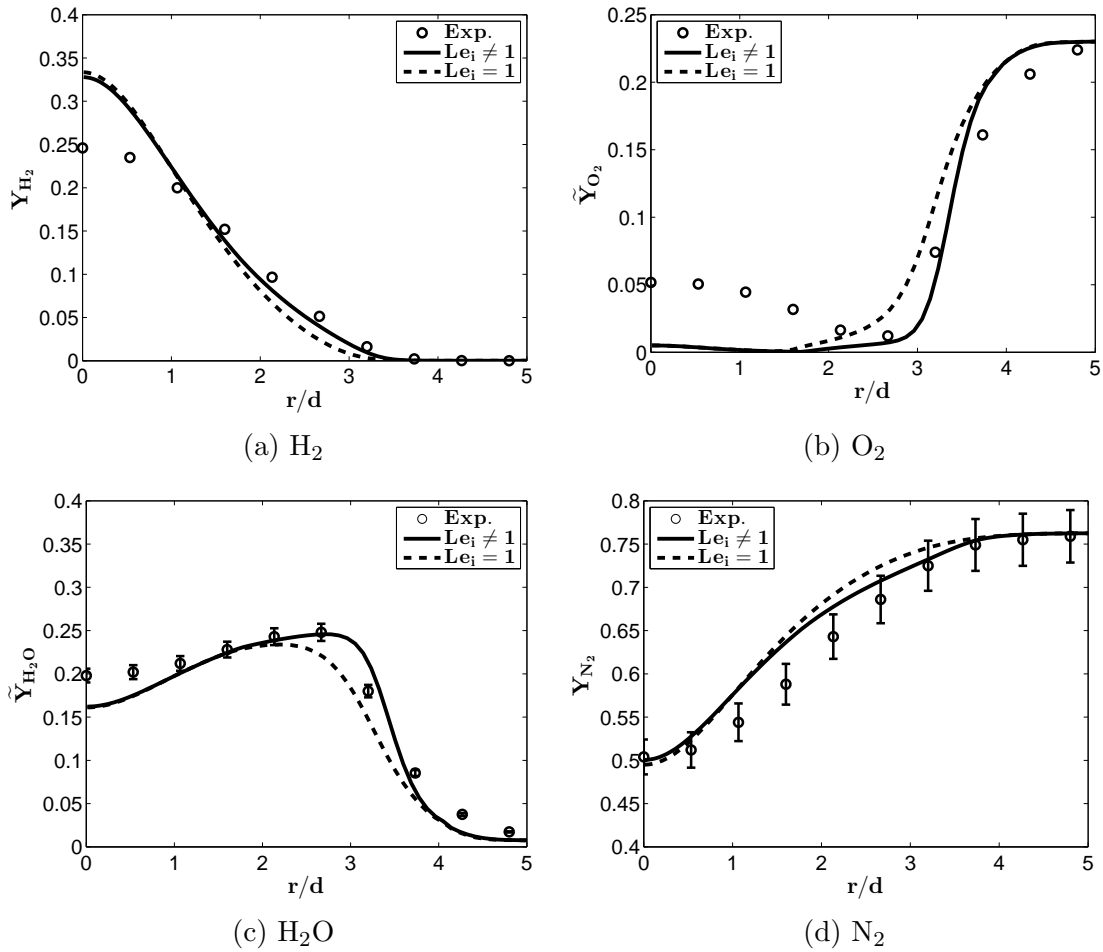


Figure 6.24: Predicted radial profiles of Favre averaged major species mass fraction with differential diffusion effects at $x/L_v = 1/8$. Experimental measurements are from the TNF library [86].

The unconditional Favre averaged radial profiles of OH, NO mass fraction and temperature at $x/L_v = 1/8$ are presented in Fig. 6.25. The adjustment in the location of the reaction zone from the increased penetration of H_2 can be clearly seen in the \tilde{Y}_{OH} profile in Fig. 6.25a, where the peak value is changed from $r/d \approx 2.95$ to $r/d \approx 3.25$. However, the peak value is overpredicted by approximately 60% compared to experimental results due to an increase of 25% compared to the equal diffusivity case. Away from the peak, \tilde{Y}_{OH} is largely lower than the experimental measurements. It appears that the spreading rate of \tilde{Y}_{OH} is underpredicted, resulting in an accumulation of OH near the reaction zone. In Fig. 6.25b, \tilde{Y}_{NO} is increased for $2.5 < r/d < 3.75$ when differential diffusion effects are included. The peak \tilde{Y}_{NO} value is raised by 31%. However, \tilde{Y}_{NO} remains underpredicted by approximately 30% at $r/d \approx 3$. Away from the reaction zone, differences between differential and equal diffusivity calculations are negligible. With differential diffusivity effects, the peak of \tilde{Y}_T , shown in Fig. 6.25c, shifts away from the centerline by a distance of approximately $0.3d$ and the peak temperature is increased by 10%. Physically, the rise in temperature can be explained by an increase in reaction rates due to the higher H_2 diffusion rate towards the reaction zone compared to the rate of heat diffusion away from the region. Again, negligible changes were observed away from the reaction zone for rich and lean regions. \tilde{Y}_T is underpredicted at $r/d \approx 4.5$ where $\tilde{\xi}_{blr}$ is lower than stoichiometric values. A possible cause is the underprediction of heat diffusion away from the reaction zone due to the assumption of $\alpha = D_\xi$, resulting in lower spreading of the temperature profile.

Farther downstream, the unconditional Favre averaged radial profiles of H_2 , O_2 , H_2O , and NO mass fraction at $x/L_v = 1/2$ are presented in Fig. 6.26. Some differences can be clearly seen in the radial profiles between differential and equal diffusivity results, and are larger than those observed for the conditional profiles in Fig. 6.21. With differential diffusion, \tilde{Y}_{H_2} is larger by approximately 20% near the centerline compared to the equal diffusivity results. \tilde{Y}_{O_2} exhibits the same trend as the results close to nozzle, with a decrease in predictions for $r/d < 13$. Around $r/d = 7$, \tilde{Y}_{H_2O} is increased by approximately 15%. In contrast, \tilde{Y}_{N_2} predictions with differential diffusivity are not significantly changed from equal diffusivity results.

Changes from the equal diffusivity calculations are also observed for the unconditional Favre averaged radial profiles of OH, NO mass fraction, and temperature shown in Fig. 6.27. The effects of differential diffusion on the locations of peak \tilde{Y}_{OH} , \tilde{Y}_{NO} , and \tilde{T} at $x/L_v = 1/8$ are also found at $x/L_v = 1/2$, where the peaks have moved outwards by $1.5d$. An increase of 20% is seen in the peak of \tilde{Y}_{OH} and 3% in the the peak of \tilde{Y}_{NO} . \tilde{T} is increased by approximately 200 K in the vicinity of $r/d = 7$.

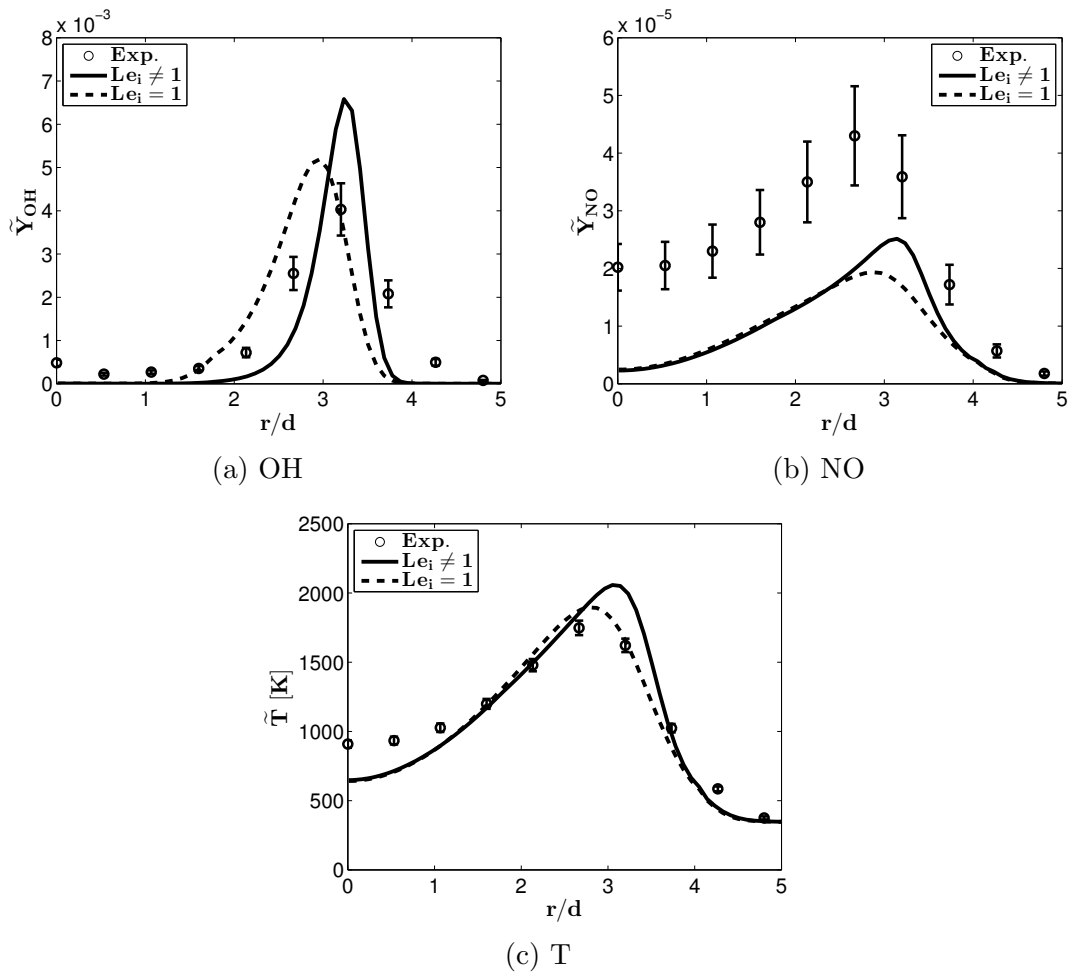


Figure 6.25: Predicted radial profiles of Favre averaged minor species mass fraction and temperature with differential diffusion effects at $x/L_v = 1/8$. Experimental measurements are from the TNF library [86].

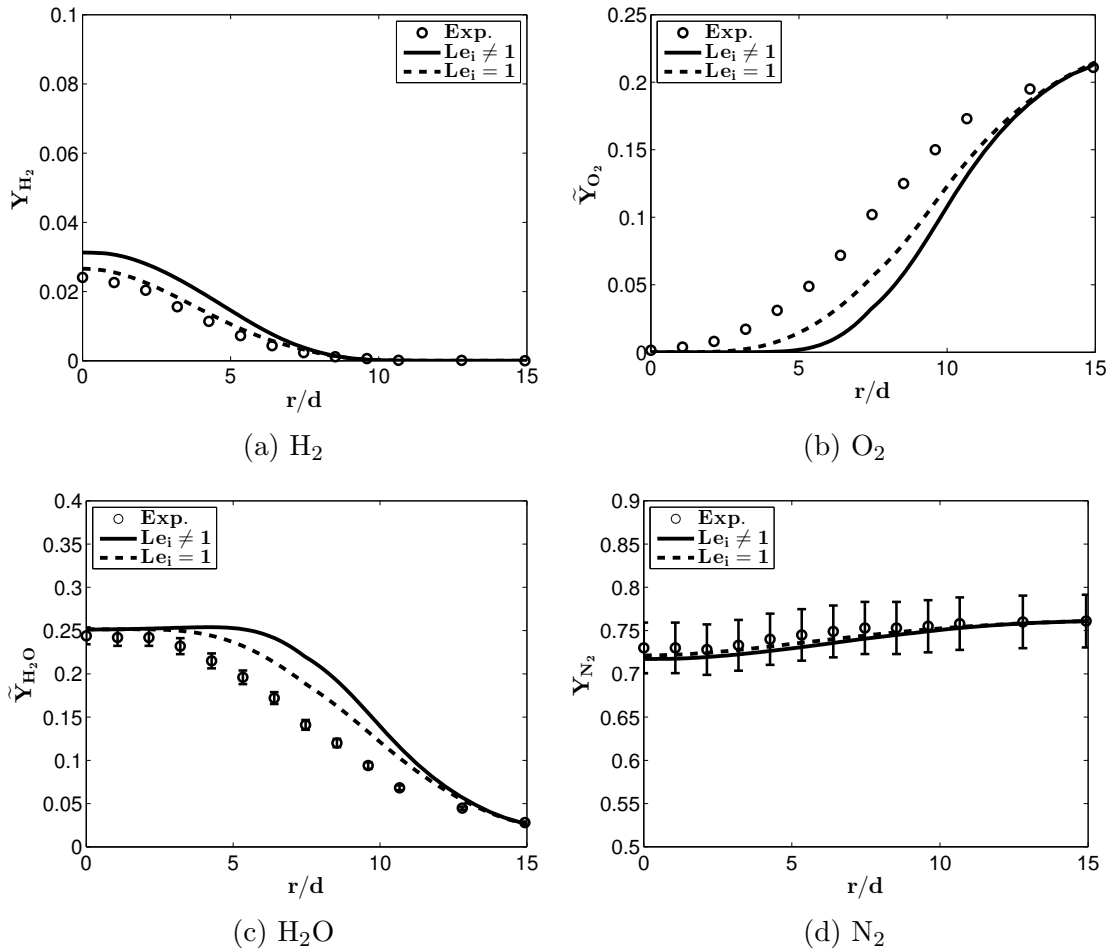


Figure 6.26: Predicted radial profiles of Favre averaged major species mass fraction with differential diffusion effects at $x/L_v = 1/2$. Experimental measurements are from the TNF library [86].

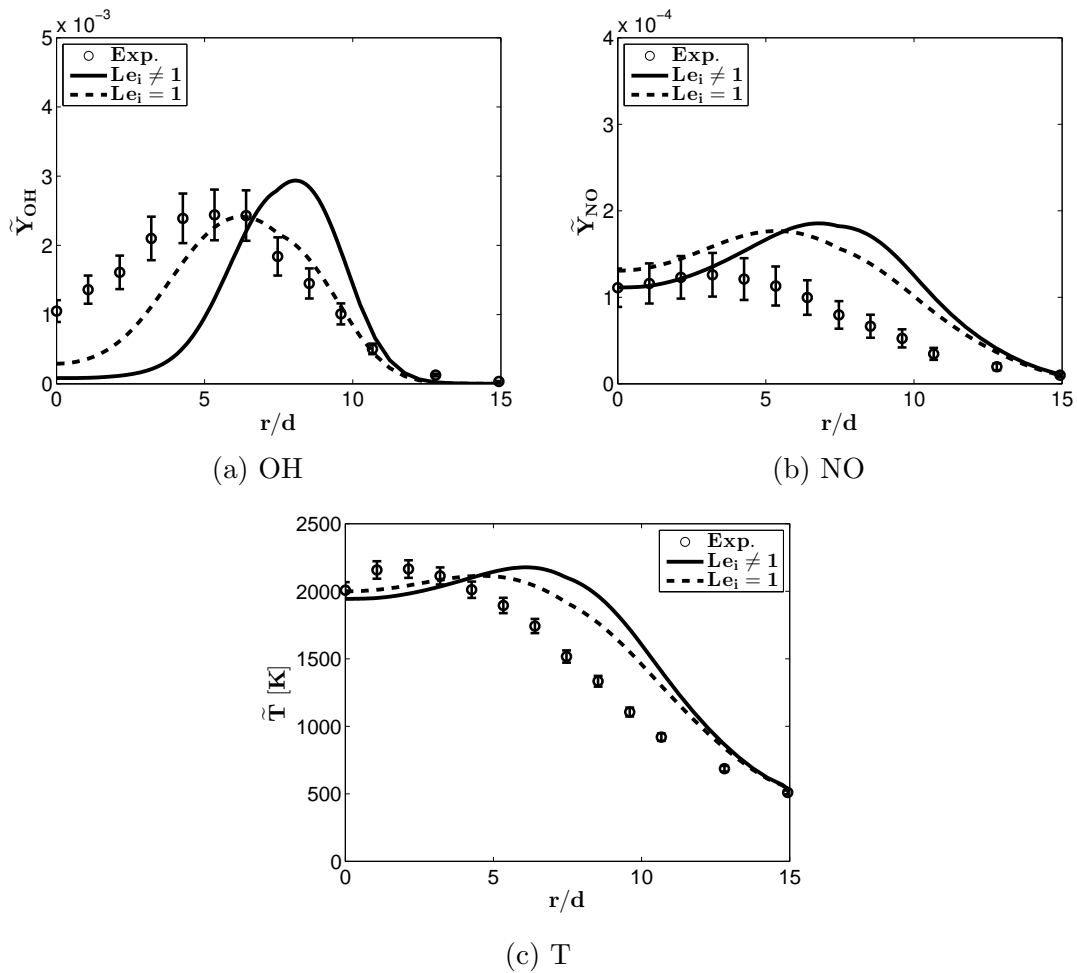


Figure 6.27: Predicted radial profiles of Favre averaged minor species mass fraction and temperature with differential diffusion effects at $x/L_v = 1/2$. Experimental measurements are from the TNF library [86].

One possible reason for the changes observed at the downstream location when differential diffusion is considered, which is also mentioned when examining the conditional profiles in Section 6.6.1, is the history effect described by Pitsch [35]. However, due to the large differences from experimental measurements, it is more seemingly caused by modelling issues. Inadequacies of the k - ε model in obtaining mixing field results may affect important quantities such as the scalar dissipation rate. There may also be inaccuracies in the closure of the terms in the CMC equation.

In the flamelet model calculations of Pitsch [35] described in Section 3.4, a unity Lewis number was specified for a provisional distance from the nozzle, in order to diminish the effects of differential diffusion downstream. Current results in the downstream regions might be improved by employing the same modification, however there are reasons against such an approach. Firstly, the choice of transition location to unity Lewis number requires *a priori* knowledge of the flame, as it is likely to contrast for different flames. The *ad hoc* nature of such a modification is detrimental to the universality of the combustion model, similar to the $C_{\varepsilon 1}$ parameter in the k - ε turbulence model. Instead, it is more desirable to obtain more physical explanations for the discrepancies that are observed. The Lewis number (Eq. 3.2) describes the relationship between thermal and mass diffusion. However, in the CMC species equation, the relationship found in the diffusion terms is between species mass diffusion and mixture fraction diffusion. The Lewis number is introduced only by the assumption of equal mixture fraction and thermal diffusivities $D_\xi = \alpha$. The concept of differential diffusion itself is a “correction” to the assumption of equal diffusivity, based only on the differences in D_i and D_ξ . Under the assumption that $D_\xi = \alpha$ is valid, a transition to unity Lewis number implies that D_i and α are sensitive to the turbulence of the flow. In this case, α increases at a greater rate than D_i as the flow becomes more turbulent. If D_i and α are independent of the turbulent description of the flow, then D_i and α close to the nozzle should be similar to the values at another location in the flow that has similar temperatures. In this case a transition to unity Lewis number would imply that the assumption of $D_\xi = \alpha$ is not valid, and that D_ξ increases for higher turbulence. The validity of the $D_\xi = \alpha$ assumption is of interest. In the derivation of the CMC equation by Kronenburg and Bilger [61], a term was proposed to counteract the differential diffusion term based on a Kolmogorov time scale to introduce a Reynolds number dependence. Additional investigation of the dependence of D_i , D_ξ , and α on turbulence would provide insight into whether transitioning from differential to unity Lewis number is a valid approach.

Additional insight can be gained by examining the η space diffusion terms in the CMC

species equation, Eq. 4.20, which can be rearranged to the following form,

$$\begin{aligned}
 & \underbrace{\frac{\partial^2}{\partial \eta^2} (\langle \rho Y_i D_\xi (\nabla \xi)^2 | \eta \rangle P(\eta)) - \frac{\partial}{\partial \eta} (\langle \rho (2D_\xi) (\nabla \xi \cdot \nabla Y_i) | \eta \rangle P(\eta))}_{\text{equal diffusivity assumption}} \\
 & \quad - \underbrace{\frac{\partial}{\partial \eta} (\langle \rho (D_i - D_\xi) (\nabla \xi \cdot \nabla Y_i) | \eta \rangle P(\eta))}_{\text{correction accounting for different diffusivities}}, \tag{6.11}
 \end{aligned}$$

where the first two terms represent the molecular diffusion under the equal diffusivity case, found in Eq. 4.7, and the third term represents a “correction” that relaxes the equal diffusivity assumption. The third term is of similar form to the second term except for the diffusivities. If the Lewis number does not scale with the turbulence, then it would indicate that the presence of differential diffusion effects in the downstream locations is due to overpredicting the magnitude of the other components of the third term. However, since the third term is of similar form to the second term, this would also indicate that the closure of the second term is also not accurate. Therefore, it may be due not only to the modelling of the differential diffusion term alone, but also due to the second term describing molecular diffusion with the equal diffusivity assumption, and possibly the first term as well. Lignell *et al.* [69] examined the terms of the CMC equation for H using DNS for an ethylene flame and found that the modelled terms were overpredicted by double the DNS results. Hewson *et al.* [6] suggested that the residual terms left from the closure of the diffusion terms may be significant. Klimenko and Bilger [7] noted that the closure for the two diffusion terms had noticeable errors, but the errors of the two terms tended to balance out under equal diffusivity. Though the primary closure hypothesis may have been sufficient under the equal diffusivity assumption, differential diffusion might amplify the error. In other words, the primary closure hypothesis may not perform well for closing the diffusion terms, and investigation into improving the closure method is warranted, though doing so may require the use of DNS.

Besides possible modelling issues for the diffusion terms resulting in an overestimation of molecular diffusion, the observation of differential diffusion effects might be due to underprediction of turbulent mixing by the advection term in Eq. 4.20. This may be due to the underprediction of mixture fraction variance at the downstream location in Fig. 6.9, resulting in lower scalar dissipation rates. It is also possible that the discrepancies are due to the closure models used for the turbulent velocity and turbulent flux (Section 4.5.5).

The modelling of the conditional scalar dissipation rate is one major challenges in CMC studies. The AMC model used in the present study, described in Secton 4.5.6, results in

a symmetric distribution. However, Hilbert and Thévenin [48] conducted a DNS study for a nonpremixed hydrogen-air flame and found that while the conditional scalar dissipation rate profiles were close to Gaussian for equal diffusivities, the profiles were not symmetrical for differential diffusivities, instead skewing to the higher mixture fractions. Investigation into the modelling of the conditional scalar dissipation rate may yield improved results.

6.6.3 Radial Dependence of Conditional Scalars

The conditional profiles presented in Section 6.6.1 were provided in Bilger’s mixture fraction space and cross-stream averaged to compare with experimental data. In this section, the effects of differential diffusion on the radial dependence of the conditional quantities and on results in η space are analyzed. The profiles in η space that are not radially averaged are the CMC results obtained directly from the solution of the CMC equations.

Figure 6.28 presents the predicted conditional mass fraction profiles of H_2 , O_2 , OH , and NO at $x/L_v = 1/8$ plotted against the sample space variable η of the mixture fraction ξ for three radial locations: $r/d = 2, 3$, and 4 . Since the mixture fraction is conserved and indifferent to the effects of differential diffusion of the reacting scalars, the influence of differential diffusion is purely on the movement of H_2 and H across η space. When unity Lewis numbers are set, there is little variation in the conditional profiles in the radial direction, and as such are represented by one profile for each species in Fig. 6.28. However, when differential diffusion is included in the CMC calculations, there are large radial variations in the conditional profiles. The higher H_2 diffusion rate outwards from the core compared to the slower diffusion of air towards the core results in a net increase in the penetration of H_2 from higher to lower mixture fractions, shown by the increase in Q_{H_2} towards the leaner mixture fractions and a decrease in the richer mixtures. At $r/d = 2$, the diffusion of H_2 to the lower values of mixture fraction is greater due to the higher concentration gradients of H_2 closer to the jet core. Q_{H_2} in the lean mixtures drops with increasing radial distance from the centerline as concentration gradients decrease. Correspondingly, larger Q_{O_2} is predicted with increasing radial distance, due to the decrease in H_2 concentrations. The locations of the peak values of Q_{OH} and Q_{NO} vary in the locations in η space for the different radial locations. The peaks move towards the lower mixture fractions closer to the centerline, indicating a greater amount of differential diffusion in those regions. The shift of the profiles had also been observed by Kronenburg and Bilger [61], though the radial dependence was not analyzed. The lower Q_{OH} and higher Q_{NO} at the larger radial distances may be due to lower mixture fraction variance and scalar dissipation, resulting in profile closer to equilibrium conditions.

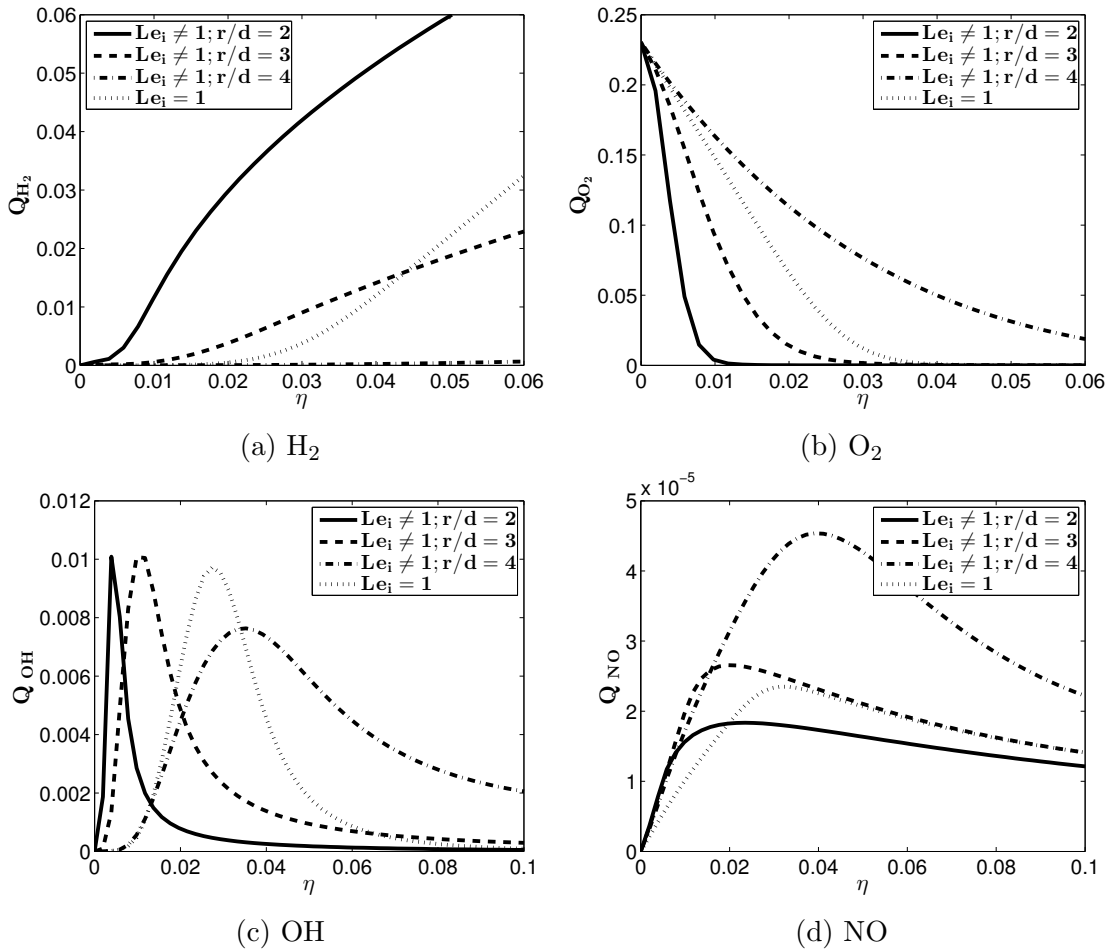


Figure 6.28: Predicted profiles of conditional means of H_2 , O_2 , OH , and NO mass fraction with differential diffusion effects (H_2 and H) for various radial positions at $x/L_v = 1/8$, in conserved mixture fraction space.

The conditional mass fraction profiles shown in Fig. 6.28 are mapped to η_{blgr} space and presented in Fig. 6.29. The result of the mapping is a movement of the profiles towards the local mean mixture fraction, $\eta_{blgr} = \xi_{blgr}$. On the lean side of $\eta_{blgr} = \xi_{blgr}$, the profile is shifted to the right, while a shift to the left is found on the rich side. $Q_{H_2}^*$ and $Q_{O_2}^*$ profiles with differential diffusion converge to the profiles for equal diffusivities, such that the stoichiometric value of the mixture fraction is conserved. The profiles without differential diffusion remain unchanged, which affirms that $\xi_{blgr} = \xi$ when the differential diffusion effects are not considered. The peaks of Q_{OH}^* and Q_{NO}^* gather to a value of η_{blgr} , so that the profiles are aligned. However, Q_{OH}^* and Q_{NO}^* show apparent radial variation in the magnitudes. In the presence of differential diffusion calculations with CMC, major reactant species may be reasonably approximated by solving radially averaged equations; however, the production of species such as OH and NO show large radial variations and the CMC equations should be solved in two dimensions (axial and radial).

6.6.4 Differential Diffusion Effects of Individual Species

The individual effects of the differential diffusion of H_2 , H, OH, and O are examined in this section. Conditional profiles are obtained by performing four different cases, where each of the forementioned chemical species are the sole differentially diffusing species. The conditional profiles are compared with the equal diffusivity results.

The cross-averaged conditional H_2 , H_2O , OH, and NO mass fractions at $x/L_v = 1/8$ for the differential diffusion of H_2 and the differential diffusion of H are compared with the unity Lewis number profiles in Fig. 6.30. The conditional profiles in Fig. 6.30 are presented in the conserved mixture fraction sample space η , so that the effects of differential diffusion are more distinguishable. The plots for the differential diffusion of H_2 results in a clear shift of the profiles to lower η corresponding to the increased diffusion rate from the higher concentrations of H_2 at rich mixture fractions. The increase of fuel diffusion rate towards the reaction zone also results in higher production of H_2O and NO. The modelling of the differential diffusion of H shows a more subtle, but nonetheless informative, effect on the conditional profiles of Fig. 6.30. The concentrations of H are small, such that the apparent stoichiometric mixture fraction value is relatively unchanged. The expected influence of differential diffusion on H is a greater spread to the lower and higher mixture fractions. The changes in the profiles appear to be more significant on the rich side of the stoichiometric value than for the lean regions, which is most apparent in the Q_{OH}^* profile. The resulting increase in NO when differential diffusion of H is included is different from the result obtained by Kronenburg *et al.* [61] where NO concentrations were decreased.

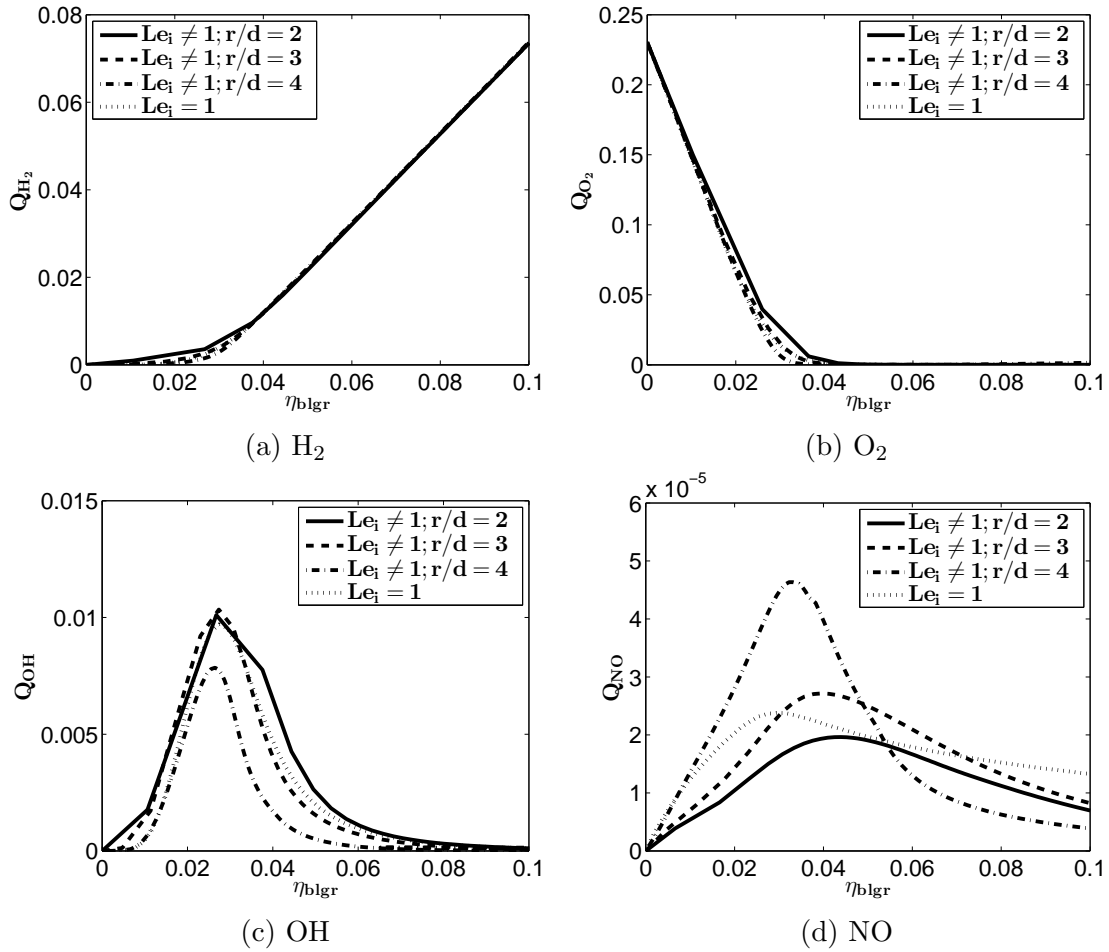


Figure 6.29: Predicted profiles of conditional means of H_2 , O_2 , and OH mass fraction with differential diffusion effects (H_2 and H) for various radial positions at $x/L_v = 1/8$, in Bilger's mixture fraction space.

The overall effect of the differential diffusion of H_2 is large than for H , which is reasonable due to the significantly higher concentrations and concentration gradients of H_2 .

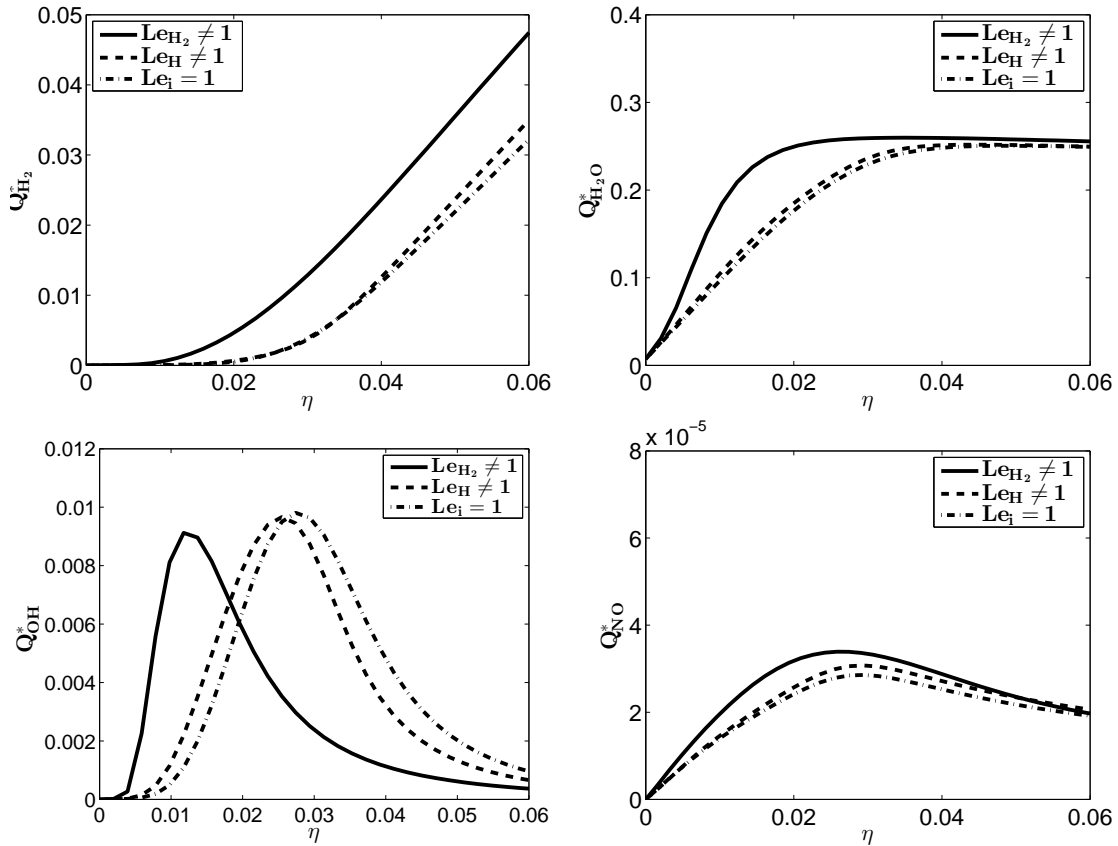


Figure 6.30: Predicted conditional profiles of independent contributions of $Le_{H_2} = 0.3$ and $Le_H = 0.18$ at $x/L_v = 1/8$, in conserved mixture fraction space.

The same analysis is conducted for the individual differential diffusion effects of OH and O . Since the difference from unity Lewis number is much smaller than for H_2 and H , and the concentrations of OH and O are significantly lower than H_2 , accounting for the differential diffusion of OH and O is observed to have negligible effect on the calculated conditional scalars.

6.6.5 Analysis of CMC equation

In this section, budgets of the terms in the CMC calculations are presented. Though there is no supplementary data, such as DNS, available for comparison, a qualitative analysis can nonetheless provide additional insight in the application of the CMC model with differential diffusion effects.

Firstly, the CMC equations, Eqs. 4.66 and 4.67 are rearranged to a more practical form for analyzing the contribution of differential diffusion modelling. In steady-state, without the term related to unsteady effects, the CMC equation governing the conditional species mass fractions, Eq. 4.66, can be rearranged into the following form,

$$\begin{aligned}
 & \underbrace{\frac{\nabla \cdot (\rho_\eta \langle \bar{v} Y_i | \eta \rangle P_\eta)}{\bar{\rho} \tilde{P}} - \frac{\nabla \cdot (\rho_\eta \langle \bar{v} | \eta \rangle P_\eta) Q_i}{\bar{\rho} \tilde{P}}}_{\text{Advection}} = \underbrace{\dot{\omega}_{i,\eta}}_{\text{Source}} + \underbrace{\frac{1}{2} \chi_\eta \frac{\partial^2 Q_i}{\partial \eta^2}}_{\text{equal diffusivity assumption (ED)}} \\
 & \underbrace{-\frac{1}{2} \left(1 - \frac{1}{Le_i}\right) \chi_\eta \frac{\partial^2 Q_i}{\partial \eta^2} - \frac{1}{2} \left(1 - \frac{1}{Le_i}\right) \frac{1}{\bar{\rho} \tilde{P}} \frac{\partial \bar{\rho} \chi_\eta \tilde{P}}{\partial \eta} \frac{\partial Q_i}{\partial \eta}}_{\text{correction accounting for different diffusivities (DD)}} \\
 & + \underbrace{\frac{\nabla^2 (\langle \rho D_i Y_i | \eta \rangle P(\eta))}{\bar{\rho} \tilde{P}} - \frac{\nabla \cdot (\langle \nabla (\rho D_i) Y_i | \eta \rangle P(\eta))}{\bar{\rho} \tilde{P}}}_{\text{spatial diffusion (SD)}}, \tag{6.12}
 \end{aligned}$$

where the ED term is the same term found in the CMC equation under unity Lewis number assumption, and the DD term represents a correction to the unity Lewis number case to account for differential diffusivities. Figure 6.31 presents the budget of the terms in Eq. 6.12 for H_2 at $x/L_v = 1/8$ for two radial positions. The two radial locations are $r/d = 2$, where the mixture is fuel rich, and $r/d = 3$, close to the location of the stoichiometric mixture fraction. The terms related to the spatial diffusion of the conditional averages, the last two terms on the RHS of Eq. 6.12 (SD), are not shown in Fig. 6.31 since they are found to be negligible compared to the other terms. As can be seen in Fig. 6.31, the DD, source, and advective terms are larger in magnitude compared to the ED term at both radial locations, confirming the non-negligible effect of differential diffusion close to the nozzle. As expected, the chemical source term for H_2 is significant around the values of η where the mixture composition is close to stoichiometric conditions, as shown in Fig. 6.31. At $r/d = 2$ on the lean side of stoichiometry ($\eta < 0.008$), the DD, source, and advective terms significantly contribute to the CMC equation, while on the fuel side of stoichiometry ($\eta > 0.008$), the balance is between DD and advection only. Farther out in the radial direction, at $r/d = 3$ (Fig. 6.31), the chemical source is mainly balanced by

DD for $\eta < 0.03$, while for $\eta > 0.03$, when limited (or no) chemical activity takes place, DD and advection balance each other. Further examination of Eq. 6.12 shows that the diffusion of H_2 from the higher mixture fractions can be mainly attributed to the second component of the DD term involving $\frac{\partial Q_i}{\partial \eta}$, which causes a decrease in H_2 mass fractions at higher η and an increase at lower η .

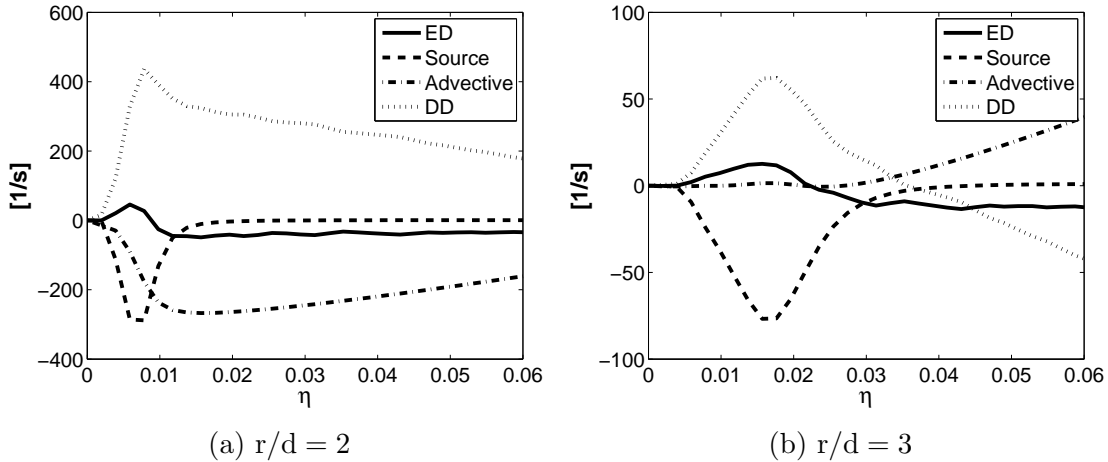


Figure 6.31: Budget of terms in CMC equation of Y_{H_2} at $x/L_v = 1/8$.

Figure 6.32 presents the budget of the terms in Eq. 6.12 for H for the same positions. Similar to the observations made for H_2 , the two major terms in the CMC equation for H are chemistry and DD, as shown in Fig. 6.32, with ED and advection having much smaller contributions. In contrast to the H_2 budget, a double peak in the chemical source term can be seen for both radial positions, one located on the fuel lean and one around stoichiometry. Similarly, a double peak is also shown in the DD term, which is the main term balancing the chemical source term. The present observations are in qualitative agreement with the findings shown by Lignell et al. [69], though the study was applied to an ethylene flame.

The budgets for the terms of Eq. 6.12 for H_2 and H farther downstream at $x/L_v = 1/2$ are presented in Figs. 6.33 and 6.34, respectively, for radial locations of $r/d = 5$ and 7. At this axial location, the radial location of $r/d = 5$ corresponds to the fuel rich region, while $r/d = 7$ lies close to the location of the stoichiometric mixture fraction. For both radial locations in Figs. 6.33 and 6.34, the profiles of the terms are similar to their respective counterparts at $x/L_v = 1/8$ in Figs. 6.31 and 6.32, albeit with lower magnitudes. The DD terms remain on the same order of magnitude as the source, ED, and advective terms. The relative significance of the DD terms at the $x/L_v = 1/2$ may contribute to the observation of differential effects in the conditional scalars in Section 6.6.2.

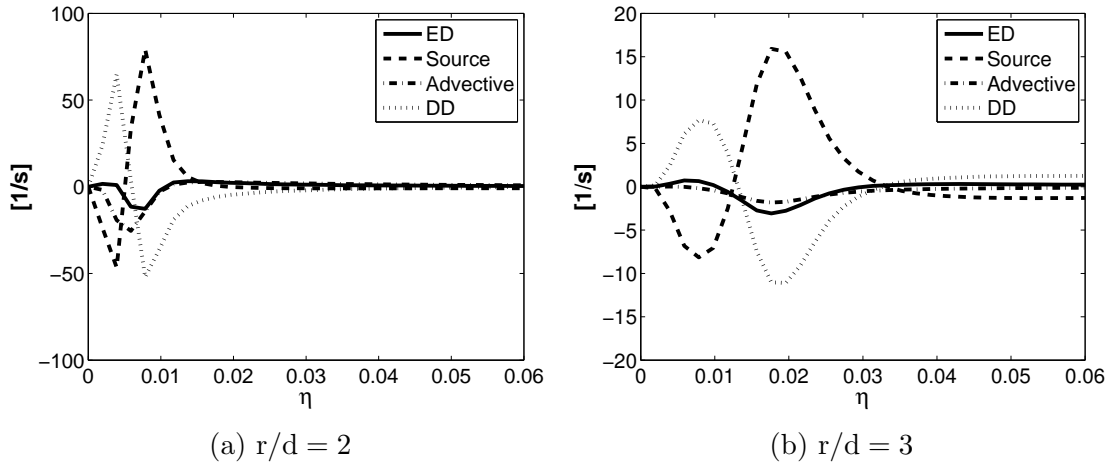


Figure 6.32: Budget of terms in CMC equation of Y_H at $x/L_v = 1/8$.

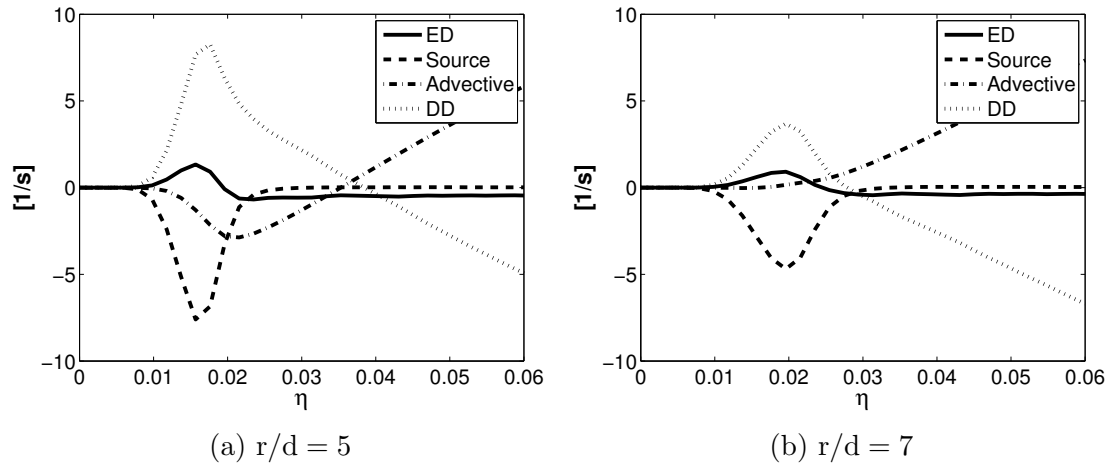


Figure 6.33: Budget of terms in CMC equation of Y_{H_2} at $x/L_v = 1/2$.

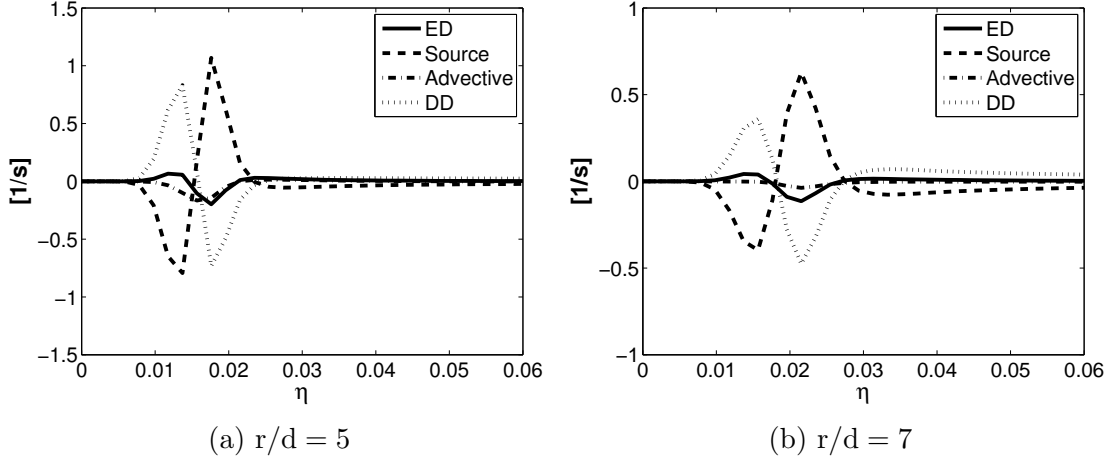


Figure 6.34: Budget of terms in CMC equation of Y_H at $x/L_v = 1/2$.

Likewise, the steady-state CMC equation for enthalpy, Eq. 4.67 can be decomposed into several terms such that

$$\begin{aligned}
& \underbrace{\frac{\nabla \cdot (\rho_\eta \langle \vec{v}h | \eta \rangle P_\eta)}{\bar{\rho}\tilde{P}} - \frac{\nabla \cdot (\rho_\eta \langle \vec{v} | \eta \rangle P_\eta) Q_h}{\bar{\rho}\tilde{P}}}_{\text{Advection}} = \underbrace{s_{\eta,h}}_{\text{Source}} + \underbrace{\frac{1}{2}\chi_\eta \frac{\partial^2 Q_h}{\partial \eta^2}}_{\text{equal diffusivity assumption (ED)}} \\
& - \underbrace{\left(1 - \frac{1}{Le_{H_2}}\right) \frac{1}{\bar{\rho}\tilde{P}} \frac{\partial}{\partial \eta} \left(\frac{\bar{\rho}\chi_\eta Q_h \tilde{P}}{2} \frac{\partial Q_{H_2}}{\partial \eta} \right)}_{\text{correction accounting for differential diffusivity of H}_2 \text{ (DD H}_2\text{)}} \\
& - \underbrace{\left(1 - \frac{1}{Le_H}\right) \frac{1}{\bar{\rho}\tilde{P}} \frac{\partial}{\partial \eta} \left(\frac{\bar{\rho}\chi_\eta Q_h \tilde{P}}{2} \frac{\partial Q_H}{\partial \eta} \right)}_{\text{correction accounting for differential diffusivity of H (DD H)}} \\
& + \frac{\nabla \cdot (\langle \rho D_\xi \nabla h \rangle P_\eta)}{\bar{\rho}\tilde{P}} + \frac{\nabla \cdot (\langle \rho (\alpha - D_\xi) \nabla h \rangle P_\eta)}{\bar{\rho}\tilde{P}} \\
& - \underbrace{\sum_i \frac{(\nabla \cdot (\langle \rho h_i (\alpha - D_i) \nabla Y_i \rangle P_\eta))}{\bar{\rho}\tilde{P}}}_{\text{spatial diffusion (SD)}}, \tag{6.13}
\end{aligned}$$

where the ED term is the same term found in the CMC equation under unity Lewis number assumption, and the DD H₂ and DD H terms represent corrections to the unity Lewis

number case to account for the differential diffusivities of H_2 and H , respectively. Figure 6.35 presents the budget of the terms in Eq. 6.13 at $x/L_v = 1/8$ for two radial locations. Similar to Eq. 6.12, the last three terms on the RHS of Eq. 6.13 are negligible compared to the other terms, and are excluded from Fig. 6.35. At $r/d = 2$, all the terms are on the same order. The advection, $DD H_2$, and $DD H$ terms peak on the lean side and near the stoichiometric mixture fraction ($\eta < 0.008$), where the enthalpy gradients are found to be the highest, while two peaks can be seen for ED on both sides of stoichiometric conditions. At $r/d = 3$, the largest contributions come from the ED and source terms, suggesting that the relative contributions of the differential diffusion terms scale with the inverse of the local temperature since the temperature values are higher at $r/d = 3$ compared to those at $r/d = 2$.

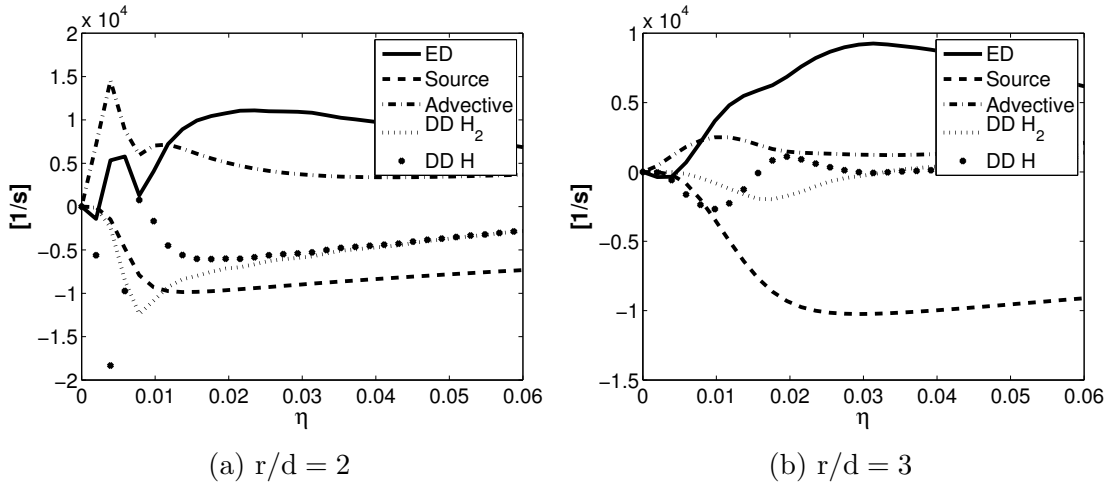


Figure 6.35: Budget of terms in CMC equation of h at $x/L_v = 1/8$.

The budgets for the terms of Eq. 6.13 farther downstream at $x/L_v = 1/2$ are presented in Fig. 6.36 for radial locations of $r/d = 5$ and 7. Similar to the first axial location, the ED, source, and advective terms at both radial locations exhibit comparable magnitudes. However, different from the results in Fig. 6.35, the terms involving the differential diffusion of H_2 and H in Fig. 6.36 are small relative to the other terms. The diminished effects of differential diffusion downstream from the nozzle appear to be captured by Eq. 6.13, unlike for the species equations (Eq. 6.12).

Outside of the qualitative analysis performed here, further investigation of the contributions of the terms in the CMC equation can benefit from DNS; however, such analysis is outside the scope of the present study.

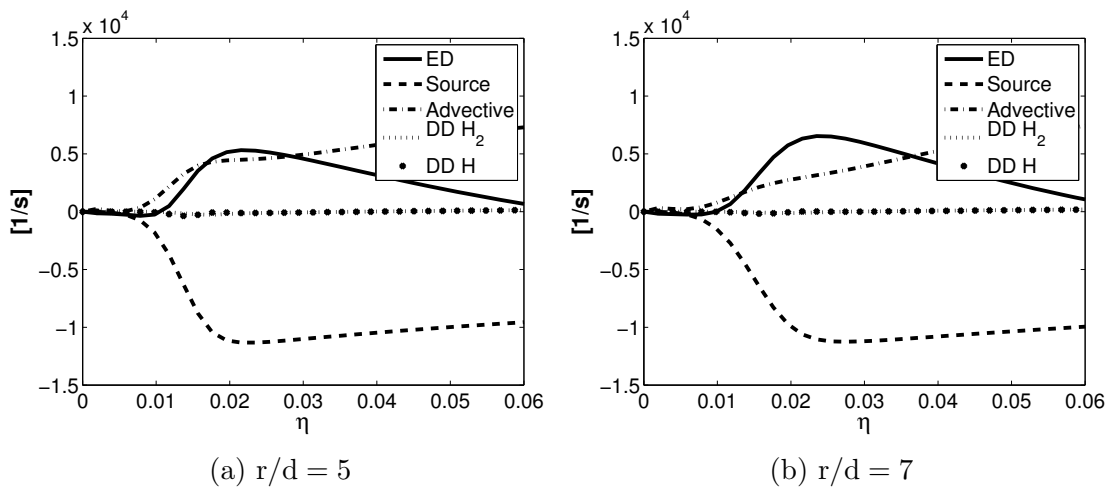


Figure 6.36: Budget of terms in CMC equation of h at $x/L_v = 1/2$.

Chapter 7

Conclusions

The focus of the present study is the investigation of differential diffusion effects in a turbulent hydrogen-air non-premixed flame using the CMC method. The first order CMC model of the species transport equation, which allows for different diffusivities of chemical species to be considered, is fully coupled with a RANS method and is applied to the steady two dimensional simulation of the flame experimentally studied by Barlow and Carter [38]. The model, to the author's knowledge, has not been previously implemented to a RANS or LES simulation of a flame. Additionally, a CMC formulation of the enthalpy transport equation which accounts for species differential diffusion effects is derived in this study using a similar method to the derivation of the species equation, and implemented in the CMC calculations. The advantages of the present CMC formulation are that no additional equations are introduced compared to CMC without differential diffusion, and the CMC equations are in conservative form entirely consistent with the solution of the mixture fraction PDF. The numerical implementation of the CMC model is described, including the discretisation of the CMC equations and the various submodels used for the various unclosed terms such as the conditional scalar dissipation rate, velocity, turbulent flux, chemical source term, and probability density function in the CMC equations. Differential diffusion effects of H_2 , H, OH, and O are investigated by comparison to results obtained from unity Lewis number calculations and to experimental data, with particular interest in the production of radicals such as OH and NO.

7.1 Hydrogen Flame Results

The hydrogen-air flame calculations are first validated under equal diffusivity assumption using CMC. The trends show an underprediction in the diffusion of mean H_2 mass fraction towards the lean regions close to the nozzle. Due to lower movement of fuel towards the reaction zone, lower H_2O and NO mass fractions are found near the nozzle compared to experimental measurements. The underprediction of NO mass fraction is especially significant, with peak value lower than the measurements by approximately 56%. As well, OH production is observed to occur closer to the centerline than the measurements.

The inclusion of non unity Lewis numbers of H_2 and H in the CMC calculations results in a higher penetration of H_2 into the fuel lean mixtures and a greater spreading of H . With differential diffusion effects, the conditional profiles of temperature, H_2O , and NO mass fraction show some improvement close to the nozzle at $x/L_v = 1/8$ where differential diffusion effects are prominent in comparison with the experimental data for mixture fractions on the rich side of stoichiometric conditions. In particular, the increase in the peak NO mass fraction of approximately 40% compared to the equal diffusivity predictions is promising. Unconditional Favre averaged profiles also show improvement for the mixture fraction, H_2 , H_2O , O_2 , N_2 , and NO mass fractions. However, though the peak unconditional NO mass fraction is increased by approximately 31%, it remains lower than the experimental measurements by 30%. Also observed is a shift in the location of OH production resulting in the alignment of the predicted and measured locations of peak OH , explained by the relocation of the reaction zone to the leaner regions due to greater diffusion rates of the fuel. However, mean OH mass fraction and temperature are higher than experimental measurements, which may be caused by an underprediction of heat diffusion. It is also found that the differential diffusion effects persist farther downstream where they would be expected to be negligible.

Several possible sources of discrepancy can be identified which may lead to the observed differences from the experimental measurements. First, the present CMC formulation includes several assumptions related to the closure of the additional differential diffusion terms. In particular, the residual terms are neglected in the closure of the η space diffusion terms. The *a priori* analysis in [69] showed some differences in the modelled terms compared to the DNS values for H . The conditional species fluctuations may also have a non-negligible effect in the near field of the flame. Second order closure for the chemical source had previously been applied to the same flame in CMC without differential diffusion [99], though no significant improvement was noticed near the nozzle. Instead, Hewson et al. [68] suggested that the conditional fluctuations could be included in the differential diffusion terms. Further, Clemens and Paul [100] mentioned that heat release near the

nozzle potentially leading to flow laminarization. This effect is not captured by the current RANS calculations. It had also been previously suggested that the Lewis number, which is assumed constant in the present study, could depend on the Reynolds number [35]. As well, the assumption of $\alpha = D_\xi$, and its dependence on Reynolds number, may not be a valid assumption.

The differential diffusion effects in the CMC equations are seen to produce significant radial variations in the conditional profiles, much larger than those without differential diffusion. This increased radial dependence is caused by differences in the local concentration gradients of differentially diffusive species. The conditional profiles converge when mapped to Bilger's mixture fraction space, which conserves the stoichiometric mixture fraction. For major species such as H_2 and O_2 , the convergence of the profiles shows that radial averaging of the CMC equations is justifiable. However, for minor species such as OH and NO, there is significant radial variation in the mass fraction profiles even in Bilger's mixture fraction space. Radial averaging of the CMC equation may not be accurate in the consideration of differential diffusion for the prediction of minor species, and the solution of the two dimensional equations is recommended over the one dimensional cross-stream averaged equations.

An analysis of the effects of the differential diffusion effects of individual species show that the differential diffusion of H_2 has the greatest impact on the results due to the high concentrations of H_2 . The effects of H diffusion are significantly smaller than those of H_2 due to lower concentrations, though should still be included. Inclusion of non unity Lewis number for OH and O has a negligible impact on species mass fraction predictions.

Budgets of the terms in the CMC equations show the large significance of differential diffusion contributions in the equations for H_2 and H. The differential diffusion contributions are balanced by chemical source term close to the stoichiometric mixture fractions, and by advection for higher mixture fractions. The terms accounting for differential diffusion are still observed to be of comparable magnitude to the other terms downstream from the nozzle, where the effects of differential diffusion are expected to be small. The discrepancy may be due to modelling inaccuracies of the diffusion terms, the advection terms, or the assumption of constant Lewis numbers.

7.2 Recommendations and Future Work

There are several possible causes for the differences in the calculated and measured results that are discussed in this study. Analysis of these conjectures will lead to refinement of

the CMC model with differential diffusion effects. An investigation into the appropriate form of the closure models using DNS for the CMC equations could lead to new insight into the applicability of the model to the flame studied under consideration. Particularly of interest are the closures for the diffusion terms (the primary closure hypothesis), the advection terms, and the conditional scalar dissipation rate (which has been observed to be asymmetric under differential diffusion effects [48]). In addition, DNS studies may also provide additional information on the Reynolds number dependence of the Lewis number, and the validity of the $\alpha = D_\xi$ assumption.

Improvement to the turbulent flow and mixing field predictions, such as with the use of LES, is also needed to provide better overall mean species predictions compared to the experimental data. Due to computational requirements of DNS studies, improvement to flow and mixing field predictions using LES may be more accessible for the near future. Further numerical optimization may also be pursued to reduce the computational cost, in particular for future LES calculations.

The applicability of the CMC model used in the present study to other flames is also of interest. The application of the model should be extended to evaluate its prediction of differential diffusion effects for other hydrogen based flames, such as H_2/CO_2 , H_2/N_2 , and H_2/CH_4 flames, or the differential diffusion effects of soot in flames such as ethylene flames.

In the CMC formulation used in the current study, there is no significant increase in computational cost with additional differentially diffusing species since no additional conservation equations are solved. However, a direct comparison with other model formulations to quantify the computational cost and performance, especially with the CMC model of Kronenburg and Bilger [61], could be performed by implementing the models with the similar codes, where the only difference is the combustion model used.

APPENDICES

Appendix A

Derivation of CMC species transport equation

The transport equation for the joint PDF of Y_i and ξ (Eq. 4.18) is

$$\begin{aligned}
 \frac{\partial \langle \rho | Y_i = Z_Y, \xi = \eta \rangle P_{Z_Y, \eta}}{\partial t} + \nabla \cdot (\langle \rho \mathbf{u} | Y_i = Z_Y, \xi = \eta \rangle P_{Z_Y, \eta}) \\
 = -\frac{\partial}{\partial Z_Y} (\langle \nabla \cdot (\rho D_i \nabla Y_i) | Y_i = Z_Y, \xi = \eta \rangle P_{Z_Y, \eta}) \\
 - \frac{\partial}{\partial \eta} (\langle \nabla \cdot (\rho D_\xi \nabla \xi) | Y_i = Z_Y, \xi = \eta \rangle P_{Z_Y, \eta}) \\
 - \frac{\partial}{\partial Z_Y} (\langle \rho \dot{\omega}_i | Y_i = Z_Y, \xi = \eta \rangle P_{Z_Y, \eta}).
 \end{aligned} \tag{A.1}$$

Klimenko and Bilger [7] provided the following identities,

$$\begin{aligned}
 \nabla \cdot (\rho D \nabla \psi) = -\frac{\partial}{\partial Z_1} (\psi \nabla \cdot (\rho D \nabla Y_1)) - \frac{\partial}{\partial Z_2} (\psi \nabla \cdot (\rho D \nabla Y_2)) + \frac{\partial^2}{\partial Z_1^2} (\psi \rho D (\nabla Y_1)^2) \\
 + \frac{\partial^2}{\partial Z_2^2} (\psi \rho D (\nabla Y_2)^2) + 2 \frac{\partial^2}{\partial Z_1 \partial Z_2} (\psi \rho D (\nabla Y_1 \nabla Y_2)),
 \end{aligned} \tag{A.2}$$

and

$$\nabla \cdot (\rho D \nabla \psi) = \nabla^2 (\psi \rho D) - \nabla \cdot (\psi \nabla (\rho D)), \tag{A.3}$$

where Eqs. A.2 and A.3 can be combined to obtain

$$\begin{aligned}
\nabla^2 (\psi \rho D) - \nabla \cdot (\psi \nabla (\rho D)) &= -\frac{\partial}{\partial Z_1} (\psi \nabla \cdot (\rho D \nabla Y_1)) - \frac{\partial}{\partial Z_2} (\psi \nabla \cdot (\rho D \nabla Y_2)) \\
&+ \frac{\partial^2}{\partial Z_1^2} (\psi \rho D (\nabla Y_1)^2) + \frac{\partial^2}{\partial Z_2^2} (\psi \rho D (\nabla Y_2)^2) \\
&+ 2 \frac{\partial^2}{\partial Z_1 \partial Z_2} (\psi \rho D (\nabla Y_1 \nabla Y_2)).
\end{aligned} \tag{A.4}$$

Setting $Y_1 = Y_i$, $Z_1 = Z_Y$, $Y_2 = \xi$, $Z_2 = \eta$, and $D = D_i$ in Eq. A.4, and using the relationship $\langle \circ \psi \rangle = \langle \circ | Y_i = Z_Y, \xi = \eta \rangle P(Z_Y, \eta)$, where \circ is a general quantity [7], Eq. A.4 becomes

$$\begin{aligned}
\nabla^2 (\langle \rho D_i | Y_i = Z_Y, \xi = \eta \rangle P_{Z_Y, \eta}) - \nabla \cdot (\langle \nabla (\rho D_i) | Y_i = Z_Y, \xi = \eta \rangle P_{Z_Y, \eta}) \\
&= -\frac{\partial}{\partial Z_Y} (\langle \nabla \cdot (\rho D_i \nabla Y_i) | Y_i = Z_Y, \xi = \eta \rangle P_{Z_Y, \eta}) \\
&- \frac{\partial}{\partial \eta} (\langle \nabla \cdot (\rho D_i \nabla \xi) | Y_i = Z_Y, \xi = \eta \rangle P_{Z_Y, \eta}) \\
&+ \frac{\partial^2}{\partial Z_Y^2} (\langle \rho D_i (\nabla Y_i)^2 | Y_i = Z_Y, \xi = \eta \rangle P_{Z_Y, \eta}) \\
&+ \frac{\partial^2}{\partial \eta^2} (\langle \rho D_i (\nabla \xi)^2 | Y_i = Z_Y, \xi = \eta \rangle P_{Z_Y, \eta}) \\
&+ 2 \frac{\partial^2}{\partial Z_Y \partial \eta} (\langle \rho D_i (\nabla Y_i \nabla \xi) | Y_i = Z_Y, \xi = \eta \rangle P_{Z_Y, \eta}).
\end{aligned} \tag{A.5}$$

The first term on the RHS of Eq. A.5 corresponds to the first term on the RHS of Eq. A.1. Substituting Eq. A.5 into Eq. A.1 gives Eq. 4.19 in Section 4.3,

$$\begin{aligned}
& \frac{\partial \langle \rho | Y_i = Z_Y, \xi = \eta \rangle P_{Z_Y, \eta}}{\partial t} + \nabla \cdot (\langle \rho \mathbf{u} | Y_i = Z_Y, \xi = \eta \rangle P_{Z_Y, \eta}) \\
&= -\frac{\partial}{\partial \eta} (\langle \nabla \cdot (\rho (D_\xi - D_i) \nabla \xi) | Y_i = Z_Y, \xi = \eta \rangle P_{Z_Y, \eta}) \\
&+ \nabla^2 (\langle \rho D_i | Y_i = Z_Y, \xi = \eta \rangle P_{Z_Y, \eta}) \\
&- \nabla \cdot (\langle \nabla (\rho D_i) | Y_i = Z_Y, \xi = \eta \rangle P_{Z_Y, \eta}) \\
&- \frac{\partial^2}{\partial Z_Y^2} (\langle \rho D_i (\nabla Y_i)^2 | Y_i = Z_Y, \xi = \eta \rangle P_{Z_Y, \eta}) \\
&- \frac{\partial^2}{\partial \eta^2} (\langle \rho D_i (\nabla \xi)^2 | Y_i = Z_Y, \xi = \eta \rangle P_{Z_Y, \eta}) \\
&- 2 \frac{\partial^2}{\partial Z_Y \partial Z_\eta} (\langle \rho D_i (\nabla Y_i \nabla \xi) | Y_i = Z_Y, \xi = \eta \rangle P_{Z_Y, \eta}) \\
&- \frac{\partial}{\partial Z_Y} (\langle \rho \dot{\omega}_i | Y_i = Z_Y, \xi = \eta \rangle P_{Z_Y, \eta}).
\end{aligned} \tag{A.6}$$

In order to obtain an transport equation in terms of the single variable PDF, $P(\eta)$, each term in Eq. A.6 is multiplied by Z_Y and subsequently integrated over Z_Y . The integrals of each term, determined using integration by parts, are as follows:

$$\int_{-\infty}^{\infty} Z_Y \frac{\partial \langle \rho | Y_i = Z_Y, \xi = \eta \rangle P_{Z_Y, \eta}}{\partial t} dZ_Y = \frac{\partial \langle \rho Y_i | \xi = \eta \rangle P_\eta}{\partial t} \tag{A.7}$$

$$\int_{-\infty}^{\infty} Z_Y \nabla \cdot (\langle \rho \mathbf{u} | Y_i = Z_Y, \xi = \eta \rangle P_{Z_Y, \eta}) dZ_Y = \nabla \cdot (\langle \rho \mathbf{u} Y_i | \xi = \eta \rangle P_\eta) \tag{A.8}$$

$$\int_{-\infty}^{\infty} Z_Y \nabla^2 (\langle \rho D_i | Y_i = Z_Y, \xi = \eta \rangle P_{Z_Y, \eta}) dZ_Y = \nabla^2 (\langle \rho D_i Y_i | \xi = \eta \rangle P_\eta) \tag{A.9}$$

$$\int_{-\infty}^{\infty} Z_Y \nabla \cdot (\langle \nabla (\rho D_i) | Y_i = Z_Y, \xi = \eta \rangle P_{Z_Y, \eta}) dZ_Y = \nabla \cdot (\langle \nabla (\rho D_i) Y_i | \xi = \eta \rangle P_\eta) \tag{A.10}$$

$$\begin{aligned}
& \int_{-\infty}^{\infty} Z_Y \frac{\partial}{\partial \eta} (\langle \nabla \cdot (\rho (D_\xi - D_i) \nabla \xi) | Y_i = Z_Y, \xi = \eta \rangle P_{Z_Y, \eta}) dZ_Y \\
&= \frac{\partial}{\partial \eta} (\langle \nabla \cdot (\rho (D_\xi - D_i) \nabla \xi) Y_i | \xi = \eta \rangle P_\eta)
\end{aligned} \tag{A.11}$$

$$\int_{-\infty}^{\infty} Z_Y \frac{\partial^2}{\partial Z_Y^2} (\langle \rho D_i (\nabla Y_i)^2 | Y_i = Z_Y, \xi = \eta \rangle P_{Z_Y, \eta}) dZ_Y = 0 \quad (\text{A.12})$$

$$\begin{aligned} \int_{-\infty}^{\infty} Z_Y \frac{\partial^2}{\partial \eta^2} (\langle \rho D_i (\nabla \xi)^2 | Y_i = Z_Y, \xi = \eta \rangle P_{Z_Y, \eta}) dZ_Y \\ = \frac{\partial^2}{\partial \eta^2} (\langle \rho D_i (\nabla \xi)^2 Y_i | \xi = \eta \rangle P_\eta) \end{aligned} \quad (\text{A.13})$$

$$\begin{aligned} \int_{-\infty}^{\infty} 2Z_Y \frac{\partial^2}{\partial Z_Y \partial Z_\eta} (\langle \rho D_i (\nabla Y_i \nabla \xi) | Y_i = Z_Y, \xi = \eta \rangle P_{Z_Y, \eta}) dZ_Y \\ = \frac{\partial}{\partial \eta} (\langle 2\rho D_i (\nabla Y_i \nabla \xi) | \xi = \eta \rangle P_\eta) \end{aligned} \quad (\text{A.14})$$

$$\int_{-\infty}^{\infty} Z_Y \frac{\partial}{\partial Z_Y} (\langle \rho \dot{\omega}_i | Y_i = Z_Y, \xi = \eta \rangle P_{Z_Y, \eta}) dZ_Y = \langle \rho \dot{\omega}_i | \xi = \eta \rangle P_\eta \quad (\text{A.15})$$

In Eqs. A.7-A.11, A.13, and A.14, the variables t , \mathbf{x} , and η are independent of Z_Y . The result is the unclosed form of the CMC species transport equation,

$$\begin{aligned} \frac{\partial \langle \rho Y_i | \xi = \eta \rangle P_\eta}{\partial t} + \nabla \cdot (\langle \rho Y_i \mathbf{u} | \xi = \eta \rangle P_\eta) &= -\frac{\partial^2}{\partial \eta^2} (\langle \rho D_i (\nabla \xi)^2 Y_i | \xi = \eta \rangle P_\eta) \\ &+ \frac{\partial}{\partial \eta} (\langle 2\rho D_i (\nabla Y_i \nabla \xi) | \xi = \eta \rangle P_\eta) \\ &- \frac{\partial}{\partial \eta} (\langle \nabla \cdot [\rho (D_\xi - D_i) \nabla \xi] Y_i | \xi = \eta \rangle P_\eta) \\ &+ \nabla^2 (\langle \rho D_i Y_i | \xi = \eta \rangle P_\eta) - \nabla \cdot (\langle \nabla (\rho D_i) Y_i | \xi = \eta \rangle P_\eta) \\ &+ \langle \rho \dot{\omega}_i | \xi = \eta \rangle P_\eta. \end{aligned} \quad (\text{A.16})$$

which is the expression given in Eq. 4.20.

Appendix B

Derivation of CMC enthalpy transport equation

Starting from the transport equation for $h\psi_\eta$ (Eq. 4.23), given by

$$\begin{aligned} \frac{\partial \rho h \psi_\eta}{\partial t} + \nabla \cdot (\rho \mathbf{u} h \psi_\eta) = & -\frac{\partial}{\partial \eta} (h \psi_\eta \nabla \cdot (\rho D_\xi \nabla \xi)) + \psi_\eta \nabla \cdot (\rho \alpha \nabla h) \\ & - \psi_\eta \nabla \cdot \left[\sum_i (\rho h_i (\alpha - D_i) \nabla Y_i) \right] + \psi_\eta \rho s h, \end{aligned} \quad (\text{B.1})$$

Eq. B.1 is rearranged using the following set of three identities (details on their derivation in [7]) to a form that is easier for averaging,

$$\begin{aligned} \nabla \cdot (\rho D_\xi h \nabla \psi_\eta) = & \frac{\partial^2}{\partial \eta^2} (\psi_\eta \rho h D_\xi (\nabla \xi)^2) - \frac{\partial}{\partial \eta} (\psi_\eta h \nabla \cdot (\rho D_\xi \nabla \xi)) \\ & - \frac{\partial}{\partial \eta} (\psi_\eta D_\xi \rho (\nabla \xi \cdot \nabla h)), \end{aligned} \quad (\text{B.2})$$

$$\nabla \cdot (\psi_\eta \rho \alpha \nabla h) = \psi_\eta \nabla \cdot (\rho \alpha \nabla h) - \frac{\partial}{\partial \eta} (\psi_\eta \rho \alpha (\nabla \xi \cdot \nabla h)), \quad (\text{B.3})$$

and

$$\nabla \cdot (\psi_\eta \rho (\alpha - D_i) h_i \nabla Y_i) = \psi_\eta \nabla \cdot (\rho (\alpha - D_i) h_i \nabla Y_i) \quad (\text{B.4})$$

$$- \frac{\partial}{\partial \eta} (\psi_\eta \rho (\alpha - D_i) h_i (\nabla \xi \cdot \nabla Y_i)). \quad (\text{B.5})$$

Substituting Eqs. B.2 and B.3 into first and second terms, respectively, on the RHS of Eq. B.1 results in

$$\begin{aligned}
\frac{\partial \rho h \psi_\eta}{\partial t} + \nabla \cdot (\rho \mathbf{u} h \psi_\eta) = & - \left[\frac{\partial^2}{\partial \eta^2} (\psi_\eta \rho h D_\xi (\nabla \xi)^2) - \frac{\partial}{\partial \eta} (\psi_\eta D_\xi \rho (\nabla \xi \cdot \nabla h)) - \nabla \cdot (\rho D_\xi h \nabla \psi_\eta) \right] \\
& + \left[\nabla \cdot (\psi_\eta \rho \alpha \nabla h) + \frac{\partial}{\partial \eta} (\psi_\eta \rho \alpha (\nabla \xi \cdot \nabla h)) \right] \\
& + \psi_\eta \nabla \cdot \left[\sum_i (\rho h_i (\alpha - D_i) \nabla Y_i) \right] \\
& + \psi_\eta \rho s_h.
\end{aligned} \tag{B.6}$$

Combining the second and fifth terms on the RHS of Eq. B.6 gives

$$\begin{aligned}
\frac{\partial \rho h \psi_\eta}{\partial t} + \nabla \cdot (\rho \mathbf{u} h \psi_\eta) = & - \frac{\partial^2}{\partial \eta^2} (\psi_\eta \rho h D_\xi (\nabla \xi)^2) + \frac{\partial}{\partial \eta} (\psi_\eta \rho (D_\xi + \alpha) (\nabla \xi \cdot \nabla h)) \\
& + \nabla \cdot (\rho D_\xi h \nabla \psi_\eta) + \nabla \cdot (\psi_\eta \rho \alpha \nabla h) \\
& - \psi_\eta \nabla \cdot \left[\sum_i (\rho h_i (\alpha - D_i) \nabla Y_i) \right] \\
& + \psi_\eta \rho s_h.
\end{aligned} \tag{B.7}$$

Expanding the third term on the RHS of Eq. B.7 results in

$$\begin{aligned}
\frac{\partial \rho h \psi_\eta}{\partial t} + \nabla \cdot (\rho \mathbf{u} h \psi_\eta) = & - \frac{\partial^2}{\partial \eta^2} (\psi_\eta \rho h D_\xi (\nabla \xi)^2) + \frac{\partial}{\partial \eta} (\psi_\eta \rho (D_\xi + \alpha) (\nabla \xi \cdot \nabla h)) \\
& + [\nabla \cdot (\rho D_\xi \nabla (h \psi_\eta)) - \nabla \cdot (\rho D_\xi \psi \nabla h)] + \nabla \cdot (\psi_\eta \rho \alpha \nabla h) \\
& - \psi_\eta \nabla \cdot \left[\sum_i (\rho h_i (\alpha - D_i) \nabla Y_i) \right] + \psi_\eta \rho s_h.
\end{aligned} \tag{B.8}$$

Combining the fourth and fifth terms on the RHS of B.8 results in

$$\begin{aligned}
\frac{\partial \rho h \psi_\eta}{\partial t} + \nabla \cdot (\rho \mathbf{u} h \psi_\eta) = & - \frac{\partial^2}{\partial \eta^2} (\psi_\eta \rho h D_\xi (\nabla \xi)^2) + \frac{\partial}{\partial \eta} (\psi_\eta \rho (D_\xi + \alpha) (\nabla \xi \cdot \nabla h)) \\
& + \nabla \cdot (\rho D_\xi \nabla (h \psi_\eta)) + \nabla \cdot (\psi_\eta \rho (\alpha - D_\xi) \nabla h) \\
& - \psi_\eta \nabla \cdot \left[\sum_i (\rho h_i (\alpha - D_i) \nabla Y_i) \right] + \psi_\eta \rho s_h.
\end{aligned} \tag{B.9}$$

Using Eq. B.4, and recognizing that the summation and divergence operations are associative, the second last term on the LHS of Eqn. B.9 rewritten, resulting in

$$\begin{aligned}
\frac{\partial \rho h \psi_\eta}{\partial t} + \nabla \cdot (\rho \mathbf{u} h \psi_\eta) &= -\frac{\partial^2}{\partial \eta^2} (\psi_\eta \rho h D_\xi (\nabla \xi)^2) + \frac{\partial}{\partial \eta} (\psi_\eta \rho (D_\xi + \alpha) (\nabla \xi \cdot \nabla h)) \\
&+ \nabla \cdot (\rho D_\xi \nabla (h \psi_\eta)) + \nabla \cdot (\psi_\eta \rho (\alpha - D_\xi) \nabla h) \\
&- \sum_i [\nabla \cdot (\psi_\eta \rho h_i (\alpha - D_i) \nabla Y_i)] \\
&- \sum_i \left[\frac{\partial}{\partial \eta} (\psi_\eta \rho h_i (\alpha - D_i) (\nabla \xi \cdot \nabla Y_i)) \right] \\
&+ \psi_\eta \rho s_h.
\end{aligned} \tag{B.10}$$

Averaging is applied to Eq. B.10, such that

$$\begin{aligned}
\frac{\partial \langle \rho h \psi_\eta \rangle}{\partial t} + \nabla \cdot \langle \rho \mathbf{u} h \psi_\eta \rangle &= -\frac{\partial^2}{\partial \eta^2} \langle \psi_\eta \rho h D_\xi (\nabla \xi)^2 \rangle + \frac{\partial}{\partial \eta} \langle \psi_\eta \rho (D_\xi + \alpha) (\nabla \xi \cdot \nabla h) \rangle \\
&+ \nabla \cdot \langle \rho D_\xi \nabla (h \psi_\eta) \rangle + \nabla \cdot \langle \psi_\eta \rho (\alpha - D_\xi) \nabla h \rangle \\
&- \sum_i \langle \nabla \cdot (\psi_\eta \rho h_i (\alpha - D_i) \nabla Y_i) \rangle \\
&- \sum_i \left\langle \frac{\partial}{\partial \eta} (\psi_\eta \rho h_i (\alpha - D_i) (\nabla \xi \cdot \nabla Y_i)) \right\rangle \\
&+ \langle \psi_\eta \rho s_h \rangle,
\end{aligned} \tag{B.11}$$

and the relationship $\langle \circ \psi \rangle = \langle \circ | \xi = \eta \rangle P(\eta)$, where \circ is a general quantity [7], is used in Eq. B.11 resulting in the unclosed form of the CMC ethalpy equation,

$$\begin{aligned}
\frac{\partial \langle \rho h | \xi = \eta \rangle P_\eta}{\partial t} + \nabla \cdot (\langle \rho \mathbf{u} h | \xi = \eta \rangle P_\eta) &= -\frac{\partial^2}{\partial \eta^2} (\langle \rho h D_\xi (\nabla \xi)^2 | \xi = \eta \rangle P_\eta) \\
&+ \frac{\partial}{\partial \eta} (\langle \rho (D_\xi + \alpha) (\nabla \xi \cdot \nabla h) | \xi = \eta \rangle P_\eta) \\
&- \sum_i \left(\frac{\partial}{\partial \eta} (\langle \rho h_i (\alpha - D_i) (\nabla \xi \cdot \nabla Y_i) | \xi = \eta \rangle P_\eta) \right) \\
&+ \nabla \cdot (\langle \rho D_\xi \nabla h | \xi = \eta \rangle P_\eta) + \nabla \cdot (\langle \rho (\alpha - D_\xi) \nabla h | \xi = \eta \rangle P_\eta) \\
&- \sum_i (\nabla \cdot (\langle \rho h_i (\alpha - D_i) \nabla Y_i | \xi = \eta \rangle P_\eta)) + \langle \rho s_h | \xi = \eta \rangle P_\eta,
\end{aligned} \tag{B.12}$$

which is the expression given in Eq. 4.24.

References

- [1] Natural Resources Canada. Energy efficiency trends in Canada 1990 to 2009. <http://oee.nrcan.gc.ca/publications/statistics/trends11/>, 2011. Government of Canada.
- [2] A. S. Ramadhas. *Alternative fuels for transportation*. CRC Press, 2011.
- [3] M. F. Hordeski. *Alternative fuels-the future of hydrogen*. CRC Press, 2nd edition, 2008.
- [4] E.-S. Cho and S. H. Chung. Improvement of flame stability and NO_x reduction in hydrogen-added ultra lean premixed combustion. *J. Mech. Sci. Technol.*, 23:650–658, 2009.
- [5] R. W. Bilger, S. B. Pope, K. N. C. Bray, and J. F. Driscoll. Paradigms in turbulent combustion research. *Proc. Combust. Inst.*, 30:21–42, 2005.
- [6] J. C. Hewson, A. J. Ricks, S. R. Tieszen, A. R. Kerstein, and R. O. Fox. Conditional-moment closure with differential diffusion for soot evolution in fire. In *Proc. of the Summer Program*, pages 311–323, Center for Turbulence Research, 2006.
- [7] A. Y. Klimenko and R. W. Bilger. Conditional moment closure for turbulent combustion. *Prog. Energy Combust. Sci.*, 25:595–687, 1999.
- [8] H. Schlichting. *Boundary-layer theory*. McGraw-Hill, 7th edition, 1979.
- [9] J. Warnatz, U. Maas, and R. W. Dibble. *Combustion: physical and chemical fundamentals, modeling and simulation, experiments, pollutant formation*. Springer-Verlag, 4th edition, 1999.
- [10] T. Poinsoot and D. Veynante. *Theoretical and numerical combustion*. R.T. Edwards, Inc., 2001.

- [11] N. Peters. *Turbulent combustion*. Cambridge University Press, Cambridge, 2000.
- [12] T. Poinso, S. Candel, and A. Trouvé. Applications of direct numerical simulation to premixed turbulent combustion. *Prog. Energy Combust. Sci.*, 21:531–576, 1995.
- [13] T. Poinso. Using direct numerical simulations to understand premixed turbulent combustion. *Symposium (Intl.) on combustion*, 26:219–232, 1996.
- [14] T. Baritaud, T. Poinso, and M. Baum. *Direct numerical simulation for turbulent reacting flows*. Editions TECHNIP, 1996.
- [15] L. Vervisch and T. Poinso. Direct numerical simulation of non-premixed turbulent flames. *Annual Rev. of Fluid Mech.*, 30:655–691, 1998.
- [16] J. Chen. Petascale direct numerical simulation of turbulent combustion-fundamental insights towards predictive models. *Proc. Combust. Inst.*, 33:99–123, 2011.
- [17] B. E. Launder and D. B. Spalding. The numerical computation of turbulent flows. *Computer Methods in Applied Mechanics and Engineering*, 3:269–289, 1974.
- [18] S. B. Pope. *Turbulent Flows*. Cambridge University Press, 2000.
- [19] H. K. Versteeg and W. Malalasekera. *An introduction to computational fluid dynamics: the finite volume method*. Pearson Education Limited, 2nd edition, 2007.
- [20] J. D. Buckmaster and G. S. S Ludford. *Theory of laminar flames*. Cambridge University Press, 1982.
- [21] S. H. Lam and J. Bellan. On de-coupling of Shvab-Zeldovich variables in the presence of diffusion. *Combust. Flame*, 132:691–696, 2003.
- [22] D. Veynante and L. Vervisch. Turbulent combustion modeling. *Prog. Energy Combust. Sci.*, 28:193–266, 2002.
- [23] S. P. Burke and T. E. W. Schumann. Diffusion flames. *Ind. Eng. Chem.*, 20:998–1004, 1928.
- [24] B. F. Magnussen and B. H. Hjertager. On mathematical modeling of turbulent combustion with special emphasis on soot formation and combustion. *Symposium (Intl.) on combustion*, 16:719–729, 1977.
- [25] D. B. Spalding. Mixing and chemical reactions in steady confined turbulent flames. *Symposium (Intl.) on combustion*, 13, 1971.

- [26] N. Peters. Laminar diffusion flamelet models in non-premixed turbulent combustion. *Prog. Energy Combust. Sci.*, 10:319–339, 1984.
- [27] R. W. Bilger. Conditional moment closure for turbulent reacting flow. *Phys. Fluids A*, 5:436–444, 1993.
- [28] A. Y. Klimenko. Multicomponent diffusion of various admixtures in turbulent flow. *Fluid Dyn.*, 25:327–333, 1990.
- [29] E. Mastorakos and R. W. Bilger. Second-order conditional moment closure for the autoignition of turbulent flows. *Phys. Fluids*, 10:1246–1248, 1998.
- [30] S. H. Kim, K. Y. Huh, and R. A. Fraser. Modeling autoignition of a turbulent methane jet by the conditional moment closure model. *Proc. Combust. Inst.*, 28:185–191, 2000.
- [31] S. H. Kim, K. Y. Huh, and R. W. Bilger. Second-order conditional moment closure modeling of local extinction and reignition in turbulent non-premixed hydrocarbon flames. *Proc. Combust. Inst.*, 29:2131–2137, 2002.
- [32] S. B. Pope. PDF methods for turbulent reactive flows. *Prog. Energy Combust. Sci.*, 11:119–192, 1985.
- [33] S. B. Pope. A Monte Carlo method for the PDF equations of turbulent reactive flow. *Combust. Sci. and Tech.*, 25:159–174, 1981.
- [34] M. D. Smooke and V. Giovangigli. Formulation of the premixed and nonpremixed test problem. In M. D. Smooke, editor, *Reduced kinetic mechanisms and asymptotic approximations for methane-air flames*. Springer Verlag, 1991.
- [35] H. Pitsch. Unsteady flamelet modeling of differential diffusion in turbulent jet diffusion flames. *Combust. Flame*, 123:358–374, 2000.
- [36] M. C. Drake, M. Lapp, C. M. Penney, S. Warshaw, and B. W. Gerhold. Measurements of temperature and concentration fluctuations in turbulent diffusion flames using pulsed Raman spectroscopy. *Symposium (Intl.) on combustion*, 18:1521–1531, 1981.
- [37] M. C. Drake, R. W. Pitz, and M. Lapp. Laser measurements on nonpremixed H₂-air flames for assessment of turbulent combustion models. *AIAA Journal*, 24:905–917, 1986.

- [38] R. S. Barlow and C. D. Carter. Raman/Rayleigh/LIF measurements of nitric oxide formation in turbulent hydrogen jet flames. *Combust. Flame*, 97:261–280, 1994.
- [39] R. S. Barlow and C. D. Carter. Relationships among nitric oxide, temperature, and mixture fraction in hydrogen jet flames. *Combust. Flame*, 104:288–299, 1996.
- [40] W. Meier, A. O. Vydrov, V. Bergmann, and W. Stricker. Simultaneous Raman/LIF measurements of major species and NO in turbulent H₂/air diffusion flames. *Appl. Phys. B*, 63:79–90, 1996.
- [41] W. Meier, S. Prucker, M.-H. Cao, and W. Stricker. Characterization of turbulent H₂/N₂/air jet diffusion flames by single-pulse spontaneous Raman scattering. *Combust. Sci. and Tech.*, 118:293–312, 1996.
- [42] A. R. Masri, R. W. Dibble, and R. S. Barlow. Chemical kinetic effects in nonpremixed flames of H₂/CO₂ fuel. *Combust. Flame*, 91:285–309, 1992.
- [43] L. L. Smith, R. W. Dibble, L. Talbot, R. S. Barlow, and C. D. Carter. Laser Raman scattering measurements of differential molecular diffusion in turbulent nonpremixed jet flames of H₂ / CO₂ fuel. *Combust. Flame*, 100:153–160, 1995.
- [44] V. Bergmann, W. Meier, D. Wolff, and W. Stricker. Application of spontaneous Raman and Rayleigh scattering and 2D LIF for the characterization of a turbulent CH₄/H₂/N₂ jet diffusion flame. *Appl. Phys. B*, 66:489–502, 1998.
- [45] V. R. Katta, L. P. Goss, and Roquemore. Effect of nonunity Lewis number and finite-rate chemistry on the dynamics of a hydrogen-air jet diffusion flame. *Combust. Flame*, 96:60–74, 1994.
- [46] F. A. Jaber, R. S. Miller, F. Mashayek, and P. Givi. Differential diffusion in binary scalar mixing and reaction. *Combust. Flame*, 109:561–577, 1997.
- [47] V. Nilsen and Kosály. Differential diffusion in turbulent reacting flows. *Combust. Flame*, 117:493–513, 1999.
- [48] R. Hilbert and D. Thévenin. Influence of differential diffusion on maximum flame temperature in turbulent nonpremixed hydrogen/air flames. *Combust. Flame*, 138:175–187, 2004.
- [49] R. W. Bilger. Molecular transport effects in turbulent diffusion flames at moderate Reynolds number. *AIAA Journal*, 20:962–970, 1982.

- [50] H. Pitsch and N. Peters. A consistent flamelet formulation for non-premixed combustion considering differential diffusion effects. *Combust. Flame*, 114:26–40, 1998.
- [51] J.-Y. Chen and W.-C. Chang. Modeling differential diffusion effects in turbulent nonreacting/reacting jets with stochastic mixing models. *Combust. Sci. and Tech.*, 133:343–375, 1998.
- [52] R. O. Fox. The Lagrangian spectral relaxation model for differential diffusion in homogeneous turbulence. *Phys. Fluids*, 11:1550–1571, 1999.
- [53] R. McDermott and S. B. Pope. A particle formulation for treating differential diffusion in filtered density function methods. *J. Comput. Phys.*, 226:947–993, 2007.
- [54] R. O. Fox, C. M. Cha, and P. Trouillet. Lagrangian PDF mixing models for reacting flows. In *Proc. of the Summer Program*, pages 369–380, Center for Turbulence Research, 2002.
- [55] S. Viswanathan, H. Wang, and S. B. Pope. Numerical implementation of mixing and molecular transport in LES/PDF studies of turbulent reacting flows. *J. Comput. Phys.*, 230:6916–6957, 2011.
- [56] G. Maragkos, P. Rauwoens, and B. Merci. A new methodology to incorporate differential diffusion in CFD simulations of reactive flows. *Combust. Flame*, 160:1903–1905, 2013.
- [57] V. V. Toro, A. V. Mokhov, H. B. Levinsky, and M. D. Smooke. Combined experimental and computational study of laminar, axisymmetric hydrogenair diffusion flames. *Proc. Comb. Inst.*, 30:485–492, 2005.
- [58] A. R. Kerstein. Linear-eddy modelling of turbulent transport, part 3, mixing and differential molecular diffusion in round jets. *J. Fluid Mech.*, 216:411–435, 1990.
- [59] L. Dialameh, M. J. Cleary, and A. Y. Klimenko. A multiple mapping conditioning model for differential diffusion. *Phys. Fluids*, 26:025107, 2014.
- [60] A. Kronenburg and R. W. Bilger. Modelling of differential diffusion effects in non-premixed nonreacting turbulent flow. *Phys. Fluids*, 9 (5):1435–1447, 1997.
- [61] A. Kronenburg and R. W. Bilger. Modelling differential diffusion in nonpremixed reacting turbulent flow: Application to turbulent jet flames. *Combust. Sci. and Tech.*, 166:175–194, 2001.

- [62] A. Kronenburg, R. W. Bilger, and J. H. Kent. Modeling soot formation in turbulent methane-air jet diffusion flames. *Combust. Flame*, 121:24–40, 2000.
- [63] Yunardi, R. M. Woolley, and M. Fairweather. Conditional moment closure prediction of soot formation in turbulent, nonpremixed ethylene flames. *Combust. Flame*, 152:360–376, 2008.
- [64] N. S. A. Smith, R. W. Bilger, C. D. Carter, R. S. Barlow, and J.-Y. Chen. A comparison of CMC and PDF modelling predictions with experimental nitric oxide LIF/Raman measurements in a turbulent H_2 jet flame. *Combust. Sci. and Tech.*, 105:357–375, 1995.
- [65] S. Navarro-Martinez and S. Rigopoulos. Differential diffusion modelling in LES with RCCE-reduced chemistry. *Flow Turb. Combust.*, 89:311–328, 2012.
- [66] A. Kronenburg and R. W. Bilger. Modelling differential diffusion in nonpremixed reacting turbulent flows: Model development. *Combust. Sci. and Tech.*, 166:195–227, 2001.
- [67] J. C. Hewson, A. J. Ricks, S. R. Tieszen, A. R. Kerstein, and R. O. Fox. On the transport of soot relative to a flame: Modeling differential diffusion for soot evolution in fire. In H. Bockhorn, A. D’Anna, A. F. Sarofim, and H. Wang, editors, *Combustion generated fine carbonaceous particles*, pages 271–587. Karlsruhe University Press, Karlsruhe, Germany, 2009.
- [68] J. C. Hewson, D. O. Lignell, and A. R. Kerstein. Modeling differential diffusion in non-premixed combustion: soot transport in the mixture fraction coordinate. In *Proc. of the Summer Program*, pages 225–236, Center for Turbulence Research, 2008.
- [69] D. O. Lignell, J. C. Hewson, and J. H. Chen. A-priori analysis of conditional moment closure modeling of a temporal ethylene jet flame with soot formation using direct numerical simulation. *Proc. Comb. Inst.*, 32:1491–1498, 2009.
- [70] L. Arnold. *Stochastic differential equations: theory and applications*. John Wiley & Sons Inc., 1974.
- [71] S. S. Girimaji. Assumed β -PDF model for turbulent mixing: validation and extension to multiple scalar mixing. *Combust. Sci. Tech.*, 78:177–196, 1991.
- [72] V. Eswaran and S. B. Pope. Direct numerical simulation of the turbulent mixing of a passive scalar. *Phys. Fluids*, 31:506–520, 1988.

- [73] N. Swaminathan and S. Mahalingam. Assessment of conditional moment closure for single and multistep chemistry. *Combust. Sci. Technol.*, 112:301–326, 1996.
- [74] P. Givi, C. K. Madnia, C. J. Steinberger, and S. H. Frankel. *Large eddy simulations and direct numerical simulations of high speed turbulent reacting flows*. NASA Langley Research Centre Technical Report, 1991.
- [75] V. R. Kuznetsov and V. A. Sabelnikov. *Turbulence and combustion, Moscow: Nauka, 1986. Turbulence and combustion*. Washington: Hemisphere, 1989.
- [76] C. B. Devaud, R. W. Bilger, and T. Liu. A new method of modeling the conditional scalar dissipation rate. *Phys. Fluids*, 6:2004–2011, 2004.
- [77] E. O’Brien and T. L. Jiang. The conditional dissipation rate of an initially binary scalar in homogeneous turbulence. *Phys. Fluids A*, 3:3121–3123, 1991.
- [78] S. S. Girimaji. On the modeling of scalar diffusion in isotropic turbulence. *Phys. Fluids A*, 4:2529–2537, 1992.
- [79] J. Janicka and N. Peters. Prediction of turbulent jet diffusion flame lift-off using a PDF transport equation. *Proc. Combust. Inst.*, 19:367–374, 1982.
- [80] M. Cleary. *CMC modelling of enclosure fires*. PhD thesis, University of Sydney, Sydney, Australia, 2004.
- [81] S. V. Patankar. *Numerical heat transfer and fluid flow*. Hemisphere, New York, 1980.
- [82] D. B. Spalding. A novel finite-difference formulation for differential expressions involving both first and second derivatives. *Int. J. Num. Methods Eng.*, 4, 1972.
- [83] W. H. Press, S. A. Teukolksy, W. T. Vetterling, and B. P. Flannery. *Numerical Recipes in Fortran*. Cambridge University Press, 2nd edition, 1992.
- [84] R. S. Barlow, N. S. A. Smith, J.-Y. Chen, and R. W. Bilger. Nitric oxide formation in dilute hydrogen jet flames: Isolation of the effects of radiation and turbulence-chemistry submodels. *Combust. Flame*, 117:4–31, 1999.
- [85] M. Fairweather and R. M. Woolley. First-order conditional moment closure modeling of turbulent, nonpremixed hydrogen flames. *Combust. Flame*, 133:393–405, 2003.
- [86] R. S. Barlow. Sandia H₂/He flame data - release 2.0. <http://www.ca.sandia.gov/TNF>, 2003. Sandia National Laboratories.

- [87] M. Schlatter, J. C. Ferreira, M. Flury, and J. Gass. Analysis of turbulence-chemistry interaction with respect to NO formation in turbulent, nonpremixed hydrogen-air flames. *Proc. Combust. Inst.*, 26:2215–2222, 1996.
- [88] R. W. Bilger. The structure of turbulent nonpremixed flames. *Proc. Combust. Inst.*, 22:475–488, 1988.
- [89] N. S. A. Smith, R. W. Bilger, and J.-Y. Chen. Modelling of nonpremixed hydrogen jet flames using a conditional moment closure method. *Symposium (Intl.) on combustion*, 24:263–269, 1992.
- [90] A. J. M. Buckrell and C. B. Devaud. Investigation of mixing models and conditional moment closure applied to autoignition of hydrogen jets. *Flow Turb. Combust.*, 90:621–644, 2013.
- [91] S. B. Pope. An explanation of the turbulent round-jet/plane-jet anomaly. *AIAA Journal*, 16:279–281, 1978.
- [92] A. P. Morse. *Axisymmetric turbulent shear flows with and without swirl*. PhD thesis, London University, London, England, 1977.
- [93] F. Tabet, B. Sarh, and I. Gökalp. Investigation of turbulent models capability in predicting mixing in the near field region of hydrogen-hydrocarbon turbulent nonpremixed flame. *Heat Mass Transfer*, 47:397–406, 2011.
- [94] B. J. McBride, S. Gordon, and M. A. Reno. *Coefficients for calculating thermodynamic and transport properties of individual species*. NASA Technical Memorandum 4513, 1993.
- [95] A. Burcat. Thermochemical data for combustion calculations. In W. C. Jr. Gardiner, editor, *Combustion chemistry*. Springer Verlag, New York, 1984.
- [96] J. Y. Chen, W. C. Chang, and M. Koszykowski. Numerical simulation and scaling of NO_x emissions from turbulent hydrogen jet flames with various amounts of helium dilution. *Combust. Sci. and Tech.*, 110-111:505–529, 1995.
- [97] G. L. Hubbard and C. L. Tien. Infrared mean absorption coefficients of luminous flames and smoke. *J. Heat Transfer*, 100:235–239, 1978.
- [98] W. L. Grosshandler. *RADICAL: A narrow-band model for radiation calculations in a combustion environment*. NIST Technical Note 1402, 1993.

- [99] A. Kronenburg, R. W. Bilger, and J. H. Kent. Second order conditional moment closure for turbulent jet diffusion flames. *Proc. Combust. Inst.*, 27:1097–1104, 1998.
- [100] N. T. Clemens and P. H. Paul. Effects of heat release on the near field flow structure of hydrogen jet diffusion flames. *Combust. Flame*, 102:271–284, 1995.